

Machine-learning Guided Search for Phonon-mediated Superconductivity in Boron and Carbon Compounds

Niraj K. Nepal^{1*} and Lin-Lin Wang^{1,2†}

[1] Ames National Laboratory, Ames, Iowa 50011, USA and

[2] Department of Physics and Astronomy, Iowa State University, Ames, Iowa 50011, USA

(Dated: January 13, 2026)

Abstract

We present a workflow that iteratively combines *ab-initio* calculations with a machine-learning (ML) guided search for superconducting compounds with both dynamical stability and instability from imaginary phonon modes, the latter of which have been largely overlooked in previous studies. Electron-phonon coupling (EPC) properties and critical temperature (T_c) of 417 boron, carbon, and borocarbide compounds have been calculated with density functional perturbation theory (DFPT) and isotropic Eliashberg approximation. Our study addresses T_c convergence of Brillouin zone sampling with an ansatz test, stabilizing imaginary phonon modes for significant EPC contributions and comparing performance of two ML models especially when including compounds of dynamical instability. We predict a few promising superconducting compounds with formation energy just above the ground state convex hull, such as $\text{Ca}_5\text{B}_3\text{N}_6$ (35 K), TaNbC_2 (28.4 K), $\text{Nb}_3\text{B}_3\text{C}$ (16.4 K), $\text{Y}_2\text{B}_3\text{C}_2$ (4.0 K), Pd_3CaB (7.0 K), MoRuB_2 (15.6 K), RuVB_2 (15.0 K), RuSc_3C_4 (6.6 K) among others.

*Corresponding author: Niraj K. Nepal, Email: nepalneeraz@gmail.com

†llw@ameslab.gov

I Introduction

The pursuit of high-temperature superconductivity (SC) is a challenging and active research area. The recent discovery of superconducting temperature (T_c) near 200 K in H_3S at the high pressure of 150 GPa[1] has re-energized the field to focus on phonon-mediated SC. For phonon-mediated SC, high phonon frequency from light atomic mass with strong electron-phonon coupling (EPC) is beneficial, as shown by the recent discovery of near room temperature T_c for metal hydrides under high pressure[2–10]. But making metallic bonds with hydrogen requires extremely high pressure. B and C compounds are known for their diverse structures and due to their light atomic mass, sizable T_c has been found in compounds [11–15] ranging from MgB_2 to metal intercalated graphite and fullerenes. Therefore, metallic B and C containing compounds with diverse structures are promising pools to search for new phonon-mediated superconductors. However, at ambient pressure, increasing T_c even just higher than the 40 K of MgB_2 [11, 16, 17, 19, 20] has been difficult [21–33]. While the recent report of a $T_c=32$ K for MoB_2 under the pressure of 110 GPa is a promising development [34], the large temperature and pressure gaps between MgB_2 and H_3S still remain, which motivates intensive search for new phonon-mediated SC compounds. Despite the challenges faced in experiments, theoretical studies continue to provide valuable insights into potential SC materials and their properties, such as SC in FeB_4 was first predicted[35] and then verified[36]. Density functional perturbation theory (DFPT) [37, 38] is one of the most robust *ab-initio* methods [10] to compute the EPC matrices over the full Brillouin zone (BZ). One can then employ either isotropic Eliashberg approximation or Green function-based anisotropic Migdal-Eliashberg equations to compute T_c [1, 40–42, 44–47]. Therefore, computational exploration of compounds containing atoms slightly heavier than H, such as B and C[11–15, 48], with strong EPC is a promising venue to search for high-temperature SC at ambient pressure and also fill the large materials gap between MgB_2 and H_3S .

Machine learning (ML) and Artificial intelligence (AI) are increasingly taking important roles for predicting materials properties including SC. ML models usually offer a computationally inexpensive alternative to DFPT calculations for evaluating superconducting properties, completing predictions in minutes compared to the months, typically required for high throughput DFPT calculations of hundreds of compounds. Previous studies performing ML predictions based on random forest [49], regression [50–53], classification [50], natural language processing (NLP) [54], and deep learning [55] models have trained on experimental data, mostly from SuperCon database [36]. Comparing to the more

* nepalneeraz@gmail.com

† llw@ameslab.gov

expensive and time consuming experiments to explore many new compounds to generate SC data for ML, the high throughput (HT) *ab-initio* first-principles approaches are valuable tools to obtain the data that can be trained to predict potential SC compounds. Several recent studies have utilized *ab-initio* computed data for training ML model and predicting SC. One approach involves performing BCS-inspired screening of materials to identify potential candidates based on certain key properties such as the Debye temperature and the density of states at the Fermi level ($N(E_F)$) [9]. A study similar to that described in Ref. [9] has been conducted on a vast range of materials, but restricting the size of the compounds to eight or fewer atoms, as reported in Ref. [58]. More recently, a new ML model suitable for the limited size of EPC dataset has been developed to predict Eliashberg spectral functions $\alpha^2 F(\omega)$ rather than the overall EPC strength, which represents an important step to account for the correlation between phonon density of state and EPC spectral function [59]. In a recent study [60], a ML approach was used to predict the maximum T_c and corresponding pressure of binary metal hydrides. The input layer consisted of atomic properties of the heavier metallic atom, while the output layer had two nodes representing T_c and pressure. The *ab-initio* data utilized in this study has been collected from literature. Recently, ML-driven search with experimental feedback was also performed to discover a novel superconductor in Zr-In-Ni systems [61].

Notably in these previous HT and ML studies, compounds of dynamical instability with imaginary phonon modes have been largely discarded. However, as shown by our recent EPC study [62] on Y_2C_3 with experimentally known $T_c=18K$ [32], imaginary phonon of C dimer wobbly motion once stabilized can carry significant EPC contributions, which explains well the observed sizable T_c . In recent model Hamiltonian studies, phonon softening and anharmonicity have also been found to enhance T_c [63, 64]. Here we present a workflow that iteratively combines *ab-initio* calculations with an ML-guided search across the dataset of compounds with both dynamical stability and instability from imaginary phonon modes by focusing on boron/carbon/borocarbide (B/C/B+C) compounds. *Ab-initio* calculations were performed to compute the EPC strength (λ), the logarithmic average phonon frequency (ω_{log}) and T_c of 417 compounds employing DFPT and isotropic Eliashberg approximation. Two major issues arise during DFPT calculations: choosing appropriate BZ sampling (\mathbf{k} and \mathbf{q} -mesh) for convergence and the problem of calculated dynamic instability. To address the convergence problem, we developed an ansatz test to check the convergence of EPC properties, particularly the T_c . For dynamically unstable compounds, we employed large electronic smearing, lattice distortion, and pressure to stabilize them. We then calculated their EPC properties, which were included in building the ML models. We evaluated ML models, specifically the crystal graph convolutional neural network (CGCNN) and the atomistic line graph neural network (ALIGNN), trained utilizing *ab initio* computed data to predict SC properties. The key new findings of this study are two-fold. First is the inclusion of the previously overlooked dynamical unstable compounds in the EPC training dataset, accounting for a sizable 20% of all compounds being studied, which would otherwise be omitted. Second, by including compounds with imaginary phonon modes, we reveal a clear performance gap between the two ML architectures, reinforcing the widely accepted principle that the completeness of a training dataset is as crucial as the ML model itself. Among the two models, especially when including the dynamically unstable compounds, ALIGNN consistently outperforms the CGCNN in predicting EPC properties. We predict a few promising SC compounds with formation energy just above the ground state convex hull. For dynamically stable systems, we predict $TaNbC_2$ (28.4 K), Nb_3B_3C (16.4 K), $Y_2B_3C_2$ (4.0 K) among others. For systems with dynamical instability and imaginary phonon modes, we predict $Ca_5B_3N_6$ with a T_c as high as 35-42.4 K, besides Pd_3CaB (7.0 K), and a few Ru compounds of $MoRuB_2$ (15.6 K), $RuVB_2$ (15.0 K), and $RuSc_3C_4$ (6.6 K).

II Results

A Machine learning guided workflow

A ML-guided search workflow is employed in this study. It can be divided into three parts: data extraction, DFPT calculations, and training ML models. We will discuss each part in the following three sections (A, B and C) before presenting the main results in the last three sections (D, E and F). As illustrated in Fig. 1 for obtaining the crystal structures of all the known B/C/B+C compounds, we utilized the Materials Project (MP) database [65-67], which offers a diverse range of compounds, including experimentally synthesized and theoretically predicted ones. We selected those B and C compounds in the MP database that meet certain criteria: being metallic with negative formation energy, excluding oxides, C_{60} and Lanthanides except for La. Approximately 1500 compounds fall within this category, out of which 400 exhibit magnetic moments, and these magnetic cases are not considered in the present study. Consequently, our focus narrows down to around 1100 nonmagnetic compounds, forming the pool for investigating phonon-mediated superconductivity. To manage computational cost, we set a further criterion that considers only systems with primitive cells containing 40 atoms or less and composed of up to four different elements ($N_{type} \leq 4$). This refinement narrows our selection to approximately 700 compounds. These 700 include 121

compounds with known T_c from experimental measurement as in SuperCon database (113 being dynamically stable and 8 dynamically unstable) and the other 579 compounds of unknown T_c . We will first discuss the 113 compounds with known T_c and also dynamical stability (no imaginary phonon modes), while the remaining 8 compounds with dynamical instability will be discussed later.

Figure 2 provides a statistical description of the 113 B/C/B+C compounds with known T_c and dynamic stability, which are 53 superconductors (SC) and 60 non-superconductors (NSC). We reviewed and corrected any inaccuracies or discrepancies found in the SuperCon database through an extensive literature review [16, 29, 33, 34, 36, 37, 41, 42, 44, 46, 68–99, 101–110, 112–117, 119–140, 142–152].

Figure 2 (a)-(c) illustrate the distribution of different elements in these systems, allocation of B/C/B+C compounds and thermodynamic stability, respectively. The thermodynamic stability of these compounds, indicated by the energy above the ground state convex hull (ΔE_h), are obtained from the MP database[65]. Approximately 71% of the compounds are on the ground state convex hull with $\Delta E_h \sim 0$. Around 18% of the cases have an ΔE_h within 0.05 eV/atom, while the remaining 11% have ΔE_h larger than 0.05 eV/atom. Figure 2(d) shows the distributions of these compounds based on their space groups (SGs). In Fig. 2(a) and (d), each bar is partitioned into two segments with the red segment representing the number of SC, while blue segment for NSC. From Fig. 2(a), many known SC compounds are associated with transition metals (TM) such as Y, La, Ni, Rh, Mo, Nb and others. Figure 2(e)-(m) depict the crystal structures of the representative SC compounds in the top 6 SGs among the experimentally known SC. In these structures, B and C atoms form various structural motifs: honeycomb lattice of B in MgB_2 (Fig. 2(e)); monomers in NbC (Fig. 2(f)), MgCNi_3 (Fig. 2(h)) and Mo_2GaC (Fig. 2(i)); dimers in YC_2 (Fig. 2(k)); graphene sheets in SrC_6 (Fig. 2(j)); chains of lighter elements in Mo_2BC (Fig. 2(g)) and $\text{LaPt}_2\text{B}_2\text{C}$ (Fig. 2(m)); octahedral cage structures in YB_6 (Fig. 2(l)). In terms of the lattice types of these known SC compounds, highly symmetric structures with hexagonal, tetragonal and cubic SGs have the most compounds, as shown in Fig. 2(d). Similarly, statistical description for the SC compounds with predicted T_c that have not been measured, akin to Fig. 2, is illustrated in Supplementary Materials (SM) Fig.S1.

B Overview of DFPT calculations

After the crystal structures of B and C compounds have been collected, the next step as shown in Fig.1 is to do HT calculations with DFPT on EPC properties for compounds with both known and unknown T_c using our recently developed high-throughput electronic structure package (HTESP) [157]. We performed DFPT calculations and computed EPC properties using the isotropic Eliashberg approximation. The accuracy of the EPC data is crucial for building reliable ML models. We have encountered two major challenges in the HT calculations with DFPT. One is the convergence with respect to BZ sampling and the other is dynamic instability. The first obstacle involved determining appropriate BZ samplings (\mathbf{k} - and \mathbf{q} - meshes) to compute the EPC properties, as these calculations become computationally expensive with dense meshes. To reduce the computational cost, we initiated an efficient screening by using a \mathbf{k} -point mesh that accurately describes the ground-state structures and energetics. EPC quantities are then interpolated to fine \mathbf{k} -mesh only twice the size of the coarse \mathbf{k} -mesh. But we noticed that calculations with such grid combination can lead to inaccurate predictions, with discrepancies as high as approximately 10% of the total compounds with known T_c , giving NSC for known SC and vice versa. To address this problem, we developed an ansatz test to assess the convergence of T_c with respect to the \mathbf{k} -point mesh. This approach leverages the decaying behavior of T_c with respect to Gaussian broadening width (σ), which is used in the double-delta integration. Initially, we acquired results using the DFPT method with the \mathbf{k} -point mesh size from the MP database. Subsequently, we assessed the convergence of these results based on the convergence ansatz test. To ensure convergence, we repeated calculations with denser \mathbf{k} -mesh for the cases where results did not pass this test. We applied this technique to the 113 dynamically stable compounds, and obtained reasonable accuracy for the calculated T_c with a mean absolute error (MAE) of 2.21 K compared to experimental data, as presented in Supplementary Figure S2 (b). Moreover, incorporating dynamically unstable compounds further improves the dataset quality, as evidenced in supplementary Fig. S2(c)–(d) by the enhanced R_{log}^2 score in the $\log(T_c)$ comparison with experiment. Further details regarding the convergence with respect to the \mathbf{k} - and \mathbf{q} -point meshes are discussed in the Method section and SM. In addition to the 113 dynamically stable compounds with known T_c , we also computed the EPC properties of 268 compounds of unknown T_c with dynamical stability, resulting from the ML-guided search as summarized in Fig.1.

The second obstacle encountered in EPC calculations was the presence of imaginary phonon modes and dynamical instability in almost 146 compounds. Among them, the imaginary phonon modes in 36 compounds show large EPC contribution. Stabilizing these imaginary modes is crucial for calculating EPC properties in such systems. These imaginary modes can be stabilized through lattice distortion, pressure, and electronic smearing, with the latter method being particularly effective in HT screening[62]. A comprehensive analysis of dynamical instability and its implications for superconductivity will be presented in the “Imaginary phonon modes and superconductivity” section.

In addition to these instances, there are cases up to 173 compounds, where EPC calculations are not complete due to either numerical problems or too large size of unit cells. For now, we will set these cases aside and will revisit them in the future.

C Training and testing ML models

Besides the data extraction and DFPT calculations, training and testing ML models also play crucial roles in the ML-guided search workflow in Fig.1. We utilized two different ML models: CGCNN[158] and ALIGNN[159]. CGCNN maps 3D crystal structures to 2D graphs by using chemical element information and neighbor bonding distance to encode them into local chemical environments through convolution operations and updating the node features based on these descriptors. The updated node features are then aggregated to represent the entire crystal, which is connected to the output via a neural network. ALIGNN includes extra local chemical information, such as bonding angles, in addition to the crystal graphs in CGCNN with another auxiliary graph of bonding distances and angles. The parameters, including weights and biases, of the neural network connections are learned through training with available DFPT data.

As shown in Fig. 1, we trained the initial ML models in Run 1 using a dataset of 250 dynamically stable compounds with 109 SC (calculated $T_c > 1$ K) and 141 NSC (calculated $T_c < 1$ K) including those 113 from SuperCon database that were already measured in experiments. This dataset encompasses 45 distinct SGs. For the purpose of evaluation, a separate collection of 58 stable compounds (18 SC and 40 NSC), belonging to 27 unique SGs (6 of which are not part of the training 45), was reserved exclusively for independent testing and was not involved in the ML training process. Moving from Run 1 to Run 2, we use the Run 1 ML model (trained on 250 dynamically stable compounds) to predict T_c for the remaining B-C compounds, which is fewer than 450, because some compounds were already found to be dynamically unstable but without EPC data during Run 1 ML training. We then sort the predictions and select the top candidates of both SC and NSC for more DFPT calculations to close the ML-guided loop. In Run2, the original 250 stable systems were augmented with an additional 73 dynamically stable systems to refine the ML models. In the concluding stage of Run 3, we incorporated the results derived from the compounds with dynamic instability. Notably, this stage included results from 2 new SGs. Among the 36 results in this category, we incorporated 28 into the training set and added 8 compounds into the independent test set. In the overall count of 417 compounds with converged EPC properties, 181 were classified as SCs, whereas 236 were categorized as NSCs. The progress from Run 1 to Run 3 constitutes a loop, as illustrated in Fig. 1. In summary, our methodology has a series of iterations involving training and testing ML models with increasingly comprehensive datasets from dynamically stable to unstable compounds.

D Comparison of ML models

Next, we will present the main results of the ML models and guided search, highlight the notable compounds, including cases of dynamical stability and instability. Figures 3(a-d) depict the ML-predicted vs. DFPT-calculated λ , ω_{log} , T_c , and T'_c using the dynamically stable systems in Run 1, respectively. Here, T_c represents the critical temperature computed using DFPT-computed λ and ω_{log} or predicted directly from ML models, while T'_c is calculated from the ML-predicted λ^{ML} and ω_{log}^{ML} using Eq. 1 in a postprocessing manner.

$$T'_c = \frac{\omega_{log}^{ML}}{1.2} \exp \left[-\frac{1.04(1 + \lambda^{ML})}{\lambda^{ML} - \mu_c^*(1 + 0.62\lambda^{ML})} \right], \quad (1)$$

Here, It is important to note that the data first used do not include dynamically unstable cases. For Run 1, we trained ML models using 250 compounds, divided into training, validation, and testing sets in a ratio of 0.8:0.1:0.1. The mean absolute errors (MAEs) for the 10% test set in each training iteration are documented in Supplementary Table S1. An additional independent test set of 58 compounds was used to assess the predictability of the ML models and their MAE and predictions are plotted in Fig. 3. Apart from MAE, we also computed the R^2 -score for the ML parity plot, which is presented in Supplementary Table S2. As expected, accurately predicting the exact EPC properties is challenging. However, the performance of the ML models improves when superconductors with stabilized phonons are included. The training process consisted of 3000 epochs using default settings provided by the ML packages, which have been thoroughly investigated in the original work [158, 159]. In both CGCNN and ALIGNN, training and validation procedures are employed. Checkpoints are established at regular intervals to store crucial parameters such as model weights and architecture. The ML packages operate automatically to retain and update the model exhibiting the best performance, determined by the lowest validation error. This iterative process also acts to mitigate

overfitting concerns. Our Supporting Figure S3 and Supporting Table S2 demonstrate that training up to 1500 epochs is sufficient to achieve the lowest validation error for both ALIGNN and CGCNN model. The performance of the models was evaluated by computing the MAE between the predicted and target quantities for the independent test set. The MAEs for CGCNN-predicted λ and ω_{log} stand at 0.23 and 105 K, respectively, while the corresponding numbers for ALIGNN are slightly higher at 0.28 and 113 K (Figs. 3(a) and (b)). In terms of predicting T_c , the CGCNN and ALIGNN models yield MAEs of 2.4 K and 3.8 K, respectively. Despite the relatively small magnitude of MAEs, the ML outcomes exhibit distinct clustering patterns, as shown in Fig. 3(c). Specifically, for the CGCNN model, the results tend to cluster closely along the “DFPT” axis (red arrow in Fig. 3(c)), whereas for ALIGNN, the clustering is pronounced along the “ML prediction” axis (blue arrow in Fig. 3(c)). An alternative approach, rather than directly training and predicting T_c , is to utilize ML-predicted values, specifically λ^{ML} and ω_{log}^{ML} , to estimate T'_c using Eq. 1. This modification not only enhances predictive performance for both models but also slightly ameliorates the issue of clustering [Fig. 3(d)]. A comparable approach has been employed in a recent study [160], wherein λ and ω_{log} can be directly acquired from first principles calculations.

Then we use the predicted T'_c to rank the remaining compounds to pick the ones with high and low T'_c for additional DFPT calculations. In this next stage, we utilized ML-guided search to expand the dataset to 323 systems characterized by 54 distinct SGs, the ML models underwent further training. Subsequently, the improved ML models were subjected to the same independent testing, employing the same set of 58 system test cases. The outcomes of the Run 2 are presented in Figs. 3(e)-(h). The results demonstrate a notable improvement in addressing the issue of prediction clustering with the expansion of the training dataset, all while maintaining reasonable accuracy. ALIGNN improves the prediction of λ and ω_{log} with MAEs of 0.24 and 93K, respectively, compared to CGCNN’s MAEs of 0.26 and 97K. However, T'_c calculated from ML-predicted λ^{ML} and ω_{log}^{ML} shows a significant improvement for ALIGNN, with an MAE of 2.7K. Notably, ω_{log} is more accurately predicted than λ and then T_c , because the former is directly related to the overall bonding strength and cohesive energy, while the later depends on the details of the Fermi surface and the EPC matrix elements.

As mentioned above, from the ML-guided search, we find quite some number of compounds with imaginary phonon and dynamical instability. In all the previous high throughput phonon-mediated SC studies, these dynamically unstable compounds are simply discarded, but as shown by our recent study [62] on Y_2C_3 , some imaginary phonon modes once stabilized can carry a large EPC and give rise to a large T_c . Thus, specifically here we also include dynamically unstable compounds in ML. As far as we know, this is the first ML trained with both dynamically stable and unstable compounds for phonon-mediated SC. We carried out a distinct training and testing phase for ML models, incorporating dynamically unstable cases after stabilization, denoted as Run 3. These results predominantly included nonzero T_c . Among these, 28 results were added to the training dataset, while the remaining 8 were added for independent testing. In total, the independent test set now consists of the original 58 dynamically stable and additional 8 stabilized compounds with imaginary phonon modes. Both the training and test datasets were balanced across various SGs. The outcomes of Run 3 are illustrated in Fig. 4(a)-(d). In Run 3, the ALIGNN model consistently outperforms the CGCNN model across different superconducting properties. The ALIGNN model achieves MAEs of 0.27 for λ , 86 K for ω_{log} , 4.3 K for T_c , and 3.5 K for T'_c . In contrast, the CGCNN model records MAEs of 0.34, 104 K, 4.5 K, and 5.3 K for the respective properties. The reason is that ALIGNN includes the bonding angles as part of training parameters, which better describe the dynamically unstable compounds, because imaginary phonon modes often involves lower-energy bond rotation with changing angle than higher-energy bond stretching vibration. Based on the information presented in Figs. 3 and 4, it is apparent that the ML model performs better in learning the parameters ω_{log} than λ and then T_c . As a result, it is justifiable to utilize Eq. 1 to estimate the ML-predicted critical temperature T'_c rather than relying solely on the directly predicted T_c values. Furthermore, we separately computed the MAE for SC and NSC, as shown in Supplementary Table S3. ALIGNN demonstrates better accuracy in predicting ω_{log} compared to CGCNN for both categories. However, it predicts λ more accurately than CGCNN for NSC, while performing slightly worse for SC. Additionally, a classification model was employed, with the results presented in the Supplementary Table S4.

E Dynamically stable systems

In Table I, we present the results of our ML-guided search for dynamically stable compounds with DFPT-calculated T_c exceeding 10 K, while the complete list of EPC properties of the 381 dynamically stable compounds are presented in SM from Table S10 to S17. It is worth noting that the compounds with high T_c tend to be thermodynamically metastable, as indicated by their formation energy significantly above the convex hull. B_2CN in different phases, with ΔE_h up to 0.35 eV/atom, has been predicted to exhibit SC, consistent with earlier theoretical findings [161]. TaC and NbC , both have sizable T_c in the metastable hexagonal structure, while their more stable cubic structures in $Fm - 3m$ have already been observed with SC [162, 163]. In Table I, the first compound close to the ground state

TABLE I: DFPT calculated EPC results for experimentally unknown systems with $T_c > 10$ K, whose superconductivity has not yet been measured; SG is spacegroup, and ΔE_h is taken from materials project. [65]

Compound	SG	ΔE_h (eV/atom)	λ	ω_{log} (K)	T_c (K)
B_2CN	R3m	0.34	1.66	578	60.7
B_2CN	P3m1	0.35	1.11	567	34.9
Mo_7B_{24}	P-6m2	0.15	1.28	386	29.6
$TaNbC_2$	R-3m	0.02	1.41	326	28.4
TcB	P6 ₃ /mmc	0.26	1.32	333	26.5
TaC	P-6m2	0.41	1.54	235	22.8
ZrBC	P6 ₃ /mmc	0.45	1.12	321	20.0
Ta_2CN	I4 ₁ /amd	0.13	1.94	162	19.8
Ta_2CN	P4/mmm	0.15	2.70	127	19.5
B_2CN	P-4m2	0.32	0.80	644	18.8
TaB ₂	P6/mmm	0.0	1.22	254	18.1
NbFeB	P-6m2	0.42	1.64	173	18.0
Nb_3B_3C	Cmcm	0.02	1.25	229	16.4
V_2CN	R-3m	0.12	1.00	323	16.2
NbC	P6 ₃ /mmc	0.15	0.84	455	15.3
$ZrMoB_4$	P6/mmm	0.09	1.30	193	15.1
NbVCN	R3m	0.16	0.99	274	13.4
Ta_4C_3	Pm-3m	0.13	1.46	138	12.6
NbVC ₂	R-3m	0.11	0.83	365	11.9
Nb_2CN	R-3m	0.08	0.88	310	11.7
$Nb_4B_3C_2$	Cmcm	0.05	1.01	219	11.3
TaVC ₂	R-3m	0.08	0.80	343	10.3

convex hull ($\Delta E_h \sim 0.02$ eV/atom) is $TaNbC_2$, whose crystal structure and EPC properties are plotted in Fig. 5(a)-(c). It crystallizes in the trigonal structure of $R-3m$. The calculated EPC properties are $\lambda = 1.4$, $\omega_{log} = 326$ K, and $T_c = 28.4$ K, with the majority of the contribution coming from phonons within the 3-6 THz range (Fig. 5(b) and (c)), as well as a significant contribution from the 16-20 THz range of C-dominated modes. Other compounds close to the ground state convex hull with $\Delta E_h \leq 0.02$ is TaB_2 . The presence of SC in TaB_2 remains a subject of debate as discussed in the previous studies [95].

Moreover, we predict other ternary superconductors, such as Nb_3B_3C (ΔE_h of 0.018 eV/atom [65]), with T_c of 16.4 K (Figs. 5 (d), (f), (h) and (j)). Comparison between the calculated and experimental T_c are also plotted (blue circles) for the Nb-B-C superconductors with known T_c . These ternary metallic borocarbides were all experimentally synthesized [164], however, some of their SC (red circles) have not been reported yet, with Nb_3B_3C has a predicted T_c as high as 16.4 K. To differentiate them from experimentally measured systems, we color-coded them in red and presented them along the $y = x$ line. The crystal structure of Nb_3B_3C exhibits an interesting layer-like arrangement as in Fig. 5(f), where B atoms form strips of honeycomb lattice, while C being monomers. The λ -projected phonon dispersion (Fig. 5(h)) analysis indicates that the SC is attributed to the presence of low-frequency soft phonon modes in the vicinity of the Z and T points of the BZ. For ternary Nb-B-C systems, EPC calculations with isotropic approximation tend to overestimate T_c , while for Y-B-C systems, EPC calculations have also notable underestimations as plotted in Fig. 5(e). Therefore, we also show the EPC properties of $Y_2B_3C_2$ with a predicted T_c of 4 K, but having $\Delta E_h \sim 0$ [65], along with other experimentally measured Y-B-C systems in Fig. 5(e). Unlike Nb_3B_3C , the crystal structure of $Y_2B_3C_2$ shows a layer of mixed B and C network sandwiching the Y layer (Fig. 5(g)). The λ -projected phonon dispersion shows that the EPC properties are mostly contributed by phonon within the 4-10 THz energy range around the Γ and Z points (Figs. 5 (i) and (k)). Other compounds with calculated $T_c < 10$ K and their EPC properties are listed in SM.

F Imaginary phonon modes and superconductivity

In this section, we address the issue of dynamical instability observed in the DFPT-computed phonon dispersion (146 out of 700 compounds). Out of these 146 dynamical unstable compounds, 34 exhibit large EPC in their imaginary phonon modes. Figure 6 (a) and (b) provide the breakdown of these 34 compounds based on their constituent elements, while (c) and (d) show the distribution of systems in terms of formation energy and SG, respectively. As expected, a considerable portion of these compounds with imaginary phonon have formation energies above the convex hull. Superconductivity in Sc_2C_3 , shown in Fig. 6 (d), are very likely because SC has been observed in the same structure with larger cations of the same group as in Y_2C_3 [165] and La_2C_3 [166], which are closer to the convex hull. We have categorized these compounds into two groups based on whether the imaginary phonon modes occur at the Γ -point or elsewhere. The instabilities at Γ -point are represented by Sc_2C_3 , Ta_2B , and La_3InB (Fig. 6(i-l)) which constitutes 11 cases, whereas the other 23 compounds including MoB_2 represents the case of dynamic instability outside of Γ -point, as illustrated in Figs. 6(l) for MoB_2 . The unstable phonon modes possess a large mode-resolved λ in the vicinity of instability, $\lambda_{\mathbf{q}\nu} = \frac{\gamma_{\mathbf{q}\nu}}{\pi N(E_F)\omega_{\mathbf{q}\nu}^2}$, where $\gamma_{\mathbf{q}\nu}$ is the change in phonon linewidth due to EPC (See Fig. 6). The systems with dynamical instability at Γ -point can be stabilized by obtaining a low-symmetry ground state structure through lattice distortion along the direction of the imaginary eigenmodes at Γ and performing a full ionic relaxation. The analysis presented here is expanded from our earlier work on Y_2C_3 [62]. The application of smearing to stabilize imaginary phonon modes has been explored in other systems, including β -phase $\text{Ni}_x\text{Al}_{(1-x)}$ [167], NiTi [168] and EuAl_4 [169]. In these cases, instead of optical modes, the instability arises from acoustic modes. It was proposed that the dynamic instability observed in these materials is the result of strong EPC between nested electronic states near the Fermi level [167–169]. Previously as exemplified with Y_2C_3 [62] these imaginary phonon modes can significantly contribute to λ after stabilization. Although these cases represent only a small fraction of the compounds, disregarding them would exclude potential SC compounds with a sizable T_c .

Performing EPC calculations on low-symmetry structures can be computationally expensive, especially when the system contains a large number of atoms like Sc_2C_3 . Hence, it is recommended to first try stabilization using pressure and smearing. The former option of stabilizing through pressure can give interesting pressure-dependent properties, whereas the latter with increasing electronic smearing can be beneficial for HT computations. To stabilize the dynamically unstable systems, we applied pressure (ranging from 5 to 60 GPa) or used a larger electronic smearing (0.05, 0.06, 0.08, 0.1 Ry). In each case, we fully relaxed the structures. We computed the EPC properties for the stabilized systems around Γ -point and presented the results in Table II together with their SG and ΔE_h . Most of these compounds crystallize in high-symmetry structures such as cubic, hexagonal and tetragonal lattices. The relative ground state energy of relaxed low-symmetry structures compared to the original high-symmetry ones are listed as Distorted GS. We utilize pressure and the electronic smearing to stabilize the imaginary phonons in Y_2C_3 , La_2C_3 and Sc_2C_3 . However, for Ta_2B and La_3InB systems, pressure and smearing were insufficient for stabilization, so lattice distortion was employed. The calculated T_c using DFPT for the stabilized systems agrees well with experimental data. For example, $\text{Al}_2\text{Mo}_3\text{C}$ exhibits an instability at Γ akin to that observed in Sc_2C_3 . After stabilization with electronic smearing, the calculated T_c is 12.05 K, which is comparable to the experimental T_c of 9.2 K [170]. We predict the EPC properties for Sc_2C_3 , YBC, and MoB_4 with a sizable T_c of 27.9 K, 10.15 K and 7.58 K under ambient or moderate pressure. These compounds have formation energy higher (0.11, 0.42, and 0.26 eV/atom respectively) than the ground state convex hull, indicating they are metastable.

Figure 6(m)-(p) displays the λ -projected phonon dispersion for four different stabilized compounds: Sc_2C_3 (P-30), Ta_2B (D), La_3InB (D), and MoB_2 (S-0.1), utilizing pressure of 30 GPa, distortion (D), distortion (D), and smearing of 0.1 Ry, respectively. By comparing these plots with Figs. 6(i)-(l), we can see that the soft optical phonon modes are stabilized and contribute significantly to λ near the Γ -point, represented by green open circles. Despite the slight lifting of phonon band degeneracy caused by distortion, the large contribution to EPC remains, which give rise to SC. The discovery of such systems is interesting as it presents opportunities for stabilization through pressure and alloying, leading to potentially high T_c metastable compounds that may be synthesizable in experiment.

For the compounds with imaginary phonon modes away from the Γ point, i.e. MoB_2 -type, we also stabilized these dynamically unstable compounds with larger electronic smearing of 0.1 Ry and tabulated the results in Table. III. For example, compounds like MoB_2 in the MgB_2 structure have shown experimentally measured T_c of 32 K under high pressure [34]. Moreover, we demonstrate that large electronic smearing can play a role similar to pressure in stabilizing imaginary phonon modes. The pressure-induced stabilization of MoB_2 is presented in Supplementary Fig. S4. Our calculated structural phase transition from R-3m to P6/mmm phase at 75 GPa agrees well with the experimentally reported critical pressure of 70 GPa [34]. The calculated electron–phonon coupling (EPC) at 75 and 90 GPa yields T_c values of 28.4 K and 28.6 K, respectively, which are consistent with the experimental value of 32 K, as well as with results obtained from the electronic smearing approach used for high-throughput calculations. Notably, both approaches give comparable EPC parameters for the same stabilized low-lying phonon modes: at 75 GPa we obtain $\lambda = 1.85$, $\omega_{log} = 244$ K, and $T_c = 28.4$ K, while the smearing-based approach (Table III) gives $\lambda = 2.12$, $\omega_{log} =$

TABLE II: Stabilization of imaginary phonon modes (around Γ) utilizing Distortion (D), Pressure (P), and Smearing (S). The values of pressure and smearing are presented as P-value (GPa) and S-value (Ry) respectively. Crystal is distorted along the direction represented by eigenmode at Γ and relaxed to obtain low-symmetry ground-state structures. Distorted GS is the difference between ground-state total energy of an undistorted and distorted structures at equilibrium. SG is spacegroup and ΔE_h represents the energy above the ground state hull.

Compound	SG	ΔE_h (eV/atom)[65]	Distorted GS (meV/atom)	EPC (λ)	ω_{log} (K)	T_c (K)	T_c^{Expt} (K)
Y ₂ C ₃	I-43d	0.04	0.9	1.94 (P-10)	175.23 (P-10)	21.27 (P-10)	18 [165]
				1.14 (S-0.1)	227.97 (S-0.1)	14.50 (S-0.1) [62]	
La ₂ C ₃	I-43d	0.0	2.2	1.15 (S-1)	219.4 (S-1)	14.3 (S-0.1)	13.4 [166]
Sc ₂ C ₃	I-43d	0.11	3.6	1.435 (P-30)	303.18 (P-30)	27.90 (P-30)	-
				1.99 (S-0.1)	205.6 (S-0.1)	25.5 (S-0.1)	-
Al ₂ Mo ₃ C	P4_132	0.05	0.6	1.19 (S-0.1)	174.95 (S-0.1)	12.05 (S-0.1)	9.2 [170]
YBC	Cmmm	0.42	150	0.73 (P-20)	454.42 (P-20)	10.15 (P-20)	-
W ₂ B	I4/mcm	0.0	0.6	0.81 (D)	215.68 (D)	6.61 (D)	3.10 [29]
Mo ₂ B	I4/mcm	0.03	3.6	0.79 (D)	284.65 (D)	8.12 (D)	4.74 [29]
Ta ₂ B	I4/mcm	0.03	8.9	0.44 (D)	236.84 (D)	0.34 (D)	3.12 [29]
MoB ₄	P6/mmm	0.26	0.7	0.69 (D)	418.42 (D)	7.58 (D)	-
La ₃ InC	Pm-3m	0.0	0.6	1.04 (D)	108.63 (D)	5.844 (D)	2.6 [171]
La ₃ InB	Pm-3m	0.20	2.3	1.18 (D)	83.03 (D)	5.60 (D)	10 [171]

209 K, and $T_c = 27.3$ K. Another notable example in Table III is Ca₅B₃N₆ with ΔE_h of 0.03 eV/atom, which exhibits dynamical instability at the H point and displayed a significant mode-resolved λ near its unstable phonon modes, as depicted in Fig. 7 (d)-(e). After stabilizing the system with electronic smearing of 0.06 Ry, Ca₅B₃N₆ exhibits a λ of 1.5. The ω_{log} is found to be 372 K. Moreover, when computing λ (with broadening parameter $\sigma = 0.01$ Ry), the T_c is determined to be 35 K with Coulomb potential $\mu_c^* = 0.16$ and 42.4 K with $\mu_c^* = 0.10$, much larger than that of MgB₂ (16-20 K) computed from isotropic approximation. It should be noted that Ca₅B₃N₆ has been synthesized in cubic structure and Im3'm (229) SG with partial occupancy in the 8c site of Ca [172]. The crystal structure of this boronitride (Fig. 7(a)-(c)) has a cage-like structure, similar to XB₃C₃ borocarbides (X = Ca,Ba,Sr,Y,La). For the stoichiometric Ca₅B₃N₆, Fig. 7(f) and (g) present the isotropic Eliashberg spectral function and electronic band structure, respectively. It shows an electron-doped band structure that connects to strong EPC as also found in other predicted SC compounds and studies. As listed in Table III, interestingly some of the trigonal compounds of NbMoC₂ are in the same structure as the stable TaNbC₂ in Table I. This shows that in this particular structure, with the substitution of neighboring group of early TMs, although bringing dynamical instability, the phonons once stabilized can still provide a large EPC contribution for a sizable T_c . As also listed in Table III, other compounds with sizable predicted T_c after stabilization that also near GS hull are some notable ternary Ru compounds, MoRuB₂ at 15.6 K, RuVB₂ at 15.0 K, Pd₃CaB at 7.0 K and RuSc₃C₄ at 6.6 K.

III Discussion

In this work, we have employed the machine learning (ML) models that utilize the data generated from *ab-initio* calculations using the DFPT and the isotropic Eliashberg approximation to iteratively guide the search for new phonon-mediated superconductors among B and C compounds. Our study also focuses on addressing the challenges encountered during DFPT calculations, such as convergence of Brillouin zone (BZ) sampling and the problem of calculated dynamic instability. To address the convergence issue, we developed an ansatz test to verify the convergence of superconductivity (SC) critical temperature T_c . This test uses the variation of T_c with respect to Gaussian broadening to compute the double delta summation. For dynamically unstable compounds, we applied large electronic smearing, lattice distortion, and pressure to stabilize imaginary phonon modes. We then calculated their EPC properties and incorporated these into the ML models. Between the two ML models, ALIGNN consistently outperforms CGCNN in predicting EPC properties especially after including the stabilized compounds with imaginary phonon and dynamical instability. Our ML-guided search demonstrates promising predictability for T_c values. For example, we predict SC in compounds with calculated dynamically stability such as TaNbC₂ (28.4 K), Nb₃B₃C (16.4 K), Y₂B₃C₂ (4.0 K), among others. In addition to studying dynamically stable compounds, we also focus on compounds with calculated dynamic instability, an area that, to our knowledge, has not been systematically explored before. We predicted SC in compounds showing dynamic instability such as Ca₅B₃N₆ (35 K), Pd₃CaB (7.0 K), some ternary Ru compounds,

TABLE III: DFPT calculated EPC results for MoB₂-type instability (outside of Γ), stabilized with electronic smearing of 0.10 Ry; SG is spacegroup, and ΔE_h is ΔE_h taken from MP database. Experimental results for some high-pressure T_c are also reported.

Compound	SG	ΔE_h (eV/atom) [65]	λ	ω_{log} (K)	T_c (K)	T_c^{Expt} (K)
Ca ₅ B ₃ N ₆	Im3'm	0.03	1.5	372	35.0 ^a	
MoB ₂	P6/mmm	0.156	2.12	209	27.3	32[34]
NbMoC ₂	R-3m	0.172	1.72	215	23.5	
TaMo ₂ C ₃	P-3m1	0.197	2.01	171	21.4	
TaMoC ₂	R-3m	0.15	1.69	189	20.3	
WVC ₂	R-3m	0.225	1.31	249	19.8	
TaTiWC ₃	P3m1	0.119	1.42	213	18.9	
ScC	P6 ₃ /mmc	0.6	0.95	410	18.5	
TaWC ₂	R-3m	0.211	2.04	129	16.3	
MoRuB ₂	Pmc2 ₁	0.09	1.29	202	15.6	
RuC	P-6m2	0.649	1.02	288	15.1	
RuVB ₂	Pmc2 ₁	0.073	1.09	255	15.0	
Ni ₃ AlC	Pm-3m	0.166	1.86	116	13.6	
Nb ₄ C ₃	Pm-3m	0.167	0.99	267	13.2	
Ta ₄ C ₃	Pm-3m	0.134	0.99	203	10.1	
RhC	F-43m	0.561	0.91	228	9.3	
MoC	F-43m	0.585	0.97	191	9.0	
Pd ₃ CaB	Pm-3m	0.0	1.23	96	7.0	
RuSc ₃ C ₄	C2/m	0.0	0.72	321	6.6	
Ta ₂ S ₂ C	P-3m1	0.007	0.69	268	5.1	
Mo ₃ ZrB ₂ C ₂	Amm2	0.046	0.64	282	4.0	
HfC	P-6m2	0.763	1.06	56	3.2	

^a Stabilized with electronic smearing of 0.06 Ry

MoRuB₂ (15.6 K), RuVB₂ (15.0 K), Pd₃CaB (7.0 K) and RuSc₃C₄ (6.6 K) with ΔE_h mostly below 0.1 eV/atom. With further refinement and larger dataset, our workflow can be improved in accurately predicting more SC compounds. In this regard, identifying metastable compounds with calculated dynamic instability, where soft phonon exhibit significant EPC contribution, plays a crucial role.

IV METHODS

A Convergence with respect to Brillouin zone sampling (k-point mesh)

To identify cases of convergence failure (i.e., incorrect prediction of SC/NSC) related to Brillouin zone sampling, we analyzed the variation of T_c with respect to Gaussian broadening (σ) in the double delta integration and developed a simple ansatz based on the converged results of MgB₂, as described in the "Convergence tests for MgB₂ and AlB₂ (Supplementary Figures S5–S10, Supplementary Tables S5–S6)" and "Convergence ansatz (Supplementary Figures S11–S14, Supplementary Tables S7–S9)" sections of the Supplemental Material (SM). This ansatz involves extracting T_c , similar to MgB₂, and estimating the decay parameter (A) in the exponential variation of T_c with σ ,

$$T_c = \exp(-A\sigma^{1/3} + B) \quad (2)$$

where A is the variable that quantifies the rate of exponential decay, and B is the constant associated with Debye temperature. Unconverged results show larger values of A , which decrease with denser \mathbf{k} -meshes. With larger \mathbf{k} - or

\mathbf{q} - grids, the T_c vs σ curve becomes less steep. Our convergence analysis of MgB_2 suggests that $A_{\text{MgB}_2} = 12\text{--}13$ can be used as a threshold for this study: calculations are considered as unconvolved for $A > A_{\text{MgB}_2}$, requiring a denser \mathbf{k} -mesh, while those with $A < A_{\text{MgB}_2}$ can be regarded as converged for accurate prediction.

B Computational details

Data extraction from the MP database, as well as input preparation for ground state calculations, calculation submission, result extraction and input preparation for ML studies, and plotting, were performed using the high-throughput electronic structure package (HTESP) [157]. A script, ‘fitting_elph_smearing.py’, is included in the HTESP package to compute the decay parameter from T_c vs. broadening σ data. Ground-state DFT and EPC calculations were performed using the QE code [173, 174]. Ultrasoft or norm-conserving pseudopotentials (PP) from the efficiency standard solid-state pseudopotentials (SSSP) dataset [175] were employed, with the replacement of projector-augmented wave (PAW) PPs by GBRV ultrasoft norm-conserving high-throughput PPs [176]. The exchange-correlation energy was approximated using the Perdew–Burke–Ehrnzerhof (PBE) generalized-gradient approximation (GGA) [177]. The Brillouin zone was sampled using a \mathbf{k} -point mesh from the MP database to compute the ground-state charge density for EPC calculations. The \mathbf{q} -point mesh required for EPC calculations was obtained by halving the \mathbf{k} -point mesh ($\mathbf{q} = \mathbf{k}/2$), with odd \mathbf{k} -points changed to even by adding 1 to it. The structures were fully relaxed using Broyden–Fletcher–Goldfarb–Shanno (BFGS) minimization [178] until the total energy and forces for ionic minimization converged within 10^{-5} Ry and 10^{-4} Ry/Bohr, respectively. The self-consistent electronic energy and charge density were minimized with a convergence threshold of 10^{-12} Ry. Similarly, the SCF convergence for phonon calculations is achieved with an energy cutoff of 10^{-14} . Starting from the default α_{mix} value of 0.7, it is reduced to 0.3 if the EPC calculation does not converge. A fine \mathbf{k} -point grid, twice the size of the \mathbf{k} -point mesh used for charge density convergence, was used for interpolating EPC matrix elements to compute double-delta integration and the λ . Gaussian smearing of 0.02 Ry was applied for charge-density optimization. To compute λ for various σ values, we computed double-delta integration using 10 broadening (σ) values ranging from 0.005 to 0.05 Ry for the \mathbf{k} -mesh. For the \mathbf{q} -mesh integration, a fixed smearing of 0.5 meV was employed. The reported results were obtained for $\sigma = 0.01$ Ry with a Coulomb potential μ_c^* of 0.16.

C Limitations

When evaluating the significance of machine-learning (ML) models trained on ab-initio data, it is essential to recognize both their capabilities and inherent limitations. First, the performance of any ML model is strongly dependent on the quality, diversity, and representativeness of its training dataset. Limited or biased datasets, which are common in computational materials science, can restrict a model’s predictive accuracy and transferability. Second, ML models are susceptible to overfitting, particularly when trained on small or noisy datasets, although careful validation procedures during model development can mitigate this issue to some extent. Third, the fidelity of ML predictions is ultimately bounded by the accuracy of the underlying ab-initio methods used to generate the training data. For example, the widely used isotropic Eliashberg approximation in superconductivity calculations neglects the inherently anisotropic and multi-band character of electron–phonon coupling. Although fully solving the anisotropic Migdal–Eliashberg equations (e.g., using EPW) yield more accurate estimates of superconducting properties, they are not computationally practical for large scale data generation. Consequently, ML models trained on data obtained from the isotropic Eliashberg approximation can function as efficient screening tools to identify promising candidate materials, which may then be examined with more accurate, anisotropic, and computationally demanding methods.

V Data availability

Data computed and utilized in this study are tabulated in Supplementary Tables S10–S17, Tables. II and III. The raw data can be downloaded from the Figshare platform [179].

VI Acknowledgements

We thank Dr. Paul C. Canfield for the funding support, initiating the idea of searching for new phonon-mediated superconductors among boron and carbon compounds, and the helpful discussion throughout the project.

VII Funding

This work was supported by Ames National Laboratory LDRD and U.S. Department of Energy, Office of Basic Energy Science, Division of Materials Sciences and Engineering. Ames National Laboratory is operated for the U.S. Department of Energy by Iowa State University under Contract No. DE-AC02-07CH11358.

VIII Author information

A Authors and Affiliations

Ames National Laboratory, Ames, Iowa 50011, USA

Niraj K. Nepal, Lin-Lin Wang

Department of Physics and Astronomy, Iowa State University, Ames, Iowa 50011, USA

Lin-Lin Wang

B Contributions

L.-L.W. conceived and supervised the work. N.K.N. and L.-L.W. designed and performed the high throughput calculations with the machine learning guided approach. N.K.N. developed the ansatz to test the convergence of Tc calculation. All authors discussed the results and contributed to the final manuscript.

C Corresponding author

Correspondence to Niraj K. Nepal (nepalneeraz@gmail.com)

IX Competing interests

The authors declare no competing interests.

X References

- [1] A. Drozdov, M. Eremets, I. Troyan, V. Ksenofontov, and S. I. Shylin, Conventional superconductivity at 203 kelvin at high pressures in the sulfur hydride system, *Nature* **525**, 73 (2015).
- [2] L. Ma, K. Wang, Y. Xie, X. Yang, Y. Wang, M. Zhou, H. Liu, X. Yu, Y. Zhao, H. Wang, G. Liu, and Y. Ma, High-temperature superconducting phase in clathrate calcium hydride cah_6 up to 215 k at a pressure of 172 gpa, *Phys. Rev. Lett.* **128**, 167001 (2022).
- [3] Z. Li, X. He, C. Zhang, X. Wang, S. Zhang, Y. Jia, S. Feng, K. Lu, J. Zhao, J. Zhang, *et al.*, Superconductivity above 200 k discovered in superhydrides of calcium, *Nat. Commun.* **13**, 2863 (2022).
- [4] P. Kong, V. S. Minkov, M. A. Kuzovnikov, A. P. Drozdov, S. P. Besedin, S. Mozaffari, L. Balicas, F. F. Balakirev, V. B. Prakapenka, S. Chariton, *et al.*, Superconductivity up to 243 k in the yttrium-hydrogen system under high pressure, *Nat. Commun.* **12**, 5075 (2021).
- [5] I. A. Troyan, D. V. Semenok, A. G. Kvashnin, A. V. Sadakov, O. A. Sobolevskiy, V. M. Pudalov, A. G. Ivanova, V. B. Prakapenka, E. Greenberg, A. G. Gavriliuk, *et al.*, Anomalous high-temperature superconductivity in YH₆, *Adv. Mater.* **33**, 2006832 (2021).

[6] D. V. Semenok, I. A. Troyan, A. G. Ivanova, A. G. Kvashnin, I. A. Kruglov, M. Hanfland, A. V. Sadakov, O. A. Sobolevskiy, K. S. Pervakov, I. S. Lyubutin, *et al.*, Superconductivity at 253 k in lanthanum–yttrium ternary hydrides, *Materials Today* **48**, 18 (2021).

[7] Y. Li, J. Hao, H. Liu, Y. Li, and Y. Ma, The metallization and superconductivity of dense hydrogen sulfide, *J. Chem. Phys.* **140**, 174712 (2014).

[8] R. Akashi, M. Kawamura, S. Tsuneyuki, Y. Nomura, and R. Arita, First-principles study of the pressure and crystal-structure dependences of the superconducting transition temperature in compressed sulfur hydrides, *Phys. Rev. B* **91**, 224513 (2015).

[9] I. Errea, M. Calandra, C. J. Pickard, J. Nelson, R. J. Needs, Y. Li, H. Liu, Y. Zhang, Y. Ma, and F. Mauri, High-pressure hydrogen sulfide from first principles: A strongly anharmonic phonon-mediated superconductor, *Phys. Rev. Lett.* **114**, 157004 (2015).

[10] D. A. Papaconstantopoulos, B. M. Klein, M. J. Mehl, and W. E. Pickett, Cubic h_3s around 200 gpa: An atomic hydrogen superconductor stabilized by sulfur, *Phys. Rev. B* **91**, 184511 (2015).

[11] J.-N. Wang, X.-W. Yan, and M. Gao, High-temperature superconductivity in SrB_3C_3 and BaB_3C_3 predicted from first-principles anisotropic migdal-eliashberg theory, *Phys. Rev. B* **103**, 144515 (2021).

[12] L. Zhu, H. Liu, M. Somayazulu, Y. Meng, P. A. Guńka, T. B. Shiell, C. Kenney-Benson, S. Chariton, V. B. Prakapenka, H. Yoon, *et al.*, Superconductivity in SrB_3C_3 clathrate, *Phys. Rev. Res.* **5**, 013012 (2023).

[13] S. Di Cataldo, S. Qulaghasi, G. B. Bachelet, and L. Boeri, High-t c superconductivity in doped boron-carbon clathrates, *Phys. Rev. B* **105**, 064516 (2022).

[14] P. Zhang, X. Li, X. Yang, H. Wang, Y. Yao, and H. Liu, Path to high-t c superconductivity via rb substitution of guest metal atoms in the SrB_3C_3 clathrate, *Phys. Rev. B* **105**, 094503 (2022).

[15] N. Geng, K. P. Hilleke, L. Zhu, X. Wang, T. A. Strobel, and E. Zurek, Conventional high-temperature superconductivity in metallic, covalently bonded, binary-guest c-b clathrates, *J. Am. Chem. Soc.* (2023).

[16] J. Nagamatsu, N. Nakagawa, T. Muranaka, Y. Zenitani, and J. Akimitsu, Superconductivity at 39 k in magnesium diboride, *Nature* **410**, 63 (2001).

[17] S. L. Bud'ko, G. Lapertot, C. Petrovic, C. E. Cunningham, N. Anderson, and P. C. Canfield, Boron isotope effect in superconducting mgb_2 , *Phys. Rev. Lett.* **86**, 1877 (2001).

[18] K.-P. Bohnen, R. Heid, and B. Renker, Phonon dispersion and electron-phonon coupling in mgb_2 and alb_2 , *Phys. Rev. Lett.* **86**, 5771 (2001).

[19] D. Hinks, H. Claus, and J. Jorgensen, The complex nature of superconductivity in MgB_2 as revealed by the reduced total isotope effect, *Nature* **411**, 457 (2001).

[20] Y. Wang, T. Plackowski, and A. Junod, Specific heat in the superconducting and normal state (2–300 k, 0–16 t), and magnetic susceptibility of the 38 k superconductor MgB_2 : evidence for a multicomponent gap, *Phys. C: Supercond.* **355**, 179 (2001).

[21] S. Kazakov, M. Angst, J. Karpinski, I. Fita, and R. Puzniak, Substitution effect of zn and cu in MgB_2 on t_c and structure, *Solid State Commun.* **119**, 1 (2001).

[22] A. Tampieri, G. Celotti, S. Sprio, D. Rinaldi, G. Barucca, and R. Caciuffo, Effects of copper doping in MgB_2 superconductor, *Solid State Commun.* **121**, 497 (2002).

[23] M. Calandra, N. Vast, and F. Mauri, Superconductivity from doping boron icosahedra, *Phys. Rev. B* **69**, 224505 (2004).

[24] H. Xiang, Z. Li, J. Yang, J. Hou, and Q. Zhu, Electron-phonon coupling in a boron-doped diamond superconductor, *Phys. Rev. B* **70**, 212504 (2004).

[25] X. Blase, C. Adessi, and D. Connetable, Role of the dopant in the superconductivity of diamond, *Phys. Rev. Lett.* **93**, 237004 (2004).

[26] K. Müller and V. Narozhnyi, Interaction of superconductivity and magnetism in borocarbide superconductors, *Reports on Progress in Physics* **64**, 943 (2001).

[27] P. Martinez-Samper, H. Suderow, S. Vieira, J. Brison, N. Luchier, P. Lejay, and P. Canfield, Phonon-mediated anisotropic superconductivity in the y and lu nickel borocarbides, *Phys. Rev. B* **67**, 014526 (2003).

[28] K. Togano, P. Badica, Y. Nakamori, S. Oriomo, H. Takeya, and K. Hirata, Superconductivity in the metal rich Li-Pd-B ternary boride, *Phys. Rev. Lett.* **93**, 247004 (2004).

[29] G. F. Hardy and J. K. Hulm, The superconductivity of some transition metal compounds, *Phys. Rev.* **93**, 1004 (1954).

[30] A. Karki, Y. Xiong, I. Vekhter, D. Browne, P. Adams, D. Young, K. Thomas, J. Y. Chan, H. Kim, and R. Prozorov, Structure and physical properties of the noncentrosymmetric superconductor $\text{Mo}_3\text{Al}_2\text{C}$, *Phys. Rev. B* **82**, 064512 (2010).

[31] J. Kim, W. Xie, R. Kremer, V. Babizhetsky, O. Jepsen, A. Simon, K. Ahn, B. Raquet, H. Rakoto, J.-M. Broto, *et al.*, Strong electron-phonon coupling in the rare-earth carbide superconductor La_2C_3 , *Phys. Rev. B* **76**, 014516 (2007).

[32] G. Amano, S. Akutagawa, T. Muranaka, Y. Zenitani, and J. Akimitsu, Superconductivity at 18 K in yttrium sesquicarbide system, Y_2C_3 , *J. Phys. Soc. Japan* **73**, 530 (2004).

[33] F. Heiniger, E. Bucher, J. Maita, and P. Descouts, Superconducting and other electronic properties of La_3In , La_3Tl , and some related phases, *Phys. Rev. B* **8**, 3194 (1973).

[34] C. Pei, J. Zhang, Q. Wang, Y. Zhao, L. Gao, C. Gong, S. Tian, R. Luo, M. Li, W. Yang, Z.-Y. Lu, H. Lei, K. Liu, and Y. Qi, Pressure-induced Superconductivity at 32 K in MoB_2 , *National Science Review* 10.1093/nsr/nwad034 (2023), nwad034, <https://academic.oup.com/nsr/advance-article-pdf/doi/10.1093/nsr/nwad034/49182415/nwad034.pdf>.

[35] A. N. Kolmogorov, S. Shah, E. R. Margine, A. F. Bialon, T. Hammerschmidt, and R. Drautz, New superconducting and semiconducting fe-b compounds predicted with an ab initio evolutionary search, *Phys. Rev. Lett.* **105**, 217003 (2010).

[36] H. Gou, N. Dubrovinskaia, E. Bykova, A. A. Tsirlin, D. Kasinathan, W. Schnelle, A. Richter, M. Merlini, M. Hanfland, A. M. Abakumov, et al., Discovery of a superhard iron tetraboride superconductor, *Phys. Rev. Lett.* **111**, 157002 (2013).

[37] S. Baroni, S. De Gironcoli, A. Dal Corso, and P. Giannozzi, Phonons and related crystal properties from density-functional perturbation theory, *Rev. Mod. Phys.* **73**, 515 (2001).

[38] A. Dal Corso, Density-functional perturbation theory with ultrasoft pseudopotentials, *Phys. Rev. B* **64**, 235118 (2001).

[10] A. Floris, A. Sanna, M. Lüders, G. Profeta, N. Lathiotakis, M. Marques, C. Franchini, E. Gross, A. Continenza, and S. Massidda, Superconducting properties of MgB₂ from first principles, *Physica C: Supercond.* **456**, 45 (2007).

[40] A. Migdal, Interaction between electrons and lattice vibrations in a normal metal, *Sov. Phys. JETP* **7**, 996 (1958).

[41] G. Eliashberg, Interactions between electrons and lattice vibrations in a superconductor, *Sov. Phys. JETP* **11**, 696 (1960).

[42] P. B. Allen, Neutron spectroscopy of superconductors, *Phys. Rev. B* **6**, 2577 (1972).

[1] P. B. Allen and R. Dynes, Transition temperature of strong-coupled superconductors reanalyzed, *Phys. Rev. B* **12**, 905 (1975).

[44] E. R. Margine and F. Giustino, Anisotropic migdal-eliashberg theory using wannier functions, *Phys. Rev. B* **87**, 024505 (2013).

[45] F. Giustino, Electron-phonon interactions from first principles, *Rev. Mod. Phys.* **89**, 015003 (2017).

[46] G. Webb, F. Marsiglio, and J. Hirsch, Superconductivity in the elements, alloys and simple compounds, *Phys. C: Supercond. Appl.* **514**, 17 (2015).

[47] B. Lilia, R. Hennig, P. Hirschfeld, G. Profeta, A. Sanna, E. Zurek, W. E. Pickett, M. Amsler, R. Dias, M. I. Eremets, et al., The 2021 room-temperature superconductivity roadmap, *J. Phys. Condens. Matter.* **34**, 183002 (2022).

[48] S. Kharabadze, M. Meyers, C. R. Tomassetti, E. R. Margine, I. I. Mazin, and A. N. Kolmogorov, Thermodynamic stability of li-b-c compounds from first principles, *Phys. Chem. Chem. Phys.* **25**, 7344 (2023).

[49] V. Stanev, C. Oses, A. G. Kusne, E. Rodriguez, J. Paglione, S. Curtarolo, and I. Takeuchi, Machine learning modeling of superconducting critical temperature, *Npj Comput. Mater.* **4**, 29 (2018).

[50] B. Roter and S. Dordevic, Predicting new superconductors and their critical temperatures using machine learning, *Physica C: Superconductivity and its applications* **575**, 1353689 (2020).

[51] S. Xie, Y. Quan, A. Hire, B. Deng, J. DeStefano, I. Salinas, U. Shah, L. Fanfarillo, J. Lim, J. Kim, et al., Machine learning of superconducting critical temperature from eliashberg theory, *Npj Comput. Mater.* **8**, 14 (2022).

[52] S. R. Xie, G. R. Stewart, J. J. Hamlin, P. J. Hirschfeld, and R. G. Hennig, Functional form of the superconducting critical temperature from machine learning, *Phys. Rev. B* **100**, 174513 (2019).

[53] J. Zhang, Z. Zhu, X.-D. Xiang, K. Zhang, S. Huang, C. Zhong, H.-J. Qiu, K. Hu, and X. Lin, Machine learning prediction of superconducting critical temperature through the structural descriptor, *The Journal of Physical Chemistry C* **126**, 8922 (2022).

[54] C. J. Court and J. M. Cole, Magnetic and superconducting phase diagrams and transition temperatures predicted using text mining and machine learning, *Npj Comput. Mater.* **6**, 18 (2020).

[55] T. Konno, H. Kurokawa, F. Nabeshima, Y. Sakishita, R. Ogawa, I. Hosako, and A. Maeda, Deep learning model for finding new superconductors, *Phys. Rev. B* **103**, 014509 (2021).

[36] National institute of materials science, materials information station, http://supercon.nims.go.jp/index_en.html, SuperCon (2018).

[9] K. Choudhary and K. Garrity, Designing high-*tc* superconductors with bcs-inspired screening, density functional theory, and deep-learning, *Npj Comput. Mater.* **8**, 244 (2022).

[58] T. F. Cerqueira, A. Sanna, and M. A. Marques, Sampling the whole materials space for conventional superconducting materials, arXiv preprint arXiv:2307.10728 (2023).

[59] J. B. Gibson, A. C. Hire, P. M. Dee, O. Barrera, B. Geisler, P. J. Hirschfeld, and R. G. Hennig, Accelerating superconductor discovery through tempered deep learning of the electron-phonon spectral function, *npj Computational Materials* **11**, 7 (2025).

[60] M. J. Hutzcheon, A. M. Shipley, and R. J. Needs, Predicting novel superconducting hydrides using machine learning approaches, *Phys. Rev. B* **101**, 144505 (2020).

[61] E. A. Pogue, A. New, K. McElroy, N. Q. Le, M. J. Pekala, I. McCue, E. Gienger, J. Domenico, E. Hedrick, T. M. McQueen, et al., Closed-loop machine learning for discovery of novel superconductors, arXiv preprint arXiv:2212.11855 (2022).

[62] N. K. Nepal, P. C. Canfield, and L.-L. Wang, Imaginary phonon modes and phonon-mediated superconductivity in y 2 c 3, *Phys. Rev. B* **109**, 054518 (2024).

[63] C. Jiang, E. Beneduce, M. Baggio, C. Setty, and A. Zacccone, Possible enhancement of the superconducting due to sharp kohn-like soft phonon anomalies, *J. Phys.: Condens. Matter* **35**, 164003 (2023).

[64] C. Setty, M. Baggio, and A. Zacccone, Anharmonic phonon damping enhances the *t c* of bcs-type superconductors, *Phys. Rev. B* **102**, 174506 (2020).

[65] A. Jain, S. P. Ong, G. Hautier, W. Chen, W. D. Richards, S. Dacek, S. Cholia, D. Gunter, D. Skinner, G. Ceder, et al., Commentary: The materials project: A materials genome approach to accelerating materials innovation, *APL Mater.* **1**, 011002 (2013).

[66] S. P. Ong, S. Cholia, A. Jain, M. Brafman, D. Gunter, G. Ceder, and K. A. Persson, The materials application programming interface (api): A simple, flexible and efficient api for materials data based on representational state transfer (rest) principles, *Comput. Mater. Sci.* **97**, 209 (2015).

[67] S. P. Ong, W. D. Richards, A. Jain, G. Hautier, M. Kocher, S. Cholia, D. Gunter, V. L. Chevrier, K. A. Persson, and G. Ceder, Python materials genomics (pymatgen): A robust, open-source python library for materials analysis, *Comput. Mater. Sci.* **68**, 314 (2013).

[68] B. Matthias and J. Hulm, A search for new superconducting compounds, *Phys. Rev.* **87**, 799 (1952).

[69] A. Giorgi, E. Szklarz, E. Storms, and A. Bowman, Investigation of Ta₂C, Nb₂C, and V₂C for superconductivity, *Phys. Rev.* **129**, 1524 (1963).

[70] R. Willens, E. Buehler, and B. Matthias, Superconductivity of the transition-metal carbides, *Phys. Rev.* **159**, 327 (1967).

[71] N. Morton, B. James, G. Wostenholm, D. Pomfret, M. Davies, and J. Dykins, Superconductivity of molybdenum and tungsten carbides, *J. Less Common Met.* **25**, 97 (1971).

[72] D. Johnston, Superconductivity in a new ternary structure class of boride compounds, *Solid State Commun.* **24**, 699 (1977).

[73] P. Rogl, New ternary borides with YCrB₄-type structure, *Mater. Res. Bull.* **13**, 519 (1978).

[74] R. Sobczak and P. Rogl, Magnetic behavior of new ternary metal borides with YCrB₄-type structure, *J. Solid State Chem.* **27**, 343 (1979).

[75] H. Ku, G. Meisner, F. Acker, and D. Johnston, Superconducting and magnetic properties of new ternary borides with the CeCo₃B₂-type structure, *Solid State Commun.* **35**, 91 (1980).

[76] P. Lejay, B. Chevalier, J. Etourneau, and P. Hagenmuller, Influence of some metal substitutions on the superconducting behaviour of molybdenum borocarbide, *J. Less Common Met.* **82**, 193 (1981).

[77] T. Sakai, G.-Y. Adachi, and J. Shiokawa, Electrical properties of rare earth diborodicarbides (RB₂C₂-type layer compounds), *J. Less Common Met.* **84**, 107 (1982).

[78] H. Ku and D. Lin, Low temperature magnetic order of the new ternary rare earth compounds (RRuB₄) with the YCrB₄-type structure, *J. Less Common Met.* **127**, 35 (1987).

[79] A. Kutty, C. Pillai, C. Karunakaran, and S. Vaidya, Low temperature electrical resistivity studies and search for superconductivity in Ti-B system, *Solid State Commun.* **70**, 1123 (1989).

[80] H. Boller and K. Hiebl, Quaternary pseudo-intercalation phases tx [Nb₂S₂C](T V, Cr, Mn, Fe, Co, Ni, Cu) and metastable Nb₂S₂C formed by topochemical synthesis, *J. Alloys Compd.* **183**, 438 (1992).

[81] J. Schirber, D. Overmyer, B. Morosin, E. Venturini, R. Baughman, D. Emin, H. Klesnar, and T. Aselage, Pressure dependence of the superconducting transition temperature in single-crystal NbB_x (x near 2) with T_c = 9.4 K, *Phys. Rev. B* **45**, 10787 (1992).

[82] R. J. Cava, B. Batlogg, T. Siegrist, J. J. Krajewski, W. F. Peck, S. Carter, R. J. Felder, H. Takagi, and R. B. van Dover, Superconductivity in $\text{rpt}_2\text{b}_2\text{c}$, *Phys. Rev. B* **49**, 12384 (1994).

[83] R. Cava, T. Siegrist, B. Batlogg, H. Takagi, H. Eisaki, S. Carter, J. Krajewski, and W. Peck Jr, Elementary physical properties and crystal structures of LaRh₂B₂C and LaIr₂B₂C, *Phys. Rev. B* **50**, 12966 (1994).

[84] R. Cava, H. Takagi, B. Batlogg, H. Zandbergen, J. Krajewski, W. Peck Jr, R. Van Dover, R. Felder, T. Siegrist, K. Mizuhashi, et al., Superconductivity at 23 K in yttrium palladium boride carbide, *Nature* **367**, 146 (1994).

[85] Y. Sun, I. Rusakova, R. Meng, Y. Cao, P. Gautier-Picard, and C. Chu, The 23 k superconducting phase YPd₂B₂C, *Physica C Supercond.* **230**, 435 (1994).

[86] H. Zandbergen, J. Jansen, R. Cava, J. Krajewskii, and W. Peck Jr, Structure of the 13-k superconductor La₃Ni₂B₂N₃ and the related phase lanibn, *Nature* **372**, 759 (1994).

[87] K. Kadowaki, H. Takeya, K. Hirata, and T. Mochiku, Magnetism and superconductivity in RET₂B₂C (RE Y and T Ni, Co) systems, *Phys. B: Condens. Matter.* **206**, 555 (1995).

[88] H. Michor, T. Holubar, C. Dusek, and G. Hilscher, Specific-heat analysis of rare-earth transition-metal borocarbides: An estimation of the electron-phonon coupling strength, *Phys. Rev. B* **52**, 16165 (1995).

[89] R. W. Henn, W. Schnelle, R. K. Kremer, and A. Simon, Bulk superconductivity at 10 k in the layered compounds $Y_2C_2I_2$ and $Y_2C_2Br_2$, *Phys. Rev. Lett.* **77**, 374 (1996).

[90] A. Simon, Superconductivity and chemistry, *Angew. Chem. Int. Ed.* **36**, 1788 (1997).

[91] I. Yanson, V. Fisun, A. Jansen, P. Wyder, P. Canfield, B. Cho, C. Tomy, and D. M. Paul, Observation of electron-phonon interaction with soft phonons in superconducting RNi₂B₂C, *Phys. Rev. Lett.* **78**, 935 (1997).

[92] K. Ahn, H. Mattausch, and A. Simon, Metal substitution in layered superconducting La₂C₂Br₂, *Z. Anorg. Allg. Chem.* **624**, 175 (1998).

[93] K. Ohoyama, T. Onimaru, H. Onodera, H. Yamauchi, and Y. Yamaguchi, Antiferromagnetic structure with the uniaxial anisotropy in the tetragonal LaB₂C₂ type compound, NdB₂C₂, *J. Phys. Soc. Japan* **69**, 2623 (2000).

[94] H. Bitterlich, W. Löser, H.-G. Lindenkreuz, and L. Schultz, Superconducting YNi₂B₂C-and YPd₂B₂C-phase formation from undercooled melts, *J. Alloys Compd.* **325**, 285 (2001).

[95] C. Buzea and T. Yamashita, Review of the superconducting properties of MgB₂, *Supercond. Sci. Technol.* **14**, R115 (2001).

[96] V. A. Gasparov, N. Sidorov, I. I. Zver'kova, and M. Kulakov, Electron transport in diborides: observation of superconductivity in ZrB₂, *J. Exp. Theor. Phys.* **73**, 532 (2001).

[97] K. Sakamaki, H. Wada, H. Nozaki, Y. Ōnuki, and M. Kawai, van der waals type carbosulfide superconductor, *Solid State Commun.* **118**, 113 (2001).

[98] H. Rosner, R. Weht, M. Johannes, W. Pickett, and E. Tosatti, Superconductivity near ferromagnetism in MgCNi₃, *Phys. Rev. Lett.* **88**, 027001 (2001).

[99] A. Kawano, Y. Mizuta, H. Takagiwa, T. Muranaka, and J. Akimitsu, The superconductivity in Re-B system, *J. Phys. Soc. Japan* **72**, 1724 (2003).

[44] A. Czopnik, N. Shitsevalova, V. Pluzhnikov, A. Krivchikov, Y. Paderno, and Y. Onuki, Low-temperature thermal properties of yttrium and lutetium dodecaborides, *J. Condens. Matter Phys.* **17**, 5971 (2005).

[101] R. P. Smith, T. E. Weller, C. A. Howard, M. P. Dean, K. C. Rahnejat, S. S. Saxena, and M. Ellerby, Superconductivity in graphite intercalation compounds, *Phys. C: Supercond. Appl.* **514**, 50 (2015).

[102] H. Takeya, K. Hirata, K. Yamaura, K. Togano, M. El Massalami, R. Rapp, F. Chaves, and B. Ouladdiaf, Low-temperature specific-heat and neutron-diffraction studies on Li₂Pd₃B and Li₂Pt₃B superconductors, *Phys. Rev. B* **72**, 104506 (2005).

[103] A. Bortolozo, O. Sant'Anna, M. Da Luz, C. Dos Santos, A. Pereira, K. Trentin, and A. Machado, Superconductivity in the Nb₂SnC compound, *Solid State Commun.* **139**, 57 (2006).

[104] R. Lortz, Y. Wang, U. Tutsch, S. Abe, C. Meingast, P. Popovich, W. Knafo, N. Shitsevalova, Y. B. Paderno, and A. Junod, Superconductivity mediated by a soft phonon mode: Specific heat, resistivity, thermal expansion, and magnetization of YB₆, *Phys. Rev. B* **73**, 024512 (2006).

[105] V. Anand, C. Geibel, and Z. Hossain, Superconducting and magnetic properties of Pt-based borocarbides RPt₂B₂C (R= La, Ce, Pr), *Phys. C: Supercond. Appl.* **460**, 636 (2007).

[106] S. Kuroiwa, Y. Tomita, A. Sugimoto, T. Ekino, and J. Akimitsu, Specific heat and tunneling spectroscopy study of NbB₂ with maximum T_c 10 K, *J. Phys. Soc. Japan* **76**, 094705 (2007).

[107] P. Manfrinetti, M. Pani, S. Dhar, and R. Kulkarni, Structure, transport and magnetic properties of mgni₃b₂, *J. Alloys Compd.* **428**, 94 (2007).

[108] D. Music and J. M. Schneider, The correlation between the electronic structure and elastic properties of nanolaminates, *Jom* **59**, 60 (2007).

[109] Y. Singh, A. Niazi, M. Vannette, R. Prozorov, and D. Johnston, Superconducting and normal-state properties of the layered boride OsB₂, *Phys. Rev. B* **76**, 214510 (2007).

[110] H. Takeya, S. Kasahara, M. El Massalami, T. Mochiku, K. Hirata, and K. Togano, Physical properties of Li₂Pd₃B and Li₂Pt₃B superconductors, in *Materials Science Forum*, Vol. 561 (Trans Tech Publ, 2007) pp. 2079–2082.

[42] A. Bortolozo, Z. Fisk, O. Sant'Anna, C. Dos Santos, and A. Machado, Superconductivity in Nb₂InC, *Physica C Supercond* **469**, 256 (2009).

[112] L. Huerta, A. Duran, R. Falconi, M. Flores, and R. Escamilla, Comparative study of the core level photoemission of the ZrB₂ and ZrB₁₂, *Physica C Supercond* **470**, 456 (2010).

[113] Y. Singh, C. Martin, S. Bud'Ko, A. Ellern, R. Prozorov, and D. Johnston, Multigap superconductivity and shubnikov–de haas oscillations in single crystals of the layered boride OsB₂, *Phys. Rev. B* **82**, 144532 (2010).

[114] A. J. d. S. Machado, A. Costa, C. Nunes, C. Dos Santos, T. Grant, and Z. Fisk, Superconductivity in Mo₅SiB₂, *Solid State Commun.* **151**, 1455 (2011).

[115] H. Mizoguchi, T. Kuroda, T. Kamiya, and H. Hosono, LaCo₂B₂: A co-based layered superconductor with a ThCr₂Si₂-type structure, *Phys. Rev. Lett.* **106**, 237001 (2011).

[116] H. Takeya and M. ElMassalami, Linear magnetoresistivity in the ternary AM₂B₂ and A₃Rh₈B₆ phases (a= ca, sr; m= rh, ir), *Phys. Rev. B* **84**, 064408 (2011).

[117] N. Imamura, H. Mizoguchi, and H. Hosono, Superconductivity in LaTMBN and La₃TM₂B₂N₃ (tm= transition metal) synthesized under high pressure, *J. Am. Chem. Soc.* **134**, 2516 (2012).

[41] M. Kayhan, E. Hildebrandt, M. Frotscher, A. Senyshyn, K. Hofmann, L. Alff, and B. Albert, Neutron diffraction and observation of superconductivity for tungsten borides, WB and W₂B₄, *Solid State Sci.* **14**, 1656 (2012).

[119] H. Takeya, M. ElMassalami, L. A. Terrazos, R. E. Rapp, R. B. Capaz, H. Fujii, Y. Takano, M. Doerr, and S. A. Granovsky, Probing the electronic properties of ternary AnM₃n-1B₂n (n= 1: A= ca, sr; m= rh, ir and n= 3: A= ca, sr; m= rh) phases: observation of superconductivity, *Sci Technol Adv Mate* (2013).

[120] B. Wang and K. Ohgushi, Superconductivity in anti-post-perovskite vanadium compounds, *Sci. Rep.* **3**, 3381 (2013).

[121] V. Babizhetsky, O. Jepsen, R. Kremer, A. Simon, B. Ouladdiaf, and A. Stolovits, Structure and bonding of superconducting LaC₂, *J. Condens. Matter Phys.* **26**, 025701 (2013).

[122] C. Xu, L. Wang, Z. Liu, L. Chen, J. Guo, N. Kang, X.-L. Ma, H.-M. Cheng, and W. Ren, Large-area high-quality 2d ultrathin mo₂c superconducting crystals, *Nat. Mater.* **14**, 1135 (2015).

[123] L. E. Corrêa, M. Da Luz, B. De Lima, O. Cigarroa, A. Da Silva, G. C. Coelho, Z. Fisk, and A. J. S. Machado, Ta₅GeB₂: New T₂ superconductor phase, *J. Alloys Compd.* **660**, 44 (2016).

[124] R. Escamilla, E. Carvajal, M. Cruz-Irisson, F. Morales, L. Huerta, and E. Verdin, Xps study of the electronic density of states in the superconducting Mo₂B and Mo₂BC compounds, *J. Mater. Sci.* **51**, 6411 (2016).

[125] Y. Takada, Theory of superconductivity in graphite intercalation compounds, *arXiv preprint arXiv:1601.02753* (2016).

[126] N. Barbero, T. Shiroka, B. Delley, T. Grant, A. J. d. S. Machado, Z. Fisk, H.-R. Ott, and J. Mesot, Doping-induced superconductivity of ZrB₂ and HfB₂, *Phys. Rev. B* **95**, 094505 (2017).

[127] P. A. Kumar, A. Satya, P. S. Reddy, M. Sekar, V. Kanchana, G. Vaitheeswaran, A. Mani, S. Kalavathi, and N. C. Shekar, Structural and low temperature transport properties of Fe₂B and FeB systems at high pressure, *J Phys Chem Solids* **109**, 18 (2017).

[128] N. Sluchanko, V. Glushkov, S. Demishev, A. Azarevich, M. Anisimov, A. Bogach, V. Voronov, S. Gavrilkin, K. Mitsen, A. Kuznetsov, et al., Lattice instability and enhancement of superconductivity in YB₆, *Phys. Rev. B* **96**, 144501 (2017).

[129] E. M. Carnicom, W. Xie, T. Klimczuk, J. Lin, K. Górnicka, Z. Sobczak, N. P. Ong, and R. J. Cava, TaRh₂B₂ and NbRh₂B₂: Superconductors with a chiral noncentrosymmetric crystal structure, *Science advances* **4**, eaar7969 (2018).

[130] J. Singh, A. Jayaraj, D. Srivastava, S. Gayen, A. Thamizhavel, and Y. Singh, Possible multigap type-i superconductivity in the layered boride RuB₂, *Phys. Rev. B* **97**, 054506 (2018).

[131] P. Biswas, F. N. Rybakov, R. Singh, S. Mukherjee, N. Parzyk, G. Balakrishnan, M. R. Lees, C. Dewhurst, E. Babaev, A. Hillier, et al., Coexistence of type-I and type-II superconductivity signatures in ZrB₁₂ probed by muon spin rotation measurements, *Phys. Rev. B* **102**, 144523 (2020).

[132] S. Sharma, K. Motla, J. Beare, M. Nugent, M. Pula, T. Munsie, A. Hillier, R. Singh, G. Luke, et al., Fully gapped superconductivity in centrosymmetric and noncentrosymmetric Re-B compounds probed with μ sr, *Phys. Rev. B* **103**,

104507 (2021).

[133] C. Pei, J. Zhang, C. Gong, Q. Wang, L. Gao, Y. Zhao, S. Tian, W. Cao, C. Li, Z.-Y. Lu, et al., Pressure induced superconductivity in WB2 and ReB2 through modifying the b layers, arXiv preprint arXiv:2111.11909 (2021).

[134] S. Datta, S. Howlader, R. P. Singh, G. Sheet, et al., Anisotropic superconductivity in ZrB12 near the critical bogomolnyi point, *Phys. Rev. B* **105**, 094504 (2022).

[135] S. Chaudhary, J. Singh, A. Consiglio, D. Di Sante, R. Thomale, Y. Singh, et al., Role of electronic correlations in the kagome-lattice superconductor LaRh3B2, *Phys. Rev. B* **107**, 085103 (2023).

[136] K. Kurata and T. Muranaka, Superconducting properties of pt-type and bct-type YRh4B4, *Supercond. Sci. Technol.* **36**, 085005 (2023).

[137] A. Arko, G. Crabtree, J. Ketterson, F. Mueller, P. Walch, L. Windmiller, Z. Fisk, R. Hoyt, A. Mota, R. Viswanathan, et al., Large electron—phonon interaction but low-temperature superconductivity in LaB6, *Int. J. Quantum Chem.* **9**, 569 (1975).

[138] G. Schell, H. Winter, H. Rietschel, and F. Gompf, Electronic structure and superconductivity in metal hexaborides, *Phys. Rev. B* **25**, 1589 (1982).

[139] G. Strukova, V. Degtyareva, D. Shovkun, V. Zverev, V. Kiiko, A. Ionov, and A. Chaika, Superconductivity in the Re-B system, arXiv e-prints , cond (2001).

[140] M. Johannes and W. Pickett, Electronic structure of ZnCNi3, *Phys. Rev. B* **70**, 060507 (2004).

[37] M.-S. Park, J. Giim, S.-H. Park, Y. Lee, S. Lee, and E. Choi, Physical properties of zncni3: comparison with superconducting MgCNi3, *Supercond. Sci. Technol.* **17**, 274 (2003).

[142] S. Heguri, N. Kawade, T. Fujisawa, A. Yamaguchi, A. Sumiyama, K. Tanigaki, and M. Kobayashi, Superconductivity in the graphite intercalation compound BaC6, *Phys. Rev. Lett.* **114**, 247201 (2015).

[143] A. K. Iyer, Y. Zhang, J. P. Scheifers, and B. P. Fokwa, Structural variations, relationships and properties of M2B metal borides, *J. Solid State Chem.* **270**, 618 (2019).

[144] S. Ma, K. Bao, Q. Tao, L. Li, Y. Huang, X. Huang, Y. Zhao, C. Xu, P. Zhu, and T. Cui, Revealing the unusual rigid boron chain substructure in hard and superconductive tantalum monoboride, *Chem. Eur. J.* **25**, 5051 (2019).

[145] T. Shang, W. Xie, J. Zhao, Y. Chen, D. J. Gawryluk, M. Medarde, M. Shi, H. Yuan, E. Pomjakushina, and T. Shiroka, Multigap superconductivity in centrosymmetric and noncentrosymmetric rhenium-boron superconductors, *Phys. Rev. B* **103**, 184517 (2021).

[146] S. Nakamae, A. Gauzzi, F. Ladieu, D. L'hôte, N. Emery, C. Hérold, J. Marêché, P. Lagrange, and G. Loupias, Absence of superconductivity down to 80 mK in graphite intercalated BaC6, *Solid State Commun.* **145**, 493 (2008).

[147] J. Chacón-Torres and T. Pichler, Defect modulated raman response of KC8 single crystals, *Phys. Status Solidi (b)* **248**, 2744 (2011).

[148] U. Burkhardt, V. Gurin, F. Haarmann, H. Borrmann, W. Schnelle, A. Yaresko, and Y. Grin, On the electronic and structural properties of aluminum diboride Al_{0.9}B₂, *J Solid State Chem.* **177**, 389 (2004).

[149] M. Bäcker, A. Simon, R. K. Kremer, H.-J. Mattausch, R. Dronskowski, and J. Rouxel, Superconductivity in intercalated and substituted Y2Br2C2, *Angew. Chem. Int. Ed. Engl.* **35**, 752 (1996).

[150] M. Kobayashi, T. Enoki, H. Inokuchi, M. Sano, A. Sumiyama, Y. Oda, and H. Nagano, Superconductivity in the first stage rubidium graphite intercalation compound C8Rb, *Synth. Met.* **12**, 341 (1985).

[151] I. Bat'Ko, M. Bat'Kova, K. Flachbart, V. Filippov, Y. B. Paderno, N. Y. Shicevalova, and T. Wagner, Electrical resistivity and superconductivity of LaB6 and LuB12, *J. Alloys Compd.* **217**, L1 (1995).

[152] S. Datta, A. Vasdev, S. Halder, J. Singh, Y. Singh, and G. Sheet, Spectroscopic signature of two superconducting gaps and their unusual field dependence in RuB2, *J. Phys.: Condens. Matter.* **32**, 315701 (2020).

[46] E. Karaca, P. J. P. Byrne, P. J. Hasnip, and M. Probert, Prediction of phonon-mediated superconductivity in new Ti-based M2AX phases, *Scientific reports* **12**, 13198 (2022).

[154] T. He, Q. Huang, A. Ramirez, Y. Wang, K. Regan, N. Rogado, M. Hayward, M. Haas, J. Slusky, K. Inumara, et al., Superconductivity in the non-oxide perovskite MgCNi3, *Nature* **411**, 54 (2001).

[155] L. Toth, High superconducting transition temperatures in the molybdenum carbide family of compounds, *JLCM.* **13**, 129 (1967).

[156] J. Kim, L. Boeri, J. O'Brien, F. Razavi, and R. Kremer, Superconductivity in heavy alkaline-earth intercalated graphites, *Phys. Rev. Lett.* **99**, 027001 (2007).

[157] N. K. Nepal, P. C. Canfield, and L.-L. Wang, HTESP (high-throughput electronic structure package): a package for the high-throughput *ab initio* calculations (2024), arXiv:2406.04537 [physics.comp-ph].

[158] T. Xie and J. C. Grossman, Crystal graph convolutional neural networks for an accurate and interpretable prediction of material properties, *Phys. Rev. Lett.* **120**, 145301 (2018).

[159] K. Choudhary and B. DeCost, Atomistic line graph neural network for improved materials property predictions, *Npj Comput. Mater.* **7**, 185 (2021).

[160] H. Tran and T. N. Vu, Machine-learning approach for discovery of conventional superconductors, *Phys. Rev. Mater.* **7**, 054805 (2023).

[161] Q. Li, D. Zhou, H. Wang, W. Chen, B. Wu, Z. Wu, and W. Zheng, Crystal and electronic structures of superhard B2CN: An ab initio study, *Solid State Commun.* **152**, 71 (2012).

[162] D. Y. Yan, M. Yang, C. Wang, P. Song, C. Yi, and Y. Shi, Superconductivity in centrosymmetric topological superconductor candidate TaC, *Supercond. Sci. Technol.* **34**, 035025 (2021).

[163] R. Jha and V. Awana, Vacuum encapsulated synthesis of 11.5 K NbC superconductor, *J. Supercond. Nov. Magn.* **25**, 1421 (2012).

[164] H. Hillebrecht and K. Gebhardt, Crystal structures from a building set: The first boridecarbides of niobium, *Angew. Chem. Int. Ed.* **40**, 1445 (2001).

[165] G. Amano, S. Akutagawa, T. Muranaka, Y. Zenitani, and J. Akimitsu, Superconductivity at 18 K in yttrium sesquicarbide system, Y₂C₃, *J. Phys. Soc. Japan* **73**, 530 (2004).

[166] J. Kim, W. Xie, R. Kremer, V. Babizhetsky, O. Jepsen, A. Simon, K. Ahn, B. Raquet, H. Rakoto, J.-M. Broto, *et al.*, Strong electron-phonon coupling in the rare-earth carbide superconductor La₂C₃, *Phys. Rev. B* **76**, 014516 (2007).

[167] G. Zhao and B. Harmon, Phonon anomalies in β -phase Ni_xAl_{1-x} alloys, *Phys. Rev. B* **45**, 2818 (1992).

[168] G. Zhao and B. Harmon, Electron-phonon interactions and the phonon anomaly in β -phase NiTi, *Phys. Rev. B* **48**, 2031 (1993).

[169] L.-L. Wang, N. K. Nepal, and P. C. Canfield, Origin of charge density wave in topological semimetals sral4 and eual4, *Commun. Phys.* **7**, 111 (2024).

[170] A. Karki, Y. Xiong, I. Vekhter, D. Browne, P. Adams, D. Young, K. Thomas, J. Y. Chan, H. Kim, and R. Prozorov, Structure and physical properties of the noncentrosymmetric superconductor Mo₃Al₂C, *Phys. Rev. B* **82**, 064512 (2010).

[171] J.-T. Zhao, Z.-C. Dong, J. Vaughey, J. E. Ostenson, and J. D. Corbett, Synthesis, structures and properties of cubic R₃In and R₃InZ phases (R= Y, La; Z= B, C, N, O): The effect of interstitial Z on the superconductivity of La₃In, *J. Alloys Compd.* **230**, 1 (1995).

[172] M. Wörle, H. M. zu Altenschildesche, and R. Nesper, Synthesis, properties and crystal structures of α -Ca₃(BN₂)₂ and Ca_{9+x}(BN₂, CBN) 6—two compounds with BN₂₃- and CBN₄- anions, *J. Alloys Compd.* **264**, 107 (1998).

[173] P. Giannozzi, S. Baroni, N. Bonini, M. Calandra, R. Car, C. Cavazzoni, D. Ceresoli, G. L. Chiarotti, M. Cococcioni, I. Dabo, *et al.*, QUANTUM ESPRESSO: a modular and open-source software project for quantum simulations of materials, *J. Phys.: Condens. Matter.* **21**, 395502 (2009).

[174] P. Giannozzi, O. Andreussi, T. Brumme, O. Bunau, M. B. Nardelli, M. Calandra, R. Car, C. Cavazzoni, D. Ceresoli, M. Cococcioni, *et al.*, Advanced capabilities for materials modelling with Quantum ESPRESSO, *J. Phys.: Condens. Matter.* **29**, 465901 (2017).

[175] G. Prandini, A. Marrazzo, I. E. Castelli, N. Mounet, and N. Marzari, Precision and efficiency in solid-state pseudopotential calculations, *Npj Comput. Mater.* **4**, 1 (2018).

[176] K. F. Garrity, J. W. Bennett, K. M. Rabe, and D. Vanderbilt, Pseudopotentials for high-throughput DFT calculations, *Comput. Mater. Sci.* **81**, 446 (2014).

[177] J. P. Perdew, K. Burke, and M. Ernzerhof, Generalized gradient approximation made simple, *Phys. Rev. Lett.* **77**, 3865 (1996).

[178] Y.-H. Dai, Convergence properties of the BFGS algorithm, *SIAM J. Optim.* **13**, 693 (2002).

[179] N. K. Nepal and L. L. Wang, Machine-learning Guided Search for Phonon-mediated Superconductivity in Boron and Carbon Compounds 10.6084/m9.figshare.28557776.v1 (2025).

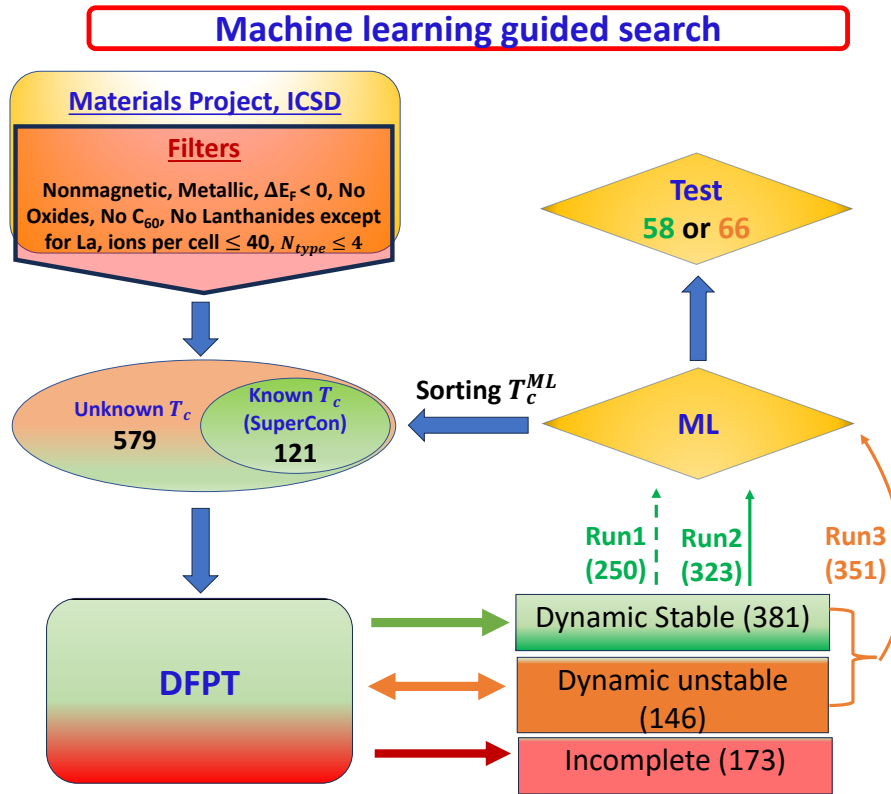


FIG. 1: Machine learning workflow. The numbers are the counts of compounds involved in each step. See main text for the detailed summary.

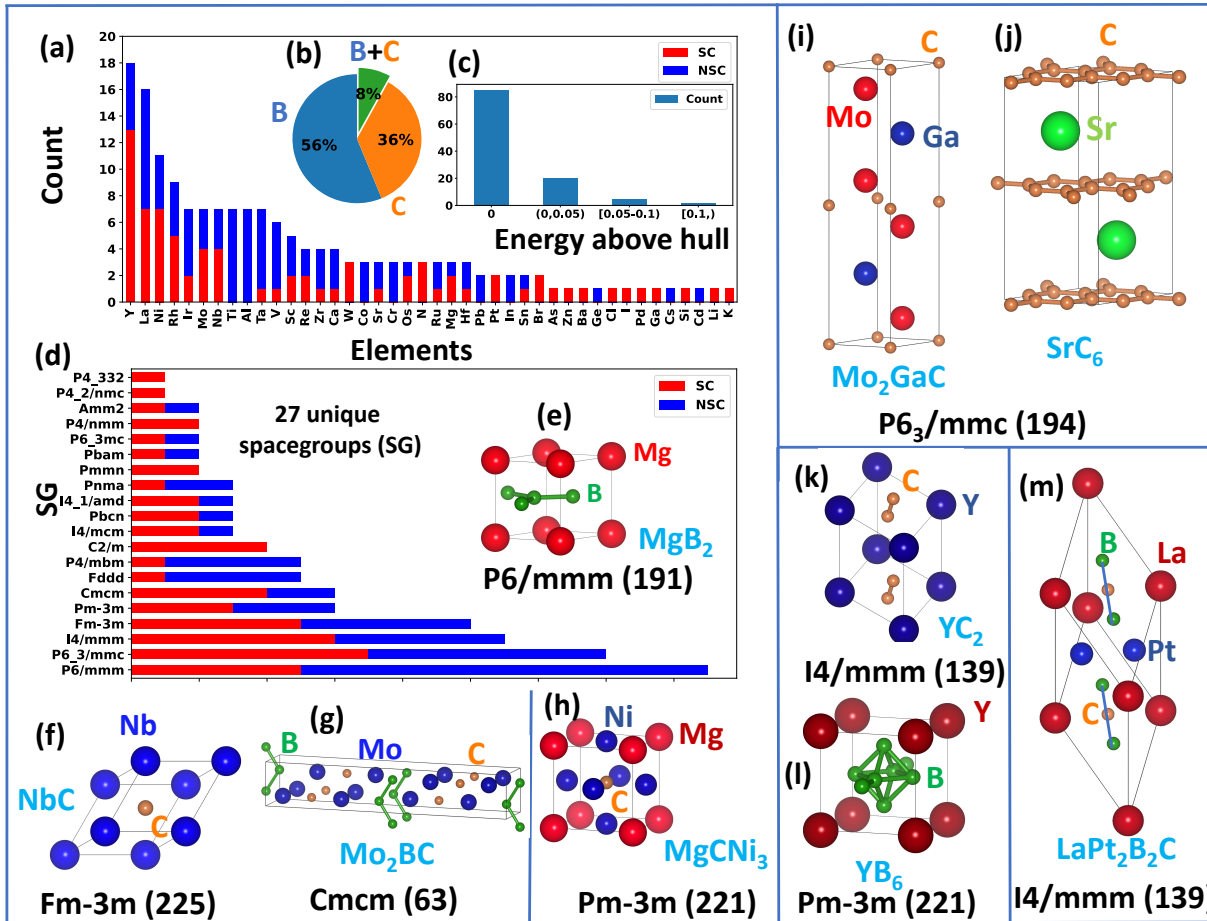


FIG. 2: Statistical description of dynamically stable 113 compounds, whose (non-) superconductivity have been experimentally measured. (a) Number of compounds according to elements, each bar is partitioned into two color segments, with red representing the number of superconductors (SC), while blue denote non-superconductors (NSC).; (b) Proportion of boron and carbon compounds (c) Histogram for energy above the convex hull in (eV/atom), (d) Distribution according to space group, (e) Crystal structure of MgB_2 . (f)-(m): Crystal structures of known superconductors. (f) NbC (10.03 K)[70], (g) Mo_2BC (7.5 K) [124], (h) MgCNi_3 (8 K)[154], (i) Mo_2GaC (3.9 K)[155], (j) SrC_6 (1.65 K)[156], (k) YC_2 (3.89K)[121], (l) YB_6 (7.2 K)[104], and (m) $\text{LaPt}_2\text{B}_2\text{C}$ (10 K)[82].

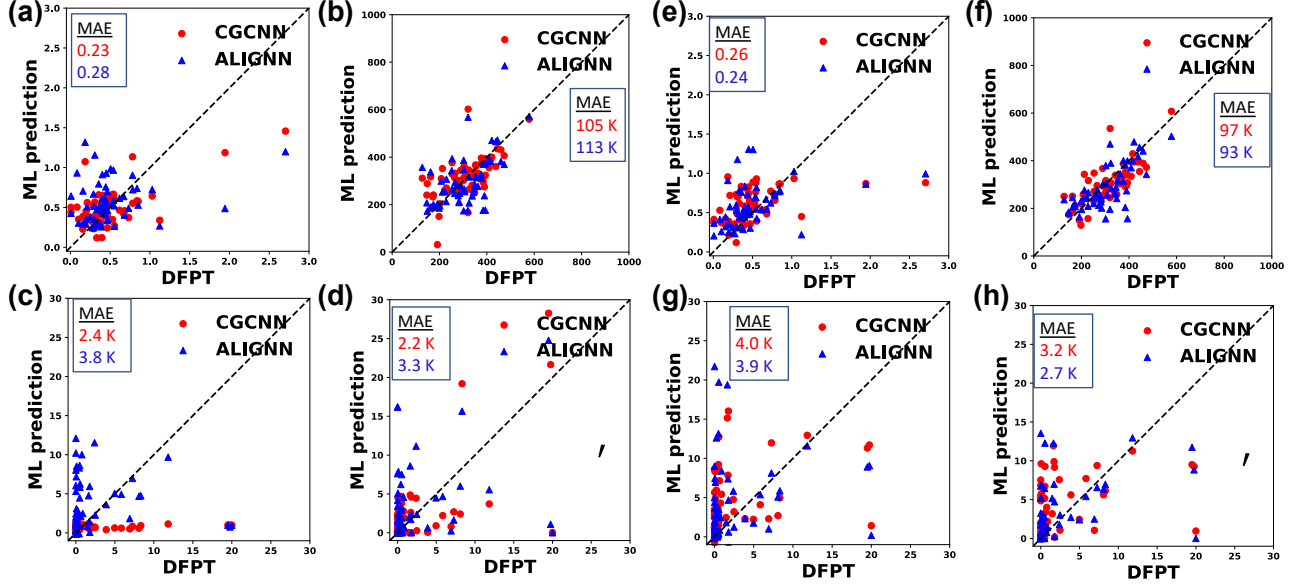


FIG. 3: Graph neural network-based regression models for dynamically stable compounds. Predicting λ , ω_{log} , T_c , and T'_c using CGCNN (red circles) and ALIGNN (blue upper triangle) models for the independent test set in comparison to the DFPT-calculated results in Run 1 (left panel, (a)-(d)) and Run 2 (right panel, (e)-(h)). Run 1 uses 250 training samples (45 space groups) and 58 test samples (27 space groups). Run 2 employs 323 training samples (54 space groups), with the test set unchanged. Similarly, Mean absolute error (MAE) are presented in inset. Red and blue arrows show the clustering pattern, discussed in the main text.

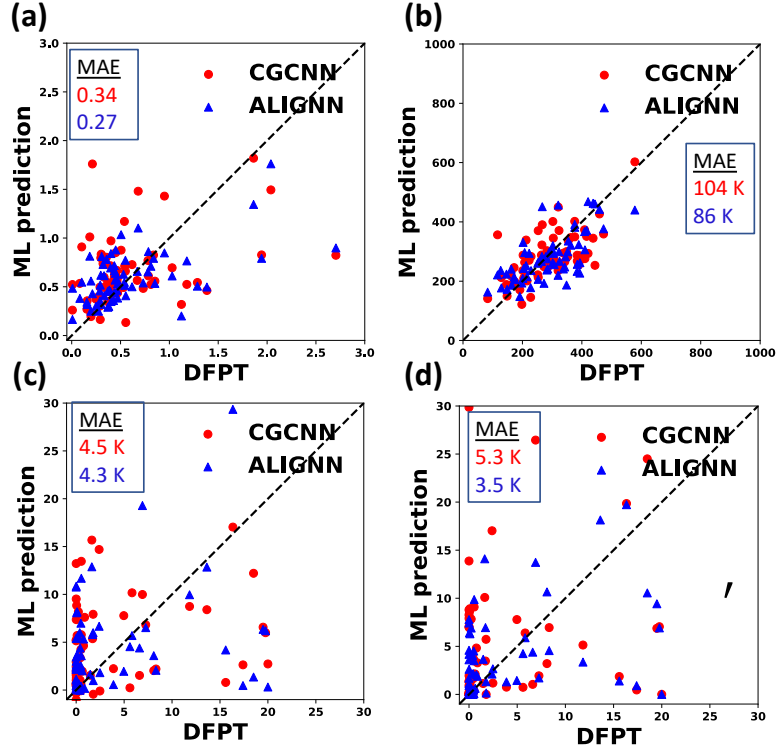


FIG. 4: Graph neural network-based regression models similar to Fig. 3, but including both stable and stabilized unstable compounds. Predicting λ , ω_{log} , T_c , and T'_c using CGCNN (red circles) and ALIGNNN (blue upper triangle) models for the independent test set including both stable and dynamically unstable cases in comparison to the DFPT-calculated results in Run3. Run 3 employs 351 training samples (56 space groups) and 66 test samples (27 space groups). MAEs are presented in inset.

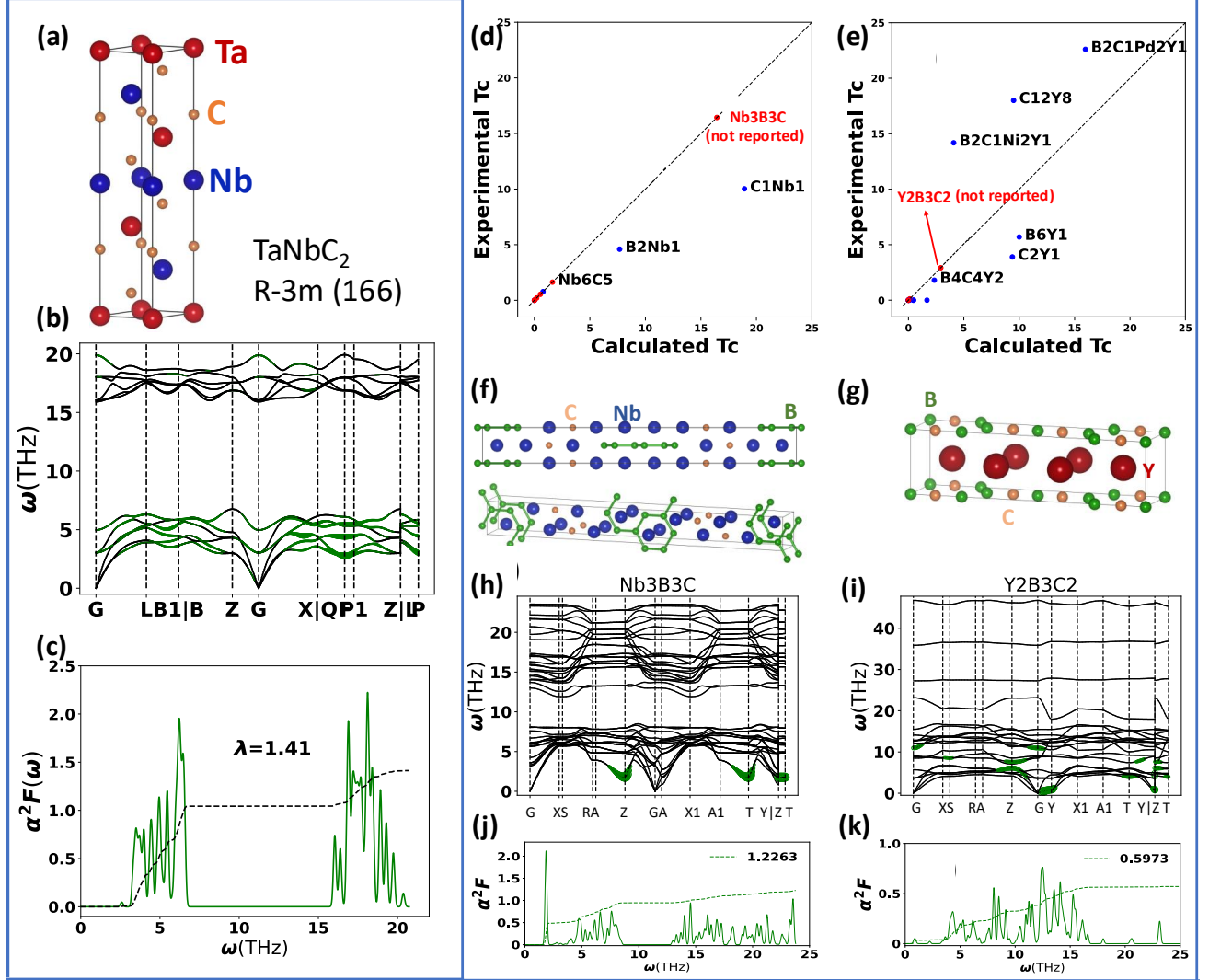


FIG. 5: DFPT calculated EPC properties of a few dynamically stable compounds. (a) Crystal structure, (b) phonon dispersion, and (c) Eliashberg isotropic spectral function of TaNbC_2 , respectively. (d)-(k) X-B-C compounds ($\text{X}=\text{Nb}, \text{Y}$): Comparison between DFPT computed T_c values with experiments for (d) Nb-B-C and (e) Y-B-C systems. Experimentally known results are represented by blue circle, while red circles are not reported ones shown along the $y=x$ dashed line as labeled. Crystal structures respectively for (f) $\text{Nb}_3\text{B}_3\text{C}$, and (g) $\text{Y}_2\text{B}_3\text{C}_2$. Atoms are highlighted by the colorized symbols. Phonon dispersion projected with mode-resolved λ (green open circles) for (h) $\text{Nb}_3\text{B}_3\text{C}$, and (i) $\text{Y}_2\text{B}_3\text{C}_2$ respectively. Eliashberg spectral functions for (j) $\text{Nb}_3\text{B}_3\text{C}$, and (k) $\text{Y}_2\text{B}_3\text{C}_2$ respectively.

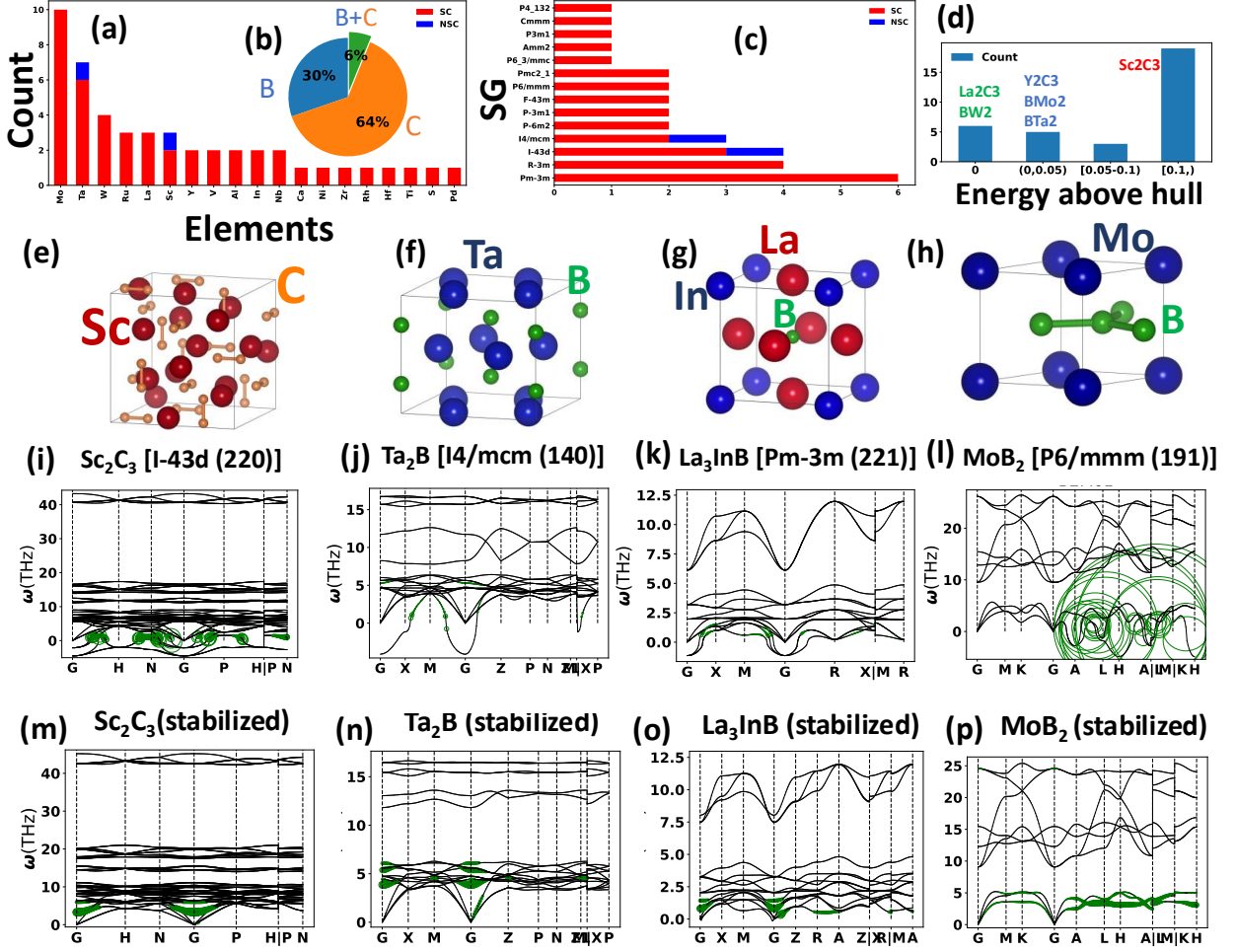


FIG. 6: Imaginary frequency modes with large EPC on the soft modes. Fig. (a) and (b) represent the count of different elements and allocation of B/C/B+C compounds in dynamically unstable systems respectively. Statistics according to spacegroup(c) and (d) energy above the convex hull. (e)-(h) Crystal structures of Sc₂C₃, Ta₂B, La₃InB, and MoB₂ are shown, respectively. (i)-(l) display the phonon dispersion plots of the dynamically unstable systems corresponding to Sc₂C₃, Ta₂B, La₃InB, and MoB₂. First 3 plots represent the instability of soft phonon modes at Γ -point, while the last one corresponds to the instability outside of Γ . (m)-(p): EPC results for compounds with stabilized imaginary phonon modes. EPC projected (highlighted by green circles) phonon band dispersions for Sc₂C₃ (P-30), Ta₂B (D), La₃InB (D), and MoB₂ (S-0.1) respectively.

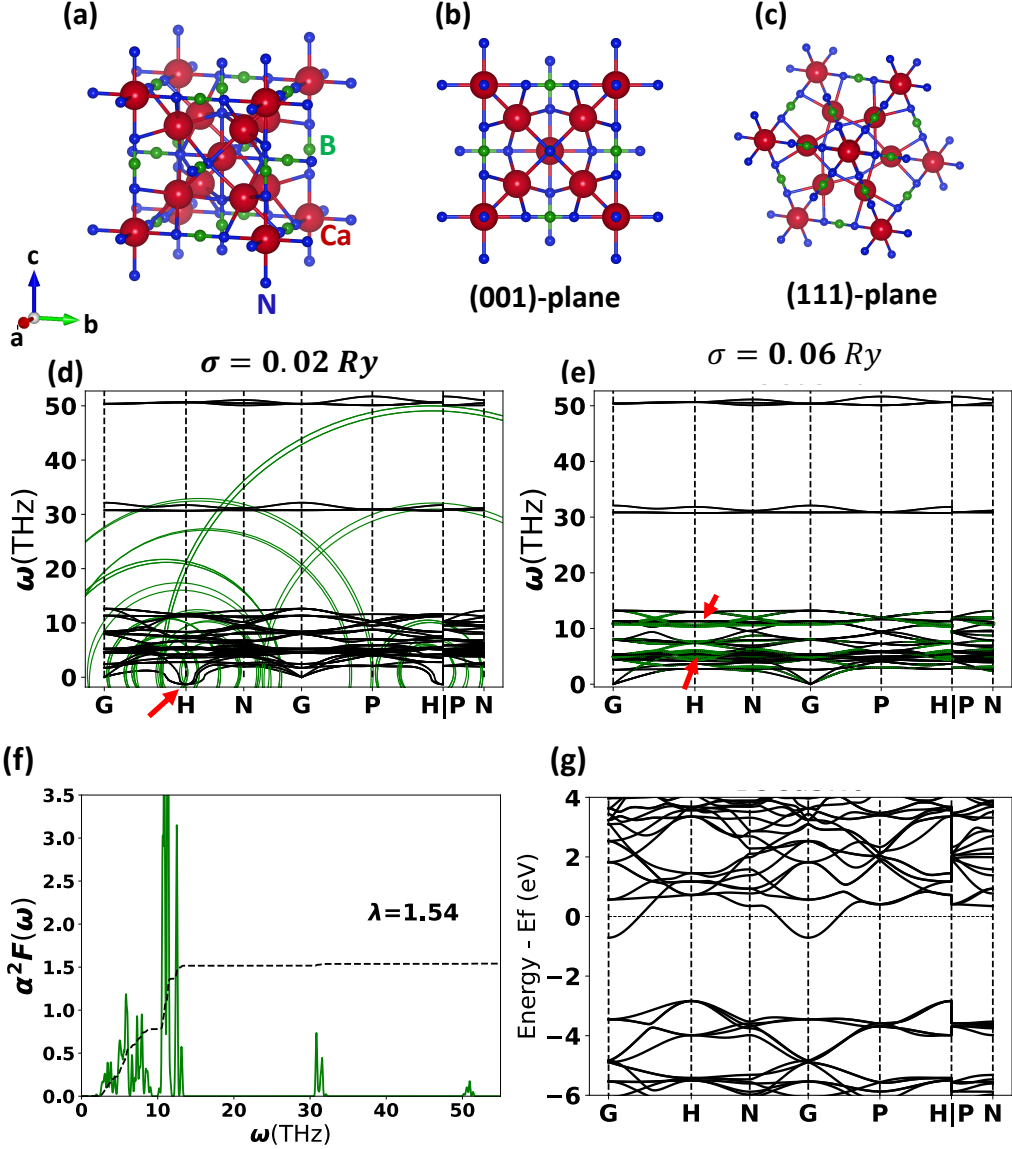


FIG. 7: Structures and EPC properties of $\text{Ca}_5\text{B}_3\text{N}_6$. (a)-(c): Crystal structures of $\text{Ca}_5\text{B}_3\text{N}_6$, viewed from different directions (d)-(e): EPC results for compounds with stabilized imaginary phonon modes for $\text{Ca}_5\text{B}_3\text{N}_6$. (d): EPC projected (highlighted by green circles) phonon band dispersions for dynamically unstable systems represented by small well at H-point (shown by red arrow), (e): Similar results for systems, stabilized with large electronic smearing of 0.06 Ry. (f) Eliashberg spectral function (g) Electronic band structure

Supplementary Materials for “Machine-learning Guided Search for Phonon-mediated Superconductivity in Boron and Carbon Compounds”

XI Statistics for compounds with unknown T_c

In Fig. S1, we present the descriptions of 268 dynamically stable compounds for which the experimental T_c is not known. Figure S1 (a)-(c) illustrate the distribution of different elements in these systems, the allocation of B/C/B+C compounds, and the deviation of their formation energy (ΔE_h) from stable structures, respectively. Most unknown compounds are associated with transition metals (TM) such as Nb, Ta, Mo, V, Y, and others. Approximately 80% of the structures are close to the ground state convex hull with $\Delta E_h \leq 0.05$ eV/atom, while the remaining 20% have ΔE_h greater than 0.05 eV/atom. Panel S1(d) showcases the distributions of these compounds based on their space groups. In Fig. S1(a) and (d), each bar is partitioned into segments, with the segments colored in red representing the number of SC, while the segments in blue denote the NSC. The overall description is similar to that of known compounds, as shown in Fig. 2 of the main text.

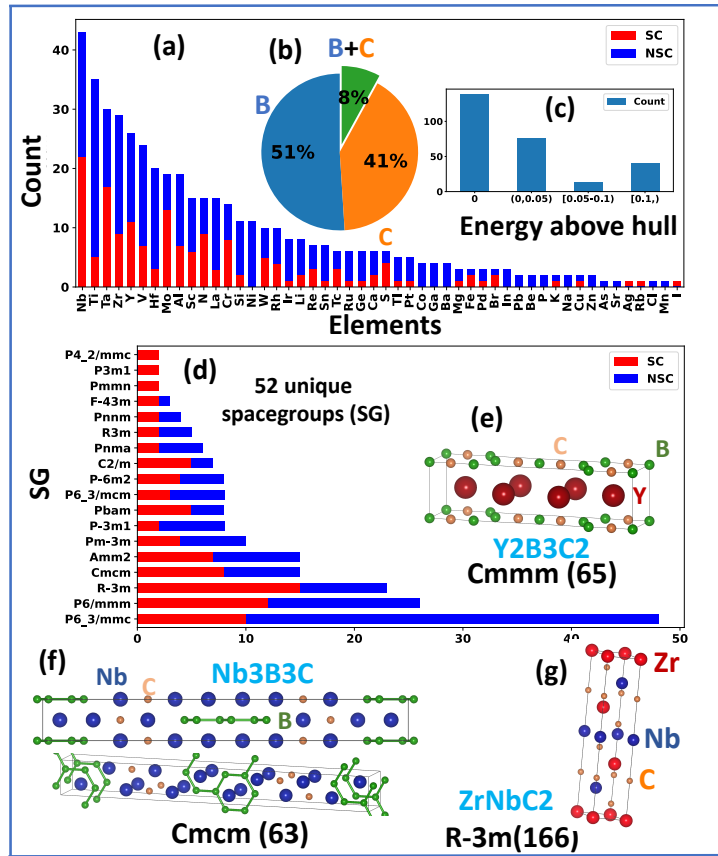


FIG. S1: Statistical description of dynamically stable materials, whose (non-) superconductivity hasn't been experimentally measured. Each bar is partitioned into segments, with the segments colored in "red" representing the number of superconductors (SC), while segments in "blue" denote nonsuperconductors (NSC).; (a) Number of compounds according to elements, (b) Proportion of boron and carbon compounds (c) Statistics in terms of energy above the convex hull, (d) Distribution according to spacegroups, (e)-(g): Crystal structures of some potential superconductors with their respective spacegroups.

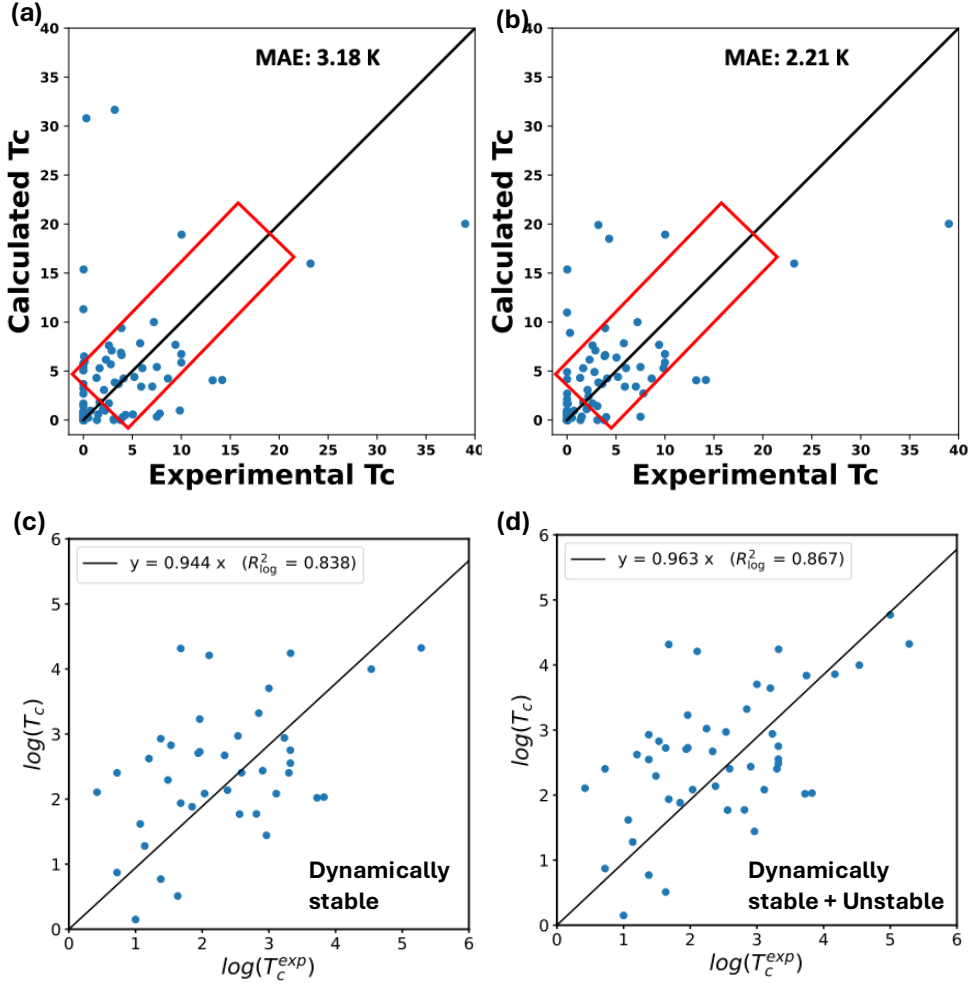


FIG. S2: Comparison of Predicted and Experimental Critical Temperatures Under k-Grid Refinement and Dataset Expansion. (a) Comparing calculated and experimental critical temperature obtained from efficient calculations; Some largely deviated results are not enclosed within red rectangular box. (b) Same plot with improved results with denser \mathbf{k} - grids for compounds with $A > A_{MgB_2}$. Red rectangular box on the right plot, enclosed more data points along the $y = x$ axis (black solid line), compared to plot on the left. (c) Predicted $\log(T_c)$ vs. measured $\log(T_c^{exp})$ for dynamically stable superconductors. (d) Same comparison after incorporating additional data obtained by stabilizing dynamically unstable compounds. The inclusion of these superconductors improves the coefficient of determination R^2_{\log} score from 0.838 to 0.867.

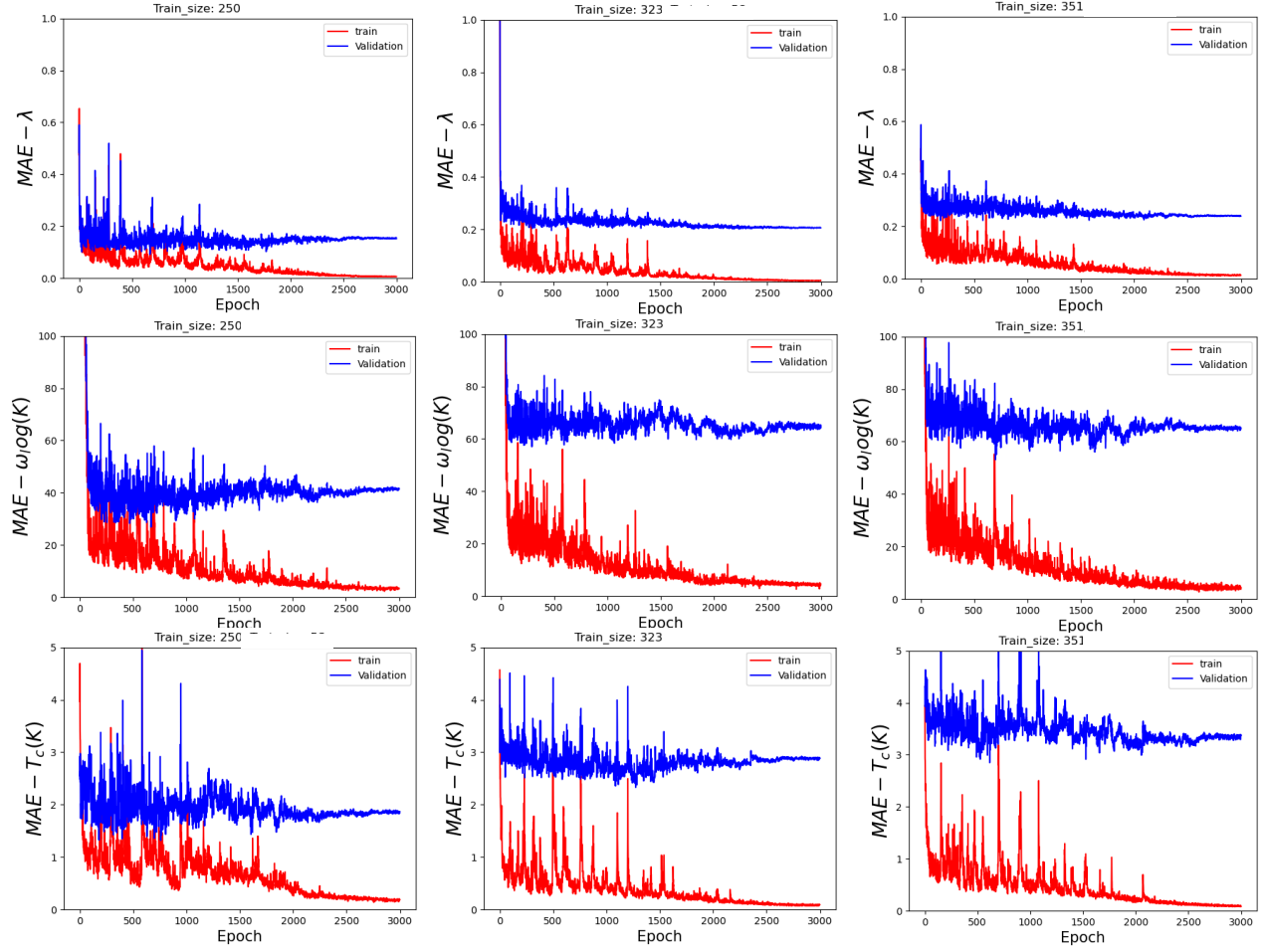


FIG. S3: Learning curves for various training and validation during the ALIGNN model training process.

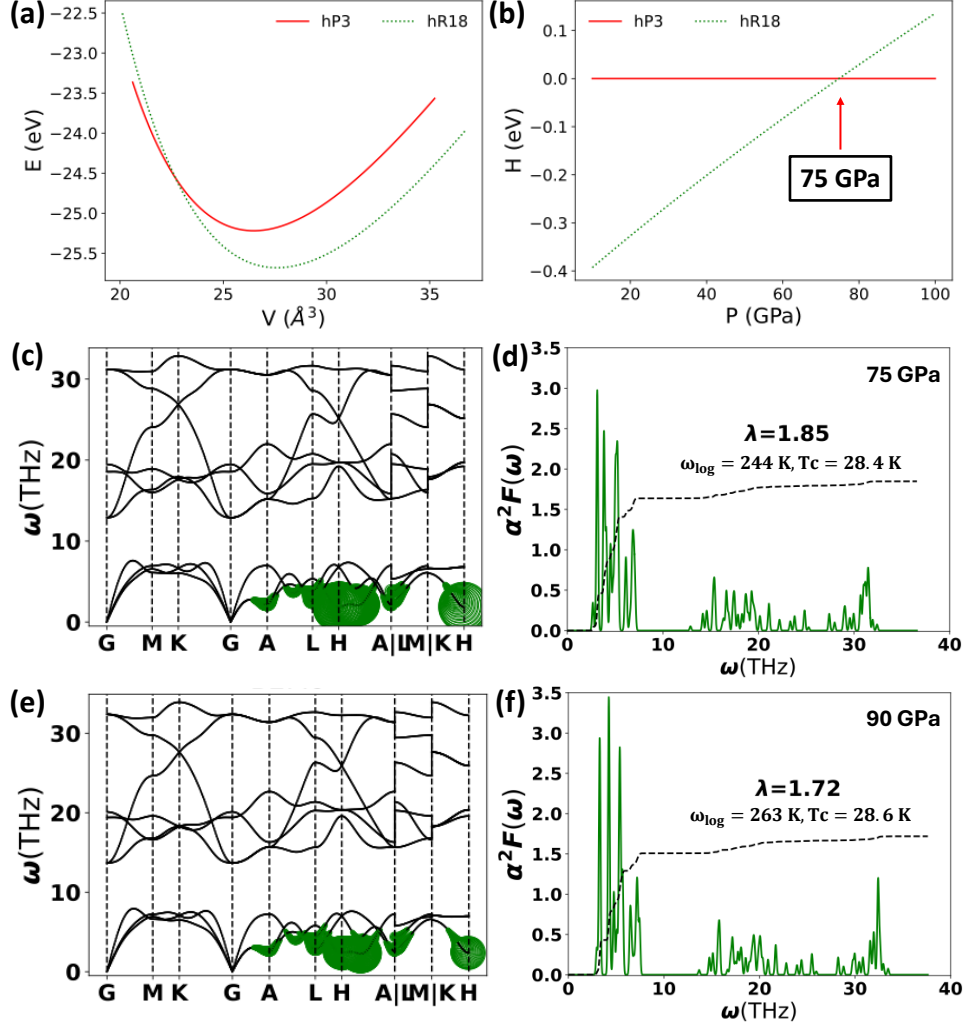


FIG. S4: Pressure-induced stabilization of phonons in MoB₂ and electron-phonon coupling (EPC) calculations. (a) Energy (E) versus volume (V) equation of state for the two phases of MoB₂: the high-pressure hP3 (P6/mmm) phase and the ambient pressure hR18 (R-3m) phase. (b) Enthalpy (H = E + PV) as a function of pressure (P, GPa) for two phases referenced to the hP3 phase. The crossover between the two phases occurs near 75 GPa (indicated by the arrow). (c) Phonon dispersion of hP3 MoB₂ at 75 GPa showing stabilization with EPC strength projected in green shading and (d) the corresponding Eliashberg spectral function. (e), (f) Same as (c), (d), but at 90 GPa.

TABLE S1: Mean Absolute Errors (MAEs) for the 10% test set in each training iteration with different sizes running for 3000 epochs.

Training size	CGCNN				ALIGNNN			
	λ	ω_{log} (k)	T _c (K)	T' _c (K)	λ	ω_{log} (K)	T _c (K)	T' _c (K)
250 (Run1)	0.15	72	1.8	1.3	0.15	56	1.7	2.2
323 (Run2)	0.27	85	6.4	5.5	0.16	83	3.0	3.3
351 (Run3)	0.31	70	3.9	6.5	0.24	60	3.0	4.4

TABLE S2: The best validation MAEs and their corresponding epochs during the training process are reported. CGCNN-250 represents the CGCNN model trained with 250 compounds and so on. Additionally, the coefficient of determination (R^2 -score) is also provided for a linear-fit $Y^{ML} = \text{slope} \times Y^{DFPT}, Y = (\lambda, \omega_{log}, T_c)$. A test set of 58 compounds is used for the model trained with 250 and 323 compounds, while 66 compounds are used for the model trained with 351 compounds. The R^2 -score with higher values close to 1 indicating better accuracy, while a score of 0 suggests no better performance than predicting the mean.

Model	EPC	Epoch	Best MAE	R^2 -score
CGCNN-250	λ	48	0.145	0.75
CGCNN-250	ω_{log}	60	49	0.45
CGCNN-250	T_c	13	2.80	0.56
CGCNN-323	λ	1190	0.203	0.66
CGCNN-323	ω_{log}	590	57	0.5
CGCNN-323	T_c	736	2.73	0.31
CGCNN-351	λ	64	0.204	0.62
CGCNN-351	ω_{log}	62	51	0.51
CGCNN-351	T_c	46	3.34	0.263
ALIGNN-250	λ	671	0.09	0.58
ALIGNN-250	ω_{log}	672	27	0.47
ALIGNN-250	T_c	760	1.32	0.23
ALIGNN-323	λ	483	0.196	0.64
ALIGNN-323	ω_{log}	293	57	0.63
ALIGNN-323	T_c	1275	2.33	0.32
ALIGNN-351	λ	186	0.22	0.72
ALIGNN-351	ω_{log}	701	53	0.77
ALIGNN-351	T_c	617	2.85	0.38

TABLE S3: MAE calculated separately for nonsuperconductors and superconductors. The test set of 58 includes 40 nonsuperconductors and 18 superconductors, while the test set of 66 consists of 41 nonsuperconductors and 25 superconductors, among which 7 are stabilized superconductors.

Training/test size	Property	Tc <= 1		Tc > 1	
		CGCNN	ALIGNN	CGCNN	ALIGNN
323/58	λ	0.28	0.21	0.20	0.32
	ω_{log}	56	54	188	111
	T_c	3.60	1.98	2.23	4.30
351/66	λ	0.39	0.20	0.27	0.39
	ω_{log}	125	99	69	63
	T_c	4.67	1.97	6.23	5.95

XII Classification models

In addition to regression, we also employ machine learning models for binary classification of materials into two categories: SC or NSC. We utilized the similar settings (batch, epochs, etc in config.json) as that of regression model training. Instead of finding a threshold T_c that maximizes the accuracy metrics, we simply perform the classification ML for a fix threshold T_c (0.5, 1.0, 2.0 K) and assess the model performance. The accuracy metrics used in our evaluation are presented in Table S4, and they are defined as follows:

$$\text{Accuracy} = \frac{T_P + T_N}{N} \quad (3)$$

$$\text{Precision} = \frac{T_P}{T_P + F_P} \quad (4)$$

$$\text{Recall} = \frac{T_P}{T_P + F_N} \quad (5)$$

$$\text{F1-score} = \frac{2(\text{Precision} \times \text{Recall})}{\text{precision} + \text{Recall}} \quad (6)$$

Accuracy, Precision, Recall, and F1-score are performance metrics that evaluate different aspects of a classifier's effectiveness. Accuracy measures the overall correctness of the classifier's predictions. Precision quantifies the correctness of positive predictions, while Recall (sensitivity) assesses the successful identification of positive instances. The F1-score is the harmonic mean of Precision and Recall, providing a balance between the two. T_P , T_N , F_P , and F_N represent true positive (correctly identifying true superconductors), true negative (correctly identifying true nonsuperconductors), false positive (misidentifying nonsuperconductors as superconductors), and false negative (misidentifying superconductors as nonsuperconductors), respectively. The accuracy metrics of classification models for both Run 1 and Run 3 are displayed in Table. S4. Across all these metrics, the overall accuracies are reasonable, indicating a useful classification model despite the small dataset. By employing a classification threshold of $T_c = 1$ K, both ML models exhibit comparable performance. Notably, one can observe the enhanced accuracy of Run 3 in contrast to Run 1. This improvement might be attributed to the expanded training dataset size and the balanced representation of both SC and NSC instances after adding stabilized high T_c results. The ML model, when using a T_c threshold of 1 K, achieves an overall accuracy ranging from 60% to 70%, precision ranging from 70% to 90%, and an F1-score ranging between 50% and 60%. The ML models demonstrate lower recall values, ranging from 50% to 55%. Considering the data imbalance between the number of SC instances (approximately 40%) and NSC instances (approximately 60%), these recall values are reasonable.

TABLE S4: Classification accuracy: Results from ML model are presented in the form CGCNN/ALIGNN.

$T_c^{Threshold}$ (K)	Run 1				Run 3			
	Accuracy	Precision	Recall	F1-score	Accuracy	Precision	Recall	F1-score
0.5	0.67/0.59	0.83/0.58	0.57/0.50	0.68/0.54	0.71/0.67	0.74/0.67	0.68/0.64	0.71/0.66
1.0	0.66/0.62	0.83/0.72	0.47/0.43	0.60/0.54	0.64/0.67	0.84/0.72	0.51/0.55	0.64/0.62
2.0	0.72/0.62	0.77/0.77	0.43/0.34	0.56/0.48	0.69/0.61	0.9/0.7	0.5/0.41	0.64/0.52

XIII Theory of superconductivity: Isotropic Approximation

We have adopted the DFPT calculation with isotropic Eliashberg approximation to compute SC properties, which provides a harmony between accuracy and efficiency. The critical temperature can be calculated using the Allen-Dynes formula [1],

$$T_c = \frac{\omega_{log}}{1.2} \exp \left[-\frac{1.04(1+\lambda)}{\lambda - \mu_c^*(1+0.62\lambda)} \right], \quad (7)$$

where, $\lambda = 2 \int_0^\infty \frac{d\omega}{\omega} \alpha^2 F(\omega)$ is the EPC strength constant, $\omega_{log} = \exp \left[\frac{2}{\lambda} \int_0^\infty \frac{d\omega}{\omega} \alpha^2 F(\omega) \log \omega \right]$, $\alpha^2 F(\omega)$ is frequency (ω) resolved Eliashberg spectral function, and μ_c^* is the Coulomb potential. The spectral function $\alpha^2 F(\omega)$ is defined as,

$$\alpha^2 F(\omega) = \frac{1}{2} \sum_{\nu} \int_{BZ} \frac{d\mathbf{q}}{\Omega_{BZ}} \omega_{\mathbf{q}\nu} \lambda_{\mathbf{q}\nu} \delta(\omega - \omega_{\mathbf{q}\nu}). \quad (8)$$

Here, Ω_{BZ} is the volume over the Brillouin zone $\int_{BZ} \frac{d\mathbf{q}}{\Omega_{BZ}} \rightarrow \frac{1}{N_{\mathbf{q}}} \sum_{\mathbf{q}}$, $\omega_{\mathbf{q}\nu}$ is the mode (ν) resolved phonon frequency, and $\lambda_{\mathbf{q}\nu}$ is the mode resolved EPC strength constant,

$$\lambda_{\mathbf{q}\nu} = \frac{1}{N(\epsilon_F) \omega_{\mathbf{q}\nu}} \sum_{mn} \int_{BZ} \frac{d\mathbf{k}}{\Omega_{BZ}} |g_{mn,\nu}(\mathbf{k}, \mathbf{q})|^2 \delta(\epsilon_{n\mathbf{k}} - \epsilon_F) \delta(\epsilon_{m\mathbf{k}+\mathbf{q}} - \epsilon_F). \quad (9)$$

$N(\epsilon_F)$ is the density of states at the Fermi level ϵ_F , and $g_{mn,\nu}(\mathbf{k}, \mathbf{q})$ is the EPC matrix element which quantifies the scattering process between Kohn-Sham states $m\mathbf{k} + \mathbf{q}$ and $n\mathbf{k}$. In Ref. [2], an effective approach to approximate double delta integration is explored, specifically tailored for situations where it is permissible to disregard the dependence on the momentum vector (\mathbf{q}). This method finds utility in scenarios such as the study of extensive molecular systems like alkali fullerides, where momentum dependence can be safely overlooked. The net EPC strength constant is computed as

$$\lambda = \sum_{q\nu} \lambda_{q\nu} \quad (10)$$

For computational feasibility, these Dirac deltas can be approximated by Gaussian functions with a broadening parameter σ [3], and EPC strength is given by Eqs.9 and 10 can be redefined as

$$\lambda \approx \frac{1}{N(\epsilon_F)N_{\mathbf{q}}N_{\mathbf{k}}} \sum_{nm} \sum_{\mathbf{q}} \sum_{\mathbf{k}} \frac{|g_{mn,\nu}(\mathbf{k}, \mathbf{q})|^2}{\omega_{q\nu}} \frac{1}{2\pi\sigma^2} \exp \left[-\frac{(\epsilon_{n\mathbf{k}} - \epsilon_F)^2 + (\epsilon_{m\mathbf{k}+\mathbf{q}} - \epsilon_F)^2}{\sigma^2} \right]. \quad (11)$$

Here, $N_{\mathbf{q}}$ and $N_{\mathbf{k}}$ respectively are the total number of \mathbf{q} and \mathbf{k} grid points, and σ is the smearing used to broaden states at the Fermi-level ϵ_F . With infinitely large \mathbf{k} - grids, and $\sigma \rightarrow 0$, the double summation changes back to double delta integration. Moreover, λ can also be obtained from frequency ω resolved Eliashberg spectral function as [4]

$$\lambda = 2 \int \frac{d\omega \alpha^2 F(\omega)}{\omega} = \frac{N(\epsilon_F) \langle g^2 \rangle}{M \langle \omega^2 \rangle}, \quad (12)$$

where, $\langle \omega^2 \rangle$ average of the square of the phonon frequency $\left(\frac{\int d\omega \omega \alpha^2 F(\omega)}{\int \frac{d\omega}{\omega} \alpha^2 F(\omega)} \right)$, $\langle g^2 \rangle$ is average over the Fermi surface of the square of electronic phonon coupling matrix element [4].

XIV Convergence tests for MgB₂ and AlB₂

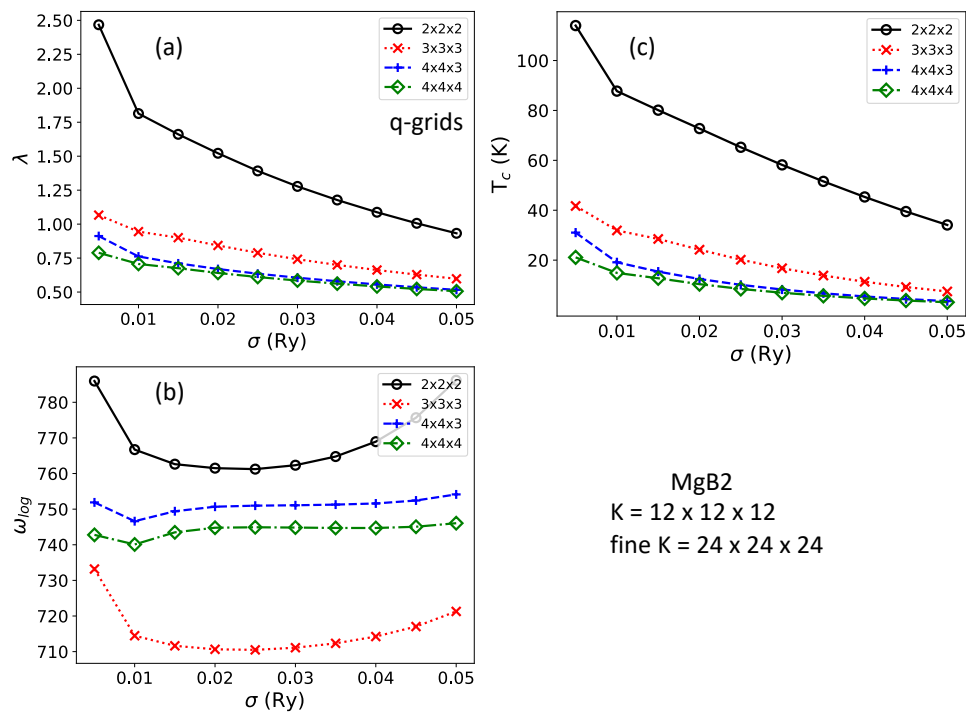
The ground-state total energy and phonon frequencies at Γ -point are well converged for MgB₂ with \mathbf{k} -grids of $8 \times 8 \times 6$, compared to the dense grid of $24 \times 24 \times 24$. K-mesh grid in materials project database for MgB₂ is $8 \times 8 \times 7$. Since the superconducting properties of MgB₂ with \mathbf{k} -grid of $8 \times 8 \times 8$ doesn't follow the trend of converged result of denser k-mesh with $\sigma \rightarrow 0$, we chose $8 \times 8 \times 6$ so that we can use sufficient \mathbf{q} -grids of $4 \times 4 \times 3$ instead of using $9 \times 9 \times 9$ \mathbf{k} -grid and $3 \times 3 \times 3$ \mathbf{q} -grid. We utilized $8 \times 8 \times 6$ \mathbf{k} -grid and its multiple to compute the decay parameter. In this work, we are taking $\lambda = 0.75$ obtained from solving anisotropic Migdal-Eliashberg equation using $\mu^* = 0.16$ as a reference [Comput. Phys. Commun. **209**, 116 (2016)]. One can obtain this converged λ with denser \mathbf{k} - and \mathbf{q} - grids and $\sigma \rightarrow 0$, as shown in Figs. S5 – S7. At last, we check whether the result is transferable to systems with larger unit cell where essentially smaller \mathbf{k} -grids provide converged ground-state properties and \mathbf{q} -grid, taken half of \mathbf{k} -grid, sometime shrinks only to include the Γ -point. To do that, we performed EPC calculations with $2 \times 2 \times 2$ supercell of MgB₂ which has 24 atoms per cell, and present the results in Fig. S8 and S9. Results confirm that \mathbf{q} -grid as half as that of the \mathbf{k} -grid can provide converged results even for larger systems. Instead of increasing coarse \mathbf{k} - and \mathbf{q} - grids, one can also utilize extremely large \mathbf{k} - grid for interpolating EPC matrix element to achieve convergence, as shown in Figs. S7 and S10 respectively for MgB₂ and AlB₂. However, it also increases computational complexity for larger systems.

TABLE S5: Convergence of the ground-state total energy with respect to K-point mesh

K-mesh	Total Energy (eV/atom)
$6 \times 6 \times 4$	-615.178
$8 \times 8 \times 6$	-615.179
$8 \times 8 \times 8$	-615.180
$9 \times 9 \times 9$	-615.180
$12 \times 12 \times 12$	-615.180
$16 \times 16 \times 16$	-615.180
$24 \times 24 \times 24$	-615.180

TABLE S6: Convergence of phonon frequency (THz) at Γ -point with respect to K-point mesh

K-mesh	ω_1	ω_2	ω_3	ω_4	ω_5	ω_6	ω_7	ω_8	ω_9
$6 \times 6 \times 4$	-0.654	-0.654	0.343	10.18	10.18	12.07	20.96	24.38	24.38
8 \times 8 \times 6	-0.49	-0.49	0.48	10.11	10.11	12.11	16.45	16.45	20.75
8 \times 8 \times 8	-0.63	-0.63	0.28	10.1	10.1	12.11	17.43	17.43	20.8
9 \times 9 \times 9	-0.62	-0.62	-0.33	9.99	9.99	12.08	14.36	14.36	20.65
12 \times 12 \times 12	-0.64	-0.64	-0.23	10.06	10.06	12.12	17.13	17.13	20.69
16 \times 16 \times 16	-0.64	-0.64	-0.25	10.05	10.05	12.1	17.2	17.2	20.69
24 \times 24 \times 24	-0.64	-0.64	-0.22	10.05	10.05	12.1	16.99	16.99	20.71

FIG. S5: Convergence test for MgB₂ results with respect to \mathbf{q} -mesh. Unit of T_c and ω_{log} is Kelvin (K); As \mathbf{q} becomes denser, convergence can be achieved across the $\sigma \rightarrow 0$, with less exponential decay. Fine \mathbf{k} - grid is utilized for interpolation.

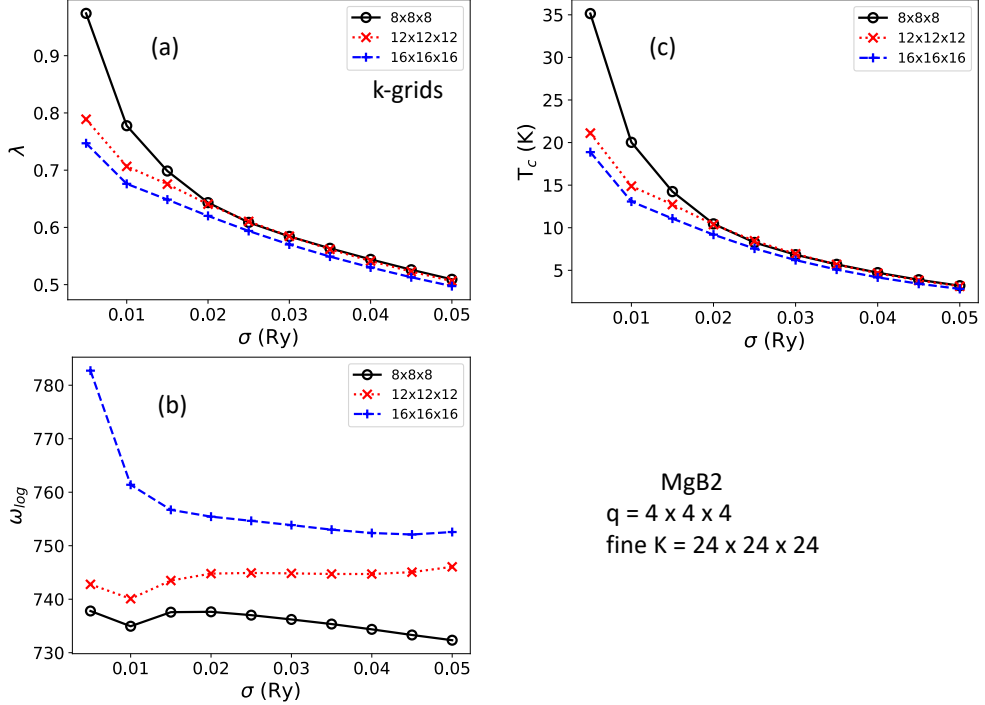


FIG. S6: Convergence test for MgB₂ results with respect to \mathbf{k} -mesh. Unit of T_c and ω_{log} is Kelvin (K); As \mathbf{k} becomes denser, convergence can be achieved across the $\sigma \rightarrow 0$, with less exponential decay. Fine \mathbf{k} - grid is utilized for interpolation.

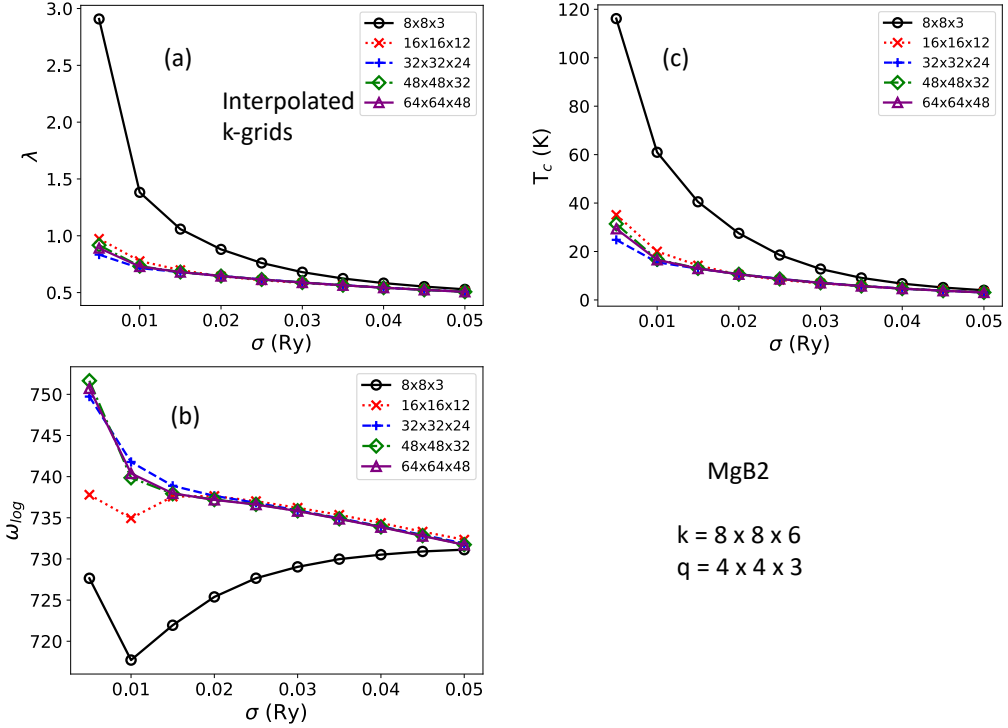


FIG. S7: Convergence test for MgB₂ results with respect to fine \mathbf{k} -mesh used for interpolation. Unit of T_c and ω_{log} is Kelvin (K); As fine \mathbf{k} becomes denser, convergence can be achieved across the $\sigma \rightarrow 0$, with less exponential decay.

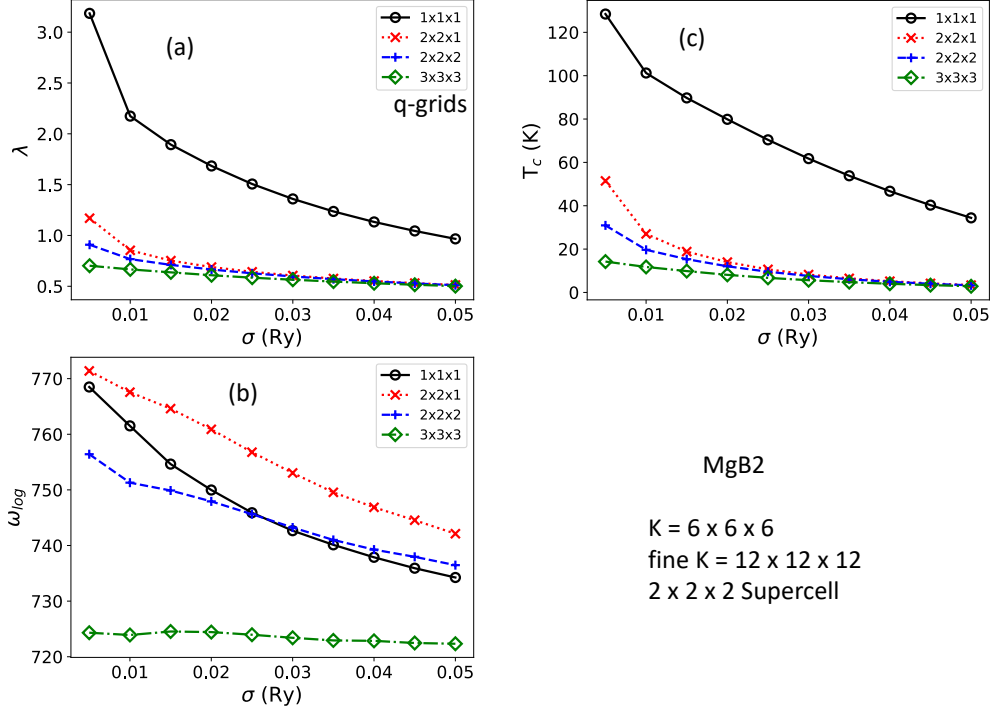


FIG. S8: Convergence test for $2 \times 2 \times 2$ supercell of MgB₂ results with respect to **q**-mesh. Unit of T_c and ω_{log} is Kelvin (K); As **q** becomes denser, convergence can be achieved across the $\sigma \rightarrow 0$, with less exponential decay. Fine **k**- grid is utilized for interpolation.

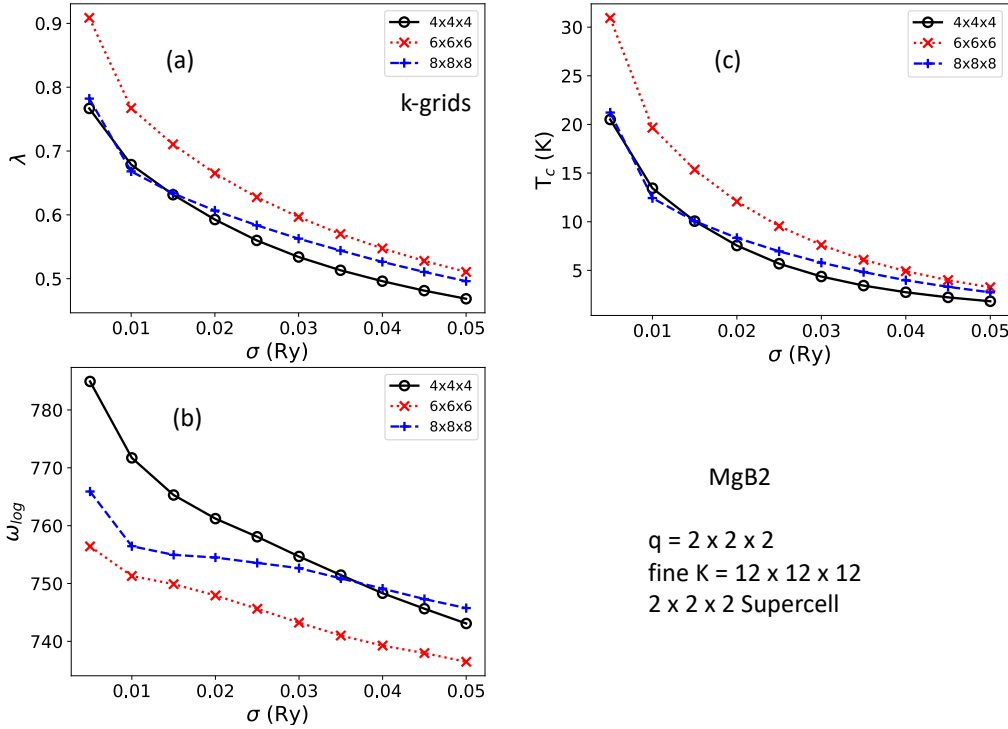


FIG. S9: Convergence test for $2 \times 2 \times 2$ supercell of MgB₂ results with respect to **k**-mesh. Unit of T_c and ω_{log} is Kelvin (K); As **k** becomes denser, convergence can be achieved across the $\sigma \rightarrow 0$, with less exponential decay. Fine **k**- grid is utilized for interpolation.

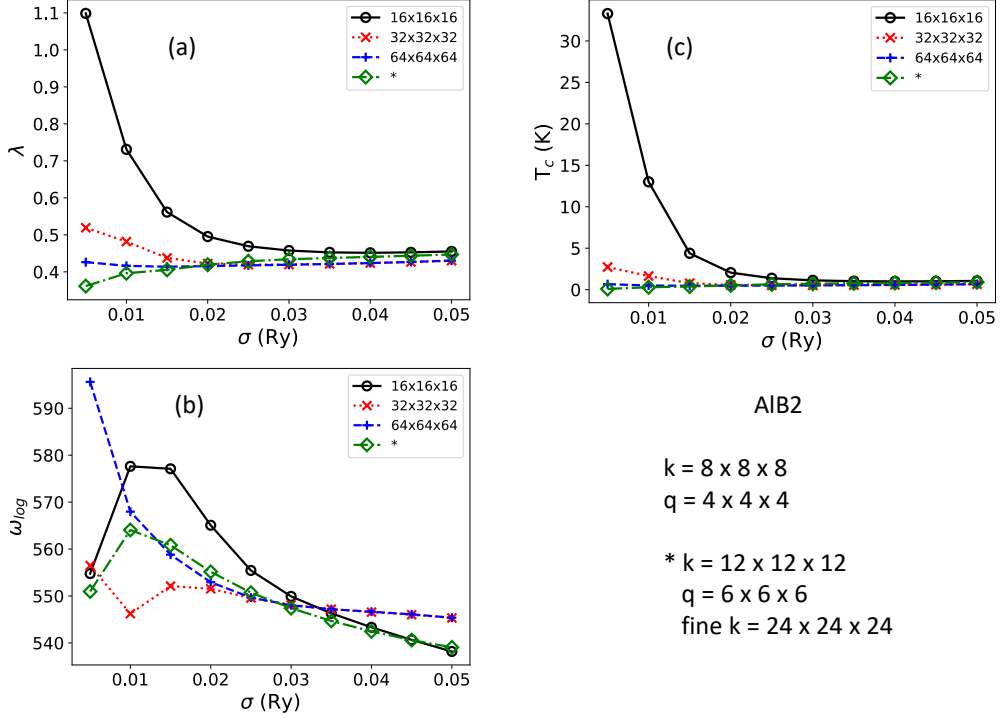


FIG. S10: Convergence test for AlB₂ results with respect to various **k**- and **q**-grids. Unit of T_c and ω_{log} is Kelvin (K); As grids becomes denser, convergence can be achieved across the $\sigma \rightarrow 0$, with less exponential decay. Separate results corresponding to **k**- and **q**- grids respectively of $12 \times 12 \times 12$ and $6 \times 6 \times 6$ is represented by “star (*)” symbol.

XV Convergence ansatz

Estimation of SC properties requires the computation of double-delta integration, which also defines the nesting function, around the Fermi level E_F over the entire Brillouin zone [Eq. 3]. However, it has a slow convergence with respect to **k**- and **q**- grids. In principle, it requires infinitely dense grids, which makes the computation exorbitantly expensive. Therefore, Gaussian broadening technique [Eq. 5] is employed to compute λ with finite **k**-mesh. To compute T_c, we employed the DFPT calculation with the isotropic Eliashberg approximation. We used a coarse **k**-grid obtained from the MP database, which provides reasonably accurate ground-state properties. The **q**-grid was set to half the size of the **k**-grid, and a broadening parameter (σ) of 0.01 Ry was utilized with the coarse MP grid, which accurately captures a converged electron-phonon coupling constant (λ) of MgB₂ computed using the anisotropic Migdal-Eliashberg equations [5]. However, in practice, $|g_{mn,\nu}(\mathbf{k}, \mathbf{q})|^2$ is computed for a reasonable coarse **k**- and **q**- grids and interpolated the matrix elements to fine **k**- for any **q**-point, from $32 \times 32 \times 32$ to as high as $60 \times 60 \times 60$, to achieve numerical convergence, as implemented in Quantum Espresso (QE) code[3]. Furthermore, an efficient interpolation scheme utilizing both dense **k**- as well as **q**-grids has been implemented in EPW package that uses wannier orbitals [5]. However, employing extremely fine grids for interpolation can increase the computational complexity, which is not suitable for highthroughput calculations. Therefore, we have restricted ourselves for choosing fine **k**-grid only twice of corresponding coarse grid for highthroughput calculations.

Our investigation revealed that a reasonable number of calculations did not converge, leading to inaccurate predictions, while utilizing a coarse **k**-grid from MP database and fine grid for interpolation only twice that of the **k**-grid [Table S7]. For example, AlB₂ was predicted to be a superconductor ($T_c \sim 11$ K) with the coarse grid [**k**-grid: $8 \times 8 \times 8$, **q**-grid: $4 \times 4 \times 4$, fine-**k**-mesh: $16 \times 16 \times 16$] from MP database, whereas a denser grid twice the size of the coarse grid corrected this inaccuracy and predicted AlB₂ to be a nonsuperconductor, consistent with experimental observations [Fig. S7]. To identify such cases of convergence failure, we examined the variation of T_c with respect to σ and developed a simple ansatz based on the converged results of MgB₂, as depicted in Fig. S13. The ansatz involves extracting T_c with a fixed broadening value (as in the case of MgB₂) and estimating the decay parameter (A) in the exponential variation of T_c with σ as $T_c \sim \exp(-A\sigma^{1/3} + B)$. Unconverged results exhibit larger values of A, which

decrease with a denser \mathbf{k} -mesh.

The detail theory of EPC calculations within DFPT formalism is presented in the section “Theory of superconductivity: isotropic approximation”. The variation of density of states at the Fermi level ($N(\epsilon_F)$) with respect to smearing σ , depends on Gaussian,

$$G(\Delta, \sigma) = \frac{1}{\sigma^2} \exp \left[-\frac{(\epsilon_{n\mathbf{k}} - \epsilon_F)^2 + (\epsilon_{m\mathbf{k}+\mathbf{q}} - \epsilon_F)^2}{\sigma^2} \right] \sim \frac{1}{\sigma^2} \exp \left[-\frac{\Delta^2}{\sigma^2} \right] \quad (13)$$

with $\Delta^2 \sim (\epsilon_{n\mathbf{k}} - \epsilon_F)^2 + (\epsilon_{m\mathbf{k}+\mathbf{q}} - \epsilon_F)^2$ also depends on σ . Despite of dependency of λ on EPC matrix ($\langle g^2 \rangle$) and phonon frequency ($\langle \omega^2 \rangle$) terms, the variation in λ is largely guided by the variation in $N(\epsilon_F)$ or the Gaussian term G . Fig. S11(a) shows the variation of G with respect to smearing σ for different values of Δ , assuming Δ independent of σ . The effect of σ on G dictates the variation of λ and hence T_c , with Δ depends on the materials as well as on size of the grid to compute double delta integration. A larger Δ represents more states contributing towards the double delta summation within space around the Fermi-level spanned by σ . In other word, Δ will increase with σ if the density of states has local maximum close to the Fermi-level, and the variation of EPC properties will be similar to the Gaussian plots corresponding to $\Delta \geq 0.05$. For Niobium, the variation of EPC properties with respect to σ follows similar to blue-dashed curve corresponding to $\Delta = 0.01$ [3], whereas for MgB_2 , the variation follows the Gaussian corresponding to $\Delta < 0.01$. For $\sigma \rightarrow 0$ and $\Delta \rightarrow 0$, if $\frac{\Delta}{\sigma} \leq 1$ the Gaussian function recovers the delta function, while for $\frac{\Delta}{\sigma} \geq 1$ the Gaussian drops to zero similar to $\Delta \geq 0.01$ cases. Our primary focus is more on exponentially decaying cases.

The effect of smearing σ on ω_{log} is insignificant compared to $N(\epsilon_F)$ or λ [2]. According to the Bardeen–Cooper–Schrieffer (BCS) theory [6],

$$T_c \sim \Theta_D \exp(-1/\lambda) \sim \Theta_D \exp\left(-\frac{1}{N(\epsilon_F)U}\right) \quad (14)$$

where Θ_D is the Debye cutoff energy and U is electron-phonon coupling potential. One can establish the relation between λ or T_c on σ as $\lambda \sim 1/\sigma^\alpha$ and $T_c \sim \Theta_D \exp(-1/\lambda) = \exp(-A\sigma^\alpha + B)$ with $\Theta_D \sim \exp(B) \times \text{constant}$. Here parameter α is a constant with a positive value if T_c decreases with increasing σ and becomes negative otherwise. Here A and B are constants to be determined with A denoting the coefficient of exponential increase (for negative A) or decrease (for positive A) of T_c with respect to σ . To determine the value of these constants, we perform linear-fit of $\log T_c$ vs σ^α for different \mathbf{k} -grids for MgB_2 , which is frequently studied both theoretically as well as experimentally and often challenging to obtain the converged SC properties [7–9]. Furthermore, one can capture the behavior of T_c vs σ for a wide range of T_c using MgB_2 , as shown in Fig. S11(b). We utilize a smaller \mathbf{k} -mesh of $6 \times 6 \times 4$ and a slightly larger \mathbf{k}' -grid of $8 \times 8 \times 6$ for comparison [Fig. S11(b) and (c)].

Fig. S11 (b) represents the variation of T_c with respect to σ , while Fig. S11 (c) presents $\log T_c$ vs σ^α plot. It exhibits nearly linear behavior up to $\sigma = 0.05$ Ry, i.e. $\sigma^{1/3} = 0.37$, after which it deviates from linearity. The linear-fit has optimal coefficient of determination score (R^2 -score) for $\alpha < 0.5$ on $\log T_c$ vs σ^α data for \mathbf{k} (charge density and EPC)- \mathbf{q} (Phonon and EPC)- $2\mathbf{k}$ (interpolating EPC matrix) grids (Fig. S11 (c)) [Table within the Fig. S11(c)]. Therefore, we chose $\alpha = 1/3$ in this work with R^2 -score of 0.9987. Besides different choice of α leads to different values of A and B , it doesn't have a significant role. For coarse grid, the T_c has a larger dependency on σ and shows larger exponential decay, compared to more converged calculations on denser grids. The exponential decay parameter “A” decreases from 19 to 10 with grids changing from coarse to dense one. This analysis suggests that $A_{\text{MgB}_2} = 12-13$ can be used as a cutoff for this work, the calculations can be considered un converged for $A > A_{\text{MgB}_2}$, while the calculations can be considered converged for $A < A_{\text{MgB}_2}$ for accurate predictions. Fig. S11(d) shows the convergence of the T_c with respect to \mathbf{q} -point mesh, keeping \mathbf{k} -grid fixed at $12 \times 12 \times 12$. A \mathbf{q} -point grid as half as that of the ground-state \mathbf{k} -point grid is sufficient to provide the converged results for MgB_2 . Fig. S11 (e) represents the spectral functions for various grids with $\mathbf{k} = 8 \times 8 \times 6$. Denser grid ($2\mathbf{k}$) slightly blue shifts the spectral function peaks at lower frequency range (15.5–16.5 THz), while peaks at higher frequency ranges (20–22.5 THz) remain unaffected. This results slight change in λ from 0.78 to 0.72 and T_c changing from 20 K to 15–16 K [Figs. S5–S7]. A λ of 0.78 agrees with previous theoretical value of ~ 0.75 from anisotropic Migdal–Eliashberg calculation using $\mu^* = 0.16$ [5], $\lambda = 0.71$ from fully anisotropic SCDFD [10], and $\lambda = 0.73$ from previous isotropic Eliashberg approximation [11] at slightly larger $\sigma = 0.015$ Ry. This indicates a \mathbf{k} -grid obtained from MP database with $\sigma = 0.01$ Ry already provide converged results in the case of MgB_2 . However, it is not always the case for other materials. Based on these results, parameters $\sigma = 0.01$ Ry with $\mu_c^* = 0.16$ seems to be reasonable choice for smearing with $8 \times 8 \times 6$ to $16 \times 16 \times 12$ \mathbf{k} -grids for MgB_2 , and for other systems for the sake of comparison. These parameters could also depend on pseudopotentials. In order to achieve converged results, it is necessary to use denser \mathbf{k} - and \mathbf{q} -grids. Subsequently, a double-delta integration should be performed, selecting the results that correspond to the limit of $\sigma \rightarrow 0$. Other details convergence tests of MgB_2 with respect to Brillouin-zone sampling are presented in Figs. S5–S10.

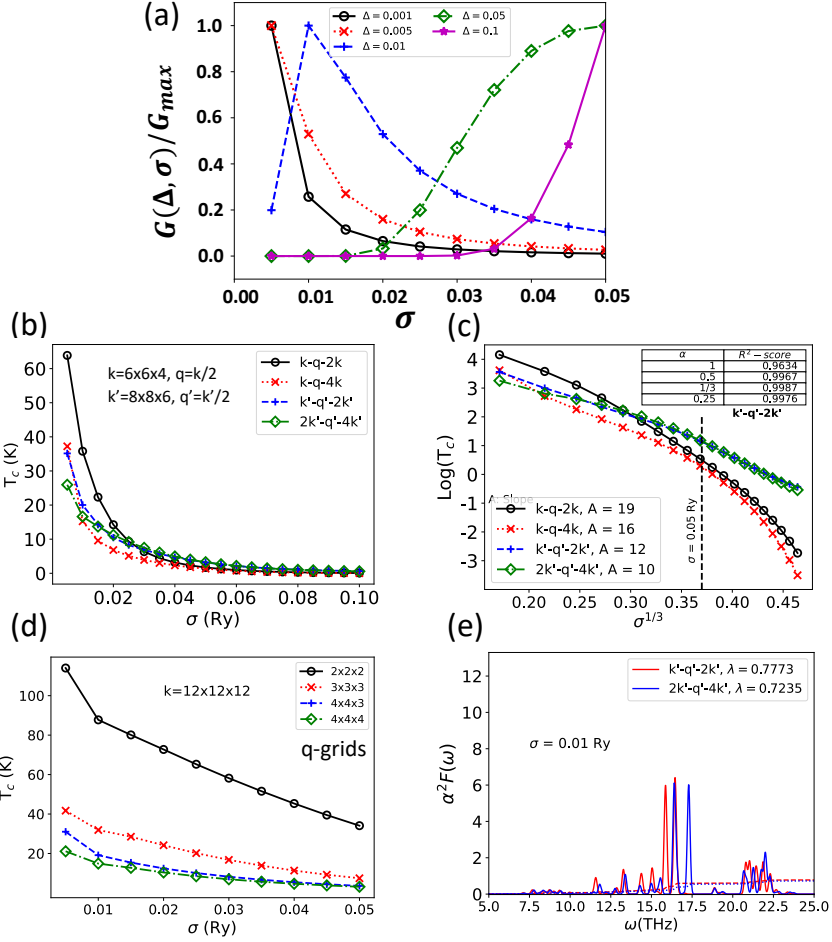


FIG. S11: Decay Constant Determination from Converged MgB₂ data. (a) Variation of $\frac{G(\Delta, \sigma)}{G_{max}}$ with respect to σ for different values of Δ ; G_{max} being the maximum value of Gaussian for corresponding Δ within the value of σ from 0.005 Ry to 0.05 Ry. (b) T_c vs σ for various k - grids for MgB₂. $k-q-2k$ represents k -mesh for self-consistent calculation for charge density and EPC, q -mesh for phonon and EPC, and $2k$ -mesh represents fine grid used for interpolating EPC matrix obtained from k and q -grids; k and k' respectively are $6 \times 6 \times 4$ and $8 \times 8 \times 6$. (c) $\log T_c$ vs $\sigma^{1/3}$ plot; Linear-fit is performed for data up to $\sigma = 0.05$ Rydberg (denoted by vertical dashed line), after which lines change slope; $\alpha = 1/3$ fits with an optimal coefficient of determination (R^2 -score) (Table inside plot); Fitting parameter “A” decreases from 19 to 10 as k - grid change from coarse to dense; (c) T_c vs σ for various q - grids keeping k -grid fixed at $12 \times 12 \times 12$. (d) Spectral function $\alpha^2 F(\omega)$ vs ω plots with $\sigma = 0.01$ Ry with k -grid of $8 \times 8 \times 6$.

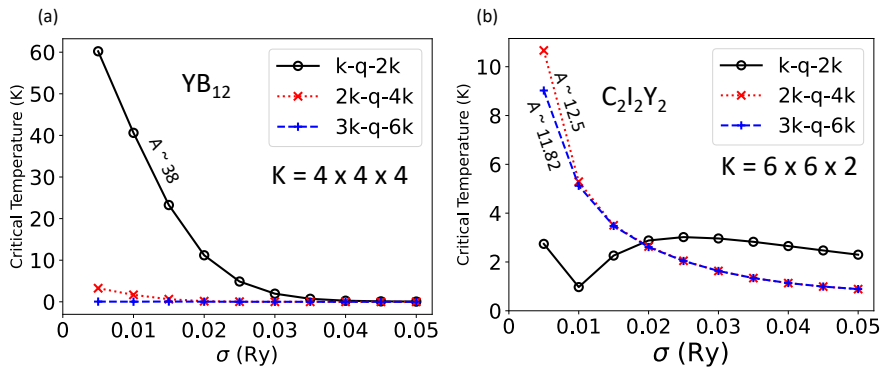


FIG. S12: T_c vs σ for various k - grids; (a) for YB₁₂ and (b) for C₂I₂Y₂.

In Fig. S12, we show two cases of YB_{12} and $\text{C}_2\text{I}_2\text{Y}_2$ in which the coarse \mathbf{k} - grids from Materials Project and fine \mathbf{k} - grid only twice of that result to qualitatively inaccurate results, unusually high T_c for the former while predicting negligible T_c for the latter. With coarse grids, the exponential decay parameter of YB_{12} is around 38, much larger than the critical value estimated for MgB_2 ($A_{\text{MgB}_2} \sim 12$). Increasing \mathbf{k} -mesh grids two times in each direction, T_c drops from 40.6 K to 1.67 K at $\sigma = 0.01$ Ry and drops to almost zero for $\sigma > 0.01$ Ry indicating non-superconductor, which is in good agreement with the experiment [12]. We found a couple of cases such as $\text{C}_2\text{I}_2\text{Y}_2$ when T_c first decreases and increases later with σ (we set $A = 0$ in Fig. S14). Such behavior hasn't been observed in $G(\Delta, \sigma)$ vs σ plots for a wide range of Δ (Fig. 8(a) of the main text). The coarse grids result to a very low T_c of 0.97 K for $\text{C}_2\text{I}_2\text{Y}_2$. However, the denser mesh corrects the behavior with an exponential decay parameter of 12.5 much closer to the reference value of MgB_2 . Also, the critical temperature T_c improves to 5.29 K agreeing much more strongly to the experiment [13]. Note that, this analysis only works for compounds with non-zero T_c for a wide range of σ . For $T_c < \sim 1$ K at $\sigma = 0.01$ Ry (computational details for choosing $\sigma = 0.01$ Ry), $T_c < 0.1$ K for $\sigma > 0.01$ Ry, and rapidly drops to zero for larger σ , we identify the compound to be non-superconducting with the value of A as zero ($A = 0 < A_{\text{MgB}_2}$, already converged). To summarize the ansatz, we present a simple schematics of the process shown as in Fig. S13.

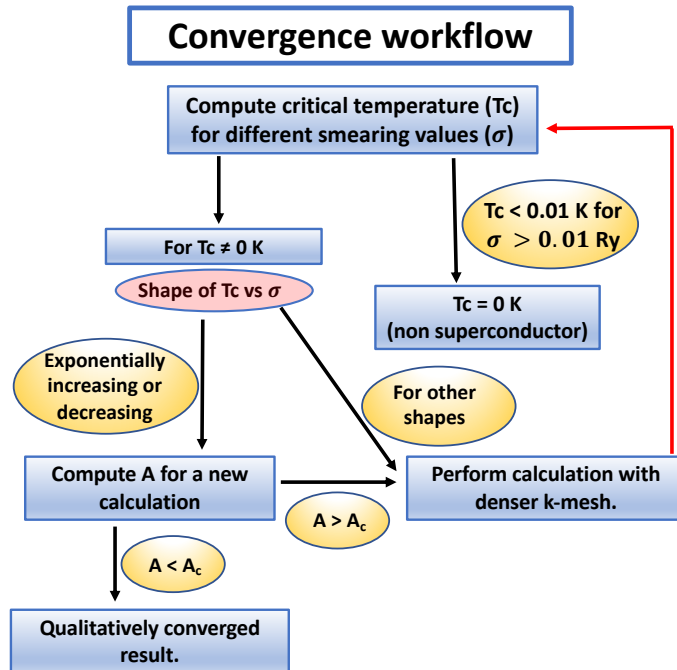


FIG. S13: Schematics of the convergence testing procedure explained in the main text. A_c is the value of the decay parameter computed for MgB_2 . First, we compute T_c for different values of σ . If the variation of T_c with σ decreases exponentially, we compute A . If $A < A_c$, then the results have converged. If the variation increases exponentially and $A < 0$, satisfying $A < A_c$, the results are also considered converged. If $A > A_c$ or if the variation follows a different pattern, the calculations are repeated with a denser \mathbf{k} -mesh. If T_c decreases extremely rapidly with increasing σ , then the material is considered a non-superconductor.

TABLE S7: Comparing results between coarse and fine grids for compounds with $A > A_{MgB_2}$; T_c^{eff} is the critical temperature calculated from efficient EPC calculations, using \mathbf{k} -point mesh grid from MP database; T_c^{Corr} is the critical temperature calculated using denser \mathbf{k} -point mesh and fine \mathbf{k} - mesh grids (2 times of MP database K-point mesh), while \mathbf{q} -grid is kept fixed;

Compound	T_c^{eff} (K)	T_c^{Corr} (K)	T_c^{Expt} (K)
YB ₁₂ (Fm-3m)	40.6	1.67	0 [12][14]
CaNiBN (P4/nmm)	0.96	2.43	2.2 [15]
BaC ₆ (P6 ₃ /mmc)	6.50	1.70	0 [16]
La ₃ PbC (Pm-3m)	3.20	0.50	0 [17][18]
La ₃ SnC (Pm-3m)	5.09	0.81	0 [17] [19]
CsC ₈ (P6/mmm)	5.97	0.4	0.13 [20]
AlB ₂ (P6/mmm)	11.3	0.3	0 [21]
C ₂ I ₂ Y ₂ (C2/m)	0.97	5.29	9.97 [13]
C ₂ Cl ₂ Y ₂ (C2/m)	0.508	2.73	2.3 [22]

TABLE S8: Comparing results between coarse and fine grids for compounds with $A < A_{MgB_2}$; T_c^{eff} is the critical temperature calculated from efficient EPC calculations, using \mathbf{k} -point mesh grid from MP database; T_c^{Corr} is the critical temperature calculated using denser \mathbf{k} -point mesh and fine \mathbf{k} - mesh grids (2 times of MP database K-point mesh), while \mathbf{q} -grid is kept fixed; Here results do not change much qualitatively from coarse to denser mesh. Vertical line in the table after LaB₆ separates data from accurate to inaccurate qualitative predictions, compared to experimental results.

Compound	T_c^{eff} (K)	T_c^{Corr} (K)	T_c^{Expt} (K)
WB (Cmcm)	5.69	4.9	2.8 [23]
ReB ₂ (P6 ₃ /mmc)	0	0	0 [24]
LaB ₆ (Pm-3m)	0.42	0	0.005 [25]
Ta ₂ C (P-3m1)	0.0	0.0	0 [26]
YIr ₃ B ₂ (P6/mmm)	5.5	5.54	N/A [27]
RuB ₂ (Pmmn)	0.59	0.32	1.5 [28]
VC (Fm-3m)	31.67	19.9	3.2 [29]
ZnNi ₃ C (Pm-3m)	15.37	15.4	0 [30][31]
YRh ₃ B ₂ (P6/mmm)	5.8	4.2	0 [32] [33]
YRu ₃ B ₂ (P6/mmm)	3.7	2.12	0 [34][35]

Next, we present results obtained from EPC calculations for 113 known boron and carbon superconducting ($N = 53$) and non-superconducting ($N = 60$) compounds from SuperCon database [36]. Fig. S14 represents the distribution of T_c with respect to exponential decay parameter A for efficient calculations for $\sigma = 0.01$ Ry with $\mu_c^* = 0.16$. Based on the convergence check ansatz, we found that around 15 % (NoConv) of the results are not fully converged, while 70 % of them are qualitatively inaccurate (NoConv-False), compared to available experimental results. Similarly, we have 12 % of cases that have $A < A_{MgB_2}$ with qualitatively inaccurate predictions (Conv-False), which could be attributed from either inaccuracy of approximations to compute T_c or inaccuracies within available experimental results. This work not only addresses the 15 % (NoConv) cases but also assists in validating true (Conv-True) results.

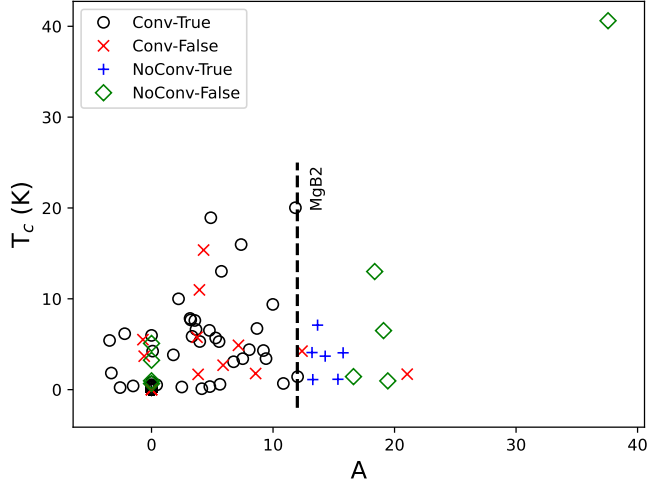


FIG. S14: Critical temperature T_c vs exponential decay parameter (A) plot; Black open circle and red cross symbols represent converged ($A < A_{MgB_2}$) true and false predictions respectively; Blue plus and green diamond symbols represent unconverged ($A > A_{MgB_2}$) true and false predictions respectively; A vertical dashed line at $A = 12$ represents the MgB₂ result; When T_c doesn't exponentially decay or increase with σ (parabolic in nature, first decrease and increase later), those results are simply identified as unconverged, and presented in the plot with $A = 0$; With denser grids, these results of parabolic T_c vs σ nature changes to exponential decay. Here, a true prediction indicates agreement with the available experimental results, while a false prediction indicates disagreement.

We present a few qualitatively inaccurate predictions with $A > A_{MgB_2}$ and improved results with a denser grid in Table S7, while Table S8 shows unaffected results (qualitatively) with denser grids for the cases with $A < A_{MgB_2}$. For example, AlB₂ is predicted to be superconductors with a coarse grid, while it changes to a non-superconductor with a denser grid, consistent with the experimental prediction. Similarly, T_c of superconductors such as CaNiBN, C2I2Y2, and C2Cl2Y2 change from below 1 K (non-superconductor) to a larger value, and show a better agreement with the experiment. On the contrary, the qualitative results remain unchanged for converged calculations represented by $A < A_{MgB_2}$, regardless of their agreement with the experimental references.

XVI Application of convergence ansatz on known compounds of SuperCon

In this section, we compare the computed T_c with available experimental results, as shown in Fig. S2 for efficient EPC calculations with and without improved data for $A > A_{MgB_2}$ (left panel) and $A < A_{MgB_2}$ (right panel) cases respectively. We also highlight some significantly deviated results with red rectangles for efficient calculations. With improved data, computed critical temperatures T_c have much better agreement compared to the references, as indicated by the red rectangle enclosing more data points (right panel of Fig. S2), compared to the plot on the left. The results obtained from the *ab-initio* calculations demonstrate a notable level of accuracy with the mean absolute error (MAE) of 2.21 K for the critical temperature, compared to experiments, highlighting the reliability and robustness of this ansatz test. This is in comparison to the MAE of 3.18 K observed in efficient calculations. Please note that we have exclusively incorporated DFPT T_c results for systems that are dynamically stable. Despite the general agreement between DFPT and experimental findings, there exist notable discrepancies. Instances like ZnNi3C (Pm-3m), with a calculated T_c of 15 K, deviate enormously from the experimental values of 0 K [37]. A comparable investigation of ZnNi3C by Hoffmann *et al.*[38], utilizing different pseudopotentials from the PSEUDODOJO project[39], revealed phonon instabilities in these compounds. Notably, these unstable phonon modes were identified to possess significant mode-resolved EPC strength[40], a finding deserving attention, as we address these concerns in the “Imaginary Phonon Modes and Superconductivity” section. Similarly, Nb2InC (P6₃/mmc) with a calculated T_c of 0.34 K, VC (Fm-3m) at 20 K, and WB (I4₁/amd) at 18.5 K, present a problematic cases. Experimental T_c measurements stand at 3.2 K [29], 4.3 K [41], and 7.5 K [42] for VC, WB, and Nb2InC, respectively. These discrepancies can be ascribed to the constraints of both theoretical approaches and experimental procedures. For instance, older experimental investigations initially reported critical temperatures that were later rectified by more recent experiments or vice versa. For instance, in Ref [43], superconductivity below 4.7 K was claimed in certain YB₁₂ samples, yet subsequent experiments, such as those in [44], failed to corroborate these findings. Furthermore, employing more sophisticated

theoretical methodologies like solving the many-body anisotropic Migdal-Eliashberg equations or utilizing SCDFT to estimate T_c can significantly enhance the accuracy of calculations compared to isotropic methods. As an illustration, when examining MgB₂, T_c calculated using isotropic Eliashberg theory falls within the 15-20 K range. However, in Ref. [45], T_c values of 34-42 K were reported over a range of μ^* values, demonstrating the improvement achievable with these advanced techniques.

In Table S9, we show some of the inaccurate results predicting nonsuperconductors with 2D \mathbf{q} - grids ($4 \times 4 \times 1$). Emergence of strong el-ph coupling and T_c with denser 3D \mathbf{q} - grid ($3 \times 3 \times 3$) is unlikely for such nonsuperconducting predictions with $T_c < 0.01$ K for $\sigma > 0.01$ Ry [Fig. S13].

TABLE S9: Comparison of superconducting properties predicting nonsuperconductors that do not agree with the experiments. Denser \mathbf{k} - and \mathbf{q} - grids do not improve the results.

Compound	Grids	λ	ω_{log} (K)	T_c (K)	T_c^{Expt} (K)
Nb ₂ InC	$12 \times 12 \times 12, 3 \times 3 \times 3$	0.39	285	0.1	7.5 [46]
	$8 \times 8 \times 2, 4 \times 4 \times 1$	0.43	297	0.34	
Ti ₂ InC	$12 \times 12 \times 12, 3 \times 3 \times 3$	0.18	355	0.0	3.1 [47]
	$16 \times 16 \times 4, 4 \times 4 \times 1$	0.13	352	0.0	

XVII DFPT results for dynamically stable compounds

[1] P. B. Allen and R. Dynes, Transition temperature of strong-coupled superconductors reanalyzed, *Phys. Rev. B* **12**, 905 (1975).

[2] T. Koretsune and R. Arita, Efficient method to calculate the electron–phonon coupling constant and superconducting transition temperature, *Comput. Phys. Commun.* **220**, 239 (2017).

[3] M. Wierzbowska, S. de Gironcoli, and P. Giannozzi, Origins of low-and high-pressure discontinuities of t_{-c} in niobium, arXiv preprint cond-mat/0504077 (2005).

[4] W. L. McMillan, Transition temperature of strong-coupled superconductors, *Phys. Rev.* **167**, 331 (1968).

[5] S. Poncé, E. R. Margine, C. Verdi, and F. Giustino, Epw: Electron–phonon coupling, transport and superconducting properties using maximally localized wannier functions, *Comput. Phys. Commun.* **209**, 116 (2016).

[6] J. Bardeen, L. N. Cooper, and J. R. Schrieffer, Theory of superconductivity, *Phys. Rev.* **108**, 1175 (1957).

[7] W. Kang, H.-J. Kim, E.-M. Choi, C. U. Jung, and S.-I. Lee, MgB₂ superconducting thin films with a transition temperature of 39 kelvin, *Science* **292**, 1521 (2001).

[8] S. A. Kuzmichev, T. E. Kuzmicheva, and S. Tchesnokov, Determination of the electron-phonon coupling constants from the experimental temperature dependences of superconducting gaps in MgB₂, *JETP Lett.* **99**, 295 (2014).

[9] K. Choudhary and K. Garrity, Designing high- t_c superconductors with bcs-inspired screening, density functional theory, and deep-learning, *Npj Comput. Mater.* **8**, 244 (2022).

[10] A. Floris, A. Sanna, M. Lüders, G. Profeta, N. Lathiotakis, M. Marques, C. Franchini, E. Gross, A. Continenza, and S. Massidda, Superconducting properties of MgB₂ from first principles, *Physica C: Supercond.* **456**, 45 (2007).

[11] K.-P. Bohnen, R. Heid, and B. Renker, Phonon dispersion and electron-phonon coupling in mgb₂ and alb₂, *Phys. Rev. Lett.* **86**, 5771 (2001).

[12] A. Czopnik, N. Shitsevalova, V. Pluzhnikov, A. Krivchikov, Y. Paderno, and Y. Onuki, Low-temperature thermal properties of yttrium and lutetium dodecaborides, *J. Phys.: Condens. Matter.* **17**, 5971 (2005).

[13] R. W. Henn, W. Schnelle, R. K. Kremer, and A. Simon, Bulk superconductivity at 10 k in the layered compounds $Y_2C_2I_2$ and $Y_2C_2Br_2$, *Phys. Rev. Lett.* **77**, 374 (1996).

[14] No transition observed above 2.5 K.

[15] N. Imamura, H. Mizoguchi, and H. Hosono, Superconductivity in LaT_MBN and La₃T_{M2}B₂N₃ (TM= transition metal) synthesized under high pressure, *J. Am. Chem. Soc.* **134**, 2516 (2012).

[16] S. Nakamae, A. Gauzzi, F. Ladieu, D. L'hôte, N. Emery, C. Hérolé, J. Maréché, P. Lagrange, and G. Loupias, Absence of superconductivity down to 80 mK in graphite intercalated BaC₆, *Solid State Commun.* **145**, 493 (2008).

[17] F. Heiniger, E. Bucher, J. Maita, and P. Descouts, Superconducting and other electronic properties of La₃In, La₃Tl, and some related phases, *Phys. Rev. B* **8**, 3194 (1973).

[18] No transition observed above 1 K.

[19] No transition observed above 1 K.

TABLE S10: EPC properties of dynamically stable compounds

ID	Compound	SG	FE (eV/atom)	λ	ω_{log} (K)	T _c (K)
mp-2252	B2Sc1	191	-0.84	0.34	606	0.032
mp-10020	C1Sc1	225	-0.14	0.61	442	5.086
mp-29941	C1Sc2	164	-0.42	0.24	351	0.0
mp-1232372	B2C2Sc2	194	-0.6	0.21	565	0.0
mp-27693	B8C8Sc4	55	-0.46	0.45	560	1.092
mp-10343	B1C2Sc2	139	-0.57	0.41	467	0.383
mp-10139	B1Sc3Sn1	221	-0.61	0.1	331	0.0
mp-12062	Ag1B2	191	0.52	0.88	568	21.563
mp-7817	B12Y1	225	-0.24	0.48	605	1.69
mp-1084	B12Zr1	225	-0.21	0.61	306	3.409
mp-345	B1Hf1	225	-0.41	0.51	281	1.225
mp-1890	B4Mo4	141	-0.5	0.4	364	0.228
mp-999198	B2Mo2	63	-0.49	0.63	338	4.398
mp-451	B1Zr1	225	-0.37	0.47	383	0.946
mp-763	B2Mg1	191	-0.13	0.78	734	20.027
mp-450	B2Nb1	191	-0.69	0.72	365	7.68
mp-1773	B4Re2	194	-0.43	0.22	409	0.0
mp-1077	B4Ru2	59	-0.29	0.42	364	0.356
mp-1472	B2Zr1	191	-0.99	0.14	581	0.0
mp-2680	B6La1	221	-0.56	0.26	343	0.0
mp-2203	B6Y1	221	-0.4	1.97	81	9.999
mp-1079500	B2Ca2N2Ni2	129	-0.97	0.53	464	2.474
mp-1106180	B6Re14	186	-0.22	0.72	180	3.83
mp-15671	B2Re6	63	-0.2	0.72	209	4.4
mp-2850	B4Os2	59	-0.21	0.61	263	3.07
mp-21502	B4Rh8	62	-0.21	0.65	183	2.692
mp-7857	B4Ti4	62	-0.83	0.27	443	0.0
mp-20881	B2La2N2Ni2	129	-1.05	0.64	301	4.241
mp-9219	B2C1La1Pt2	139	-0.64	0.76	262	6.732
mp-3465	B2La1Rh3	191	-0.67	0.84	174	5.859
mp-6114	B2La3N3Ni2	139	-1.15	0.61	362	4.056
mp-20234	B4Li8Pt12	212	-0.57	1.31	96	7.615
mp-4984	B4Mo10Si2	140	-0.4	0.81	257	7.838
mp-1189073	B8Os4Sc4	62	-0.68	0.63	330	4.305
mp-1105309	B4Ge2Ta10	140	-0.59	0.29	234	0.0
mp-1078866	B4C4Y2	127	-0.44	0.52	455	2.323
mp-15955	B4C4Y2	131	-0.3	0.5	392	1.531
mp-1024989	B2C1Pd2Y1	139	-0.5	1.14	249	15.971
mp-5984	B8Rh8Y2	137	-0.59	0.77	223	5.866
mp-1190832	B16Ru4Y4	55	-0.62	0.28	501	0.0
mp-980205	B16Os4Y4	55	-0.57	0.28	404	0.0
mp-2091	B4V6	127	-0.72	0.23	473	0.0
mp-260	B2Cr2	63	-0.52	0.45	412	0.68
mp-9973	B2V2	63	-0.85	0.23	508	0.0
mp-1183252	B1Ir1	187	-0.2	0.47	214	0.539
mp-567164	B2Rh2	194	-0.39	0.15	313	0.0
mp-1063752	B2Rh2	194	-0.18	0.91	173	7.127
mp-4472	B2C2Mo4	63	-0.25	0.78	199	5.414
mp-10112	B2Ir3La1	191	-0.65	0.62	151	1.828
mp-2536	B2Ni4	140	-0.29	0.22	316	0.0

TABLE S11: EPC properties of dynamically stable compounds

ID	Compound	SG	FE (eV/atom)	λ	ω_{log} (K)	T _c (K)
mp-1491	B2V1	191	-0.74	0.29	494	0.001
mp-8431	B4Ca2Rh4	70	-0.61	0.26	325	0.0
mp-1008487	B2W2	63	-0.36	0.68	274	4.902
mp-10142	B4Ta3	71	-0.77	0.36	357	0.046
mp-865	Ca1B6	221	-0.41	0.16	538	0.0
mp-14445	B4Ca2Ir4	70	-0.68	0.26	338	0.0
mp-944	Al1B2	191	-0.04	0.4	564	0.295
mp-10852	B4C4La2	127	-0.44	0.38	420	0.113
mp-7783	B4C4La2	131	-0.31	0.5	459	1.862
mp-2967	B2Co2La1	139	-0.48	0.31	304	0.002
mp-5992	B2C1Ir2La1	139	-0.57	0.36	250	0.035
mp-568083	B2C1La1Ni2	139	-0.44	0.33	299	0.009
mp-6794	B2C1La1Rh2	139	-0.6	0.35	284	0.022
mp-571428	B6Mg3Ni9	181	-0.38	0.2	353	0.0
mp-4938	B2Co3Sc1	191	-0.55	0.37	275	0.07
mp-6939	B4Ir4Sr2	70	-0.63	0.28	351	0.0
mp-7348	B4Rh4Sr2	70	-0.56	0.23	335	0.0
mp-3515	B2Co2Y1	139	-0.56	0.24	383	0.0
mp-1024941	B2Rh3Y1	191	-0.71	0.76	162	4.181
mp-4382	B2Ru3Y1	191	-0.47	0.62	172	2.121
mp-9956	Al2C2Cr4	194	-0.17	0.24	403	0.0
mp-3271	Al1C1Ti3	221	-0.59	0.28	271	0.0
mp-1025497	Al2C2V4	194	-0.52	0.23	425	0.0
mp-4448	Y3Al1C1	221	-0.42	0.1	254	0.0
mp-1190604	Al8C4Nb12	213	-0.46	0.35	256	0.022
mp-1190760	Al8C4Ta12	213	-0.45	0.4	191	0.111
mp-1214417	Ba2C12	194	-0.09	0.53	300	1.709
mp-9961	C2Cd2Ti4	194	-0.54	0.28	233	0.0
mp-21075	C1Hf1	225	-0.94	0.13	457	0.0
mp-1096993	C2Hf2	194	-0.74	0.46	416	0.865
mp-1002124	Hf1C1	216	-0.3	0.05	424	0.023
mp-10611	C1La3Pb1	221	-0.43	0.49	151	0.516
mp-1206443	C1La3Sn1	221	-0.49	0.53	146	0.806
mp-5443	C2Nb4Sn2	194	-0.42	0.45	271	0.527
mp-20661	C2Pb2Ti4	194	-0.57	0.31	321	0.004
mp-631	C1Ti1	225	-0.81	0.16	601	0.0
mp-1282	C1V1	225	-0.41	1.14	312	19.989
mp-20648	C4V8	60	-0.47	0.3	348	0.001
mp-1008632	C1V2	164	-0.45	0.24	319	0.0
mp-2795	C1Zr1	225	-0.8	0.15	484	0.0
mp-1014307	C2Zr2	194	-0.64	0.41	480	0.321
mp-570112	C4Cr6	63	-0.07	0.55	343	2.407
mp-28861	C8Cs1	191	-0.05	0.4	766	0.438
mp-568643	C16Rb2	70	-0.04	0.5	755	2.902
mp-16290	C1Ni3Zn1	221	-0.06	1.94	126	15.406
mp-1066566	C2Ni1Y1	38	-0.33	0.47	395	1.074
mp-1079635	C2Ga2Mo4	194	-0.12	0.77	249	6.627
mp-2305	C1Mo1	187	-0.08	0.18	512	0.0
mp-1552	C4Mo8	60	-0.11	0.7	272	5.298
mp-1221498	C1Mo2	164	-0.05	0.6	287	3.119

TABLE S12: EPC properties of dynamically stable compounds

ID	Compound	SG	FE (eV/atom)	λ	ω_{log} (K)	T _c (K)
mp-1009832	C1Ta1	216	-0.06	0.69	213	4.034
mp-7088	C1Ta2	164	-0.6	0.22	250	0.0
mp-2034	C4W8	60	-0.02	0.77	212	5.512
mp-33065	C2W4	58	-0.01	0.79	213	6.119
mp-2367	C2La1	139	-0.16	0.5	258	0.978
mp-313	C2Y1	139	-0.19	0.83	282	9.383
mp-1208630	C12Sr2	194	-0.04	0.67	310	5.291
mp-1018048	C2La1Ni1	38	-0.25	0.71	346	6.943
mp-1206284	Br2C2La2	12	-1.12	0.7	174	3.416
mp-20315	C2In2Ti4	194	-0.67	0.13	352	0.0
mp-643367	Br2C2Y2	12	-1.08	0.77	251	6.614
mp-37919	Br2C2Y2	59	-0.08	1.21	109	7.789
mp-23062	C2I2Y2	12	-0.86	0.77	196	5.177
mp-1206889	C2Cl2Y2	12	-1.44	0.6	258	2.725
mp-6576	B2C1Ni2Y1	139	-0.51	0.59	315	3.159
mp-2192	B2Pt2	194	0.07	1.24	188	13.786
mp-1009218	C1Mo1	216	0.5	1.71	103	11.153
mp-632442	Al4C3	1	0.31	0.6	256	2.704
mp-1076	KB6	221	-0.03	0.51	823	3.715
mp-1078278	CrB4	58	-0.31	0.25	622	0.0
mp-1079437	FeB4	58	-0.17	0.9	468	18.723
mp-1080111	B3Mo	166	-0.31	0.29	574	0.001
mp-1106184	MnB4	14	-0.29	0.14	559	0.0
mp-1213975	CaB4	127	-0.39	0.25	551	0.0
mp-1228730	B24Mo7	187	-0.14	1.33	359	28.901
mp-2315	NaB15	74	-0.05	0.1	763	0.0
mp-262	Na3B20	65	-0.06	0.4	782	0.513
mp-27710	CrB4	71	-0.3	0.23	755	0.0
mp-576	B13C2	166	-0.07	0.97	835	39.304
mp-637	YB4	127	-0.59	0.43	388	0.457
mp-7283	LaB4	127	-0.56	0.28	465	0.0
mp-1218188	SrLaB12	123	-0.51	0.36	306	0.041
mp-1232339	LiC12	63	-0.0	0.43	1055	1.24
mp-1227841	BaLaB12	123	-0.49	0.36	304	0.052
mp-1001581	LiC6	191	-0.0	0.39	1043	0.397
mp-1021323	LiC12	191	-0.01	0.33	949	0.035
mp-1001835	LiB	194	-0.17	0.21	328	0.0
mp-1002188	TcB	187	-0.28	0.4	445	0.267
mp-1009695	CaB2	191	-0.14	0.68	444	7.604
mp-1224328	HfNbB4	191	-0.86	0.33	462	0.013
mp-1019317	TcB2	194	-0.44	0.27	497	0.0
mp-1025170	Ti3B4	71	-0.93	0.25	517	0.0
mp-1217974	TaB4W3	25	-0.48	0.6	277	2.921
mp-1080021	Nb2B3	63	-0.75	0.45	409	0.777
mp-1217965	TaB2Mo	38	-0.66	0.57	348	2.788
mp-1102394	Nb5B6	65	-0.77	0.4	398	0.209
mp-1108	TaB2	191	-0.65	1.22	253	18.116
mp-1217924	TaNbC2	166	-0.52	1.41	326	28.387
mp-1217818	TaVB4	191	-0.69	0.6	387	4.047
mp-1206441	V5B6	65	-0.83	0.26	488	0.0

TABLE S13: EPC properties of dynamically stable compounds

ID	Compound	SG	FE (eV/atom)	λ	ω_{log} (K)	T _c (K)
mp-1216709	TiNbB2	38	-0.81	0.31	472	0.005
mp-20857	CoB	62	-0.4	0.11	357	0.0
mp-2580	NbB	63	-0.77	0.31	415	0.005
mp-1215250	ZrB4Mo	191	-0.62	1.3	193	15.047
mp-569803	B2W	194	-0.33	0.48	323	0.999
mp-999120	TcB	194	-0.22	0.42	378	0.335
mp-1215178	ZrTiB4	191	-1.0	0.09	617	0.0
mp-9208	V2B3	63	-0.8	0.29	488	0.001
mp-999118	TcB	194	-0.12	1.32	332	26.488
mp-12054	Cr2B3	63	-0.43	0.56	358	2.753
mp-10114	ScB4Ir3	176	-0.59	0.18	258	0.0
mp-9880	YB2C	135	-0.52	0.32	506	0.012
mp-995282	LiAlB4	55	-0.05	0.5	693	2.659
mp-1008527	B2CN	115	-0.44	0.8	644	18.759
mp-1207086	MgAlB4	191	-0.15	0.34	769	0.059
mp-1215209	ZrTaB4	191	-0.84	0.39	436	0.177
mp-1215223	ZrNbB2	38	-0.71	0.35	404	0.04
mp-1216966	TiCrB4	191	-0.68	0.59	339	3.385
mp-1217028	TiB2Mo	38	-0.82	0.25	461	0.0
mp-1220697	Nb2AlB6	191	-0.47	0.54	431	2.781
mp-1224283	HfTaB4	191	-0.85	0.41	423	0.354
mp-1224291	HfTaB2	38	-0.77	0.4	354	0.199
mp-1224347	HfNbB2	38	-0.76	0.37	387	0.073
mp-1226228	CrB2Mo	38	-0.48	0.62	331	3.919
mp-13341	YB4Rh	55	-0.61	0.62	483	6.008
mp-568985	La2B3Br	187	-0.84	0.35	212	0.018
mp-569002	Y3ReB7	63	-0.33	0.81	330	9.953
mp-1008526	B2CN	156	-0.42	1.11	566	34.9
mp-569121	La2B3Cl	174	-1.02	0.41	209	0.158
mp-1191641	YVB4	55	-0.7	0.3	473	0.001
mp-1216398	VCrB2	38	-0.69	0.39	460	0.19
mp-1216475	V3ReB4	25	-0.72	0.39	391	0.169
mp-1216667	TiVB4	191	-0.9	0.27	516	0.0
mp-1217026	TiB4Mo	191	-0.68	0.69	348	6.374
mp-1217095	Ti3B4Mo	6	-0.83	0.28	454	0.0
mp-1217898	TaTiB4	191	-0.88	0.29	441	0.001
mp-1217997	Ta3AlB8	191	-0.5	0.54	316	1.858
mp-1220349	NbB2W	38	-0.58	0.57	341	2.717
mp-1220351	NbVB4	191	-0.71	0.51	421	1.948
mp-1220383	NbB4Mo3	38	-0.56	0.58	354	3.101
mp-1008525	B2CN	160	-0.43	1.66	577	60.733
mp-10057	VCoB3	63	-0.62	0.26	438	0.0
mp-1226242	CrB2W	38	-0.43	0.74	290	6.877
mp-1228634	B4MoIr	187	-0.25	0.5	280	1.054
mp-1196778	Y2B6Ru	55	-0.66	0.22	511	0.0
mp-22709	TaNiB2	62	-0.63	0.3	324	0.001
mp-569116	Sc2B6Rh	55	-0.73	0.52	414	2.079
mp-1224274	HfTiC2	166	-0.83	0.42	464	0.462
mp-1215222	ZrNbC2	166	-0.66	0.73	397	8.92
mp-1224334	HfNbC2	166	-0.73	0.65	385	5.753

TABLE S14: EPC properties of dynamically stable compounds

ID	Compound	SG	FE (eV/atom)	λ	ω_{log} (K)	T _c (K)
mp-38818	HfNbB4	71	-0.86	0.4	420	0.254
mp-1086667	ScNiC2	129	-0.28	0.52	368	1.864
mp-1217975	Ta3TiB4	25	-0.84	0.26	394	0.0
mp-9530	Y4C7	14	-0.28	0.13	323	0.0
mp-9459	Y4C5	55	-0.33	0.84	225	7.678
mp-1188534	ScCrC2	59	-0.34	0.62	389	4.881
mp-1224170	HfZrC2	123	-0.87	0.25	483	0.0
mp-1334	Y2C	166	-0.29	0.29	201	0.0
mp-1232379	YBC	194	-0.29	0.28	427	0.0
mp-29896	Y2B3C2	65	-0.5	0.6	375	3.915
mp-612670	YNiBC	129	-0.52	0.2	421	0.0
mp-567692	B4C3Ni4Y3	139	-0.51	0.31	393	0.003
mp-12737	B2C1Rh2Y1	139	-0.6	0.38	285	0.098
mp-1087495	Tc3B	63	-0.27	0.8	254	7.66
mp-978989	Tc7B3	186	-0.32	0.68	227	4.037
mp-1068296	Fe(BW)2	71	-0.43	0.45	279	0.465
mp-11750	Ti6Si2B	189	-0.66	0.22	333	0.0
mp-1238800	CaBC	194	-0.07	0.42	501	0.494
mp-27261	Ba7(BIr)12	166	-0.48	0.47	233	0.626
mp-29980	Nb4B3C2	63	-0.59	1.01	219	11.258
mp-29979	Nb3B3C	63	-0.66	1.22	229	16.438
mp-541849	Al3(BRu2)2	123	-0.59	0.26	308	0.0
mp-1188408	Zr5Sn3B	193	-0.68	0.45	202	0.343
mp-1206909	CaBPd3	221	-0.56	1.1	103	6.187
mp-9985	NbNiB	63	-0.56	0.34	256	0.018
mp-1080829	Ti6Ge2B	189	-0.62	0.21	305	0.0
mp-1025192	Ta4C3	221	-0.45	1.46	138	12.644
mp-1215211	ZrNbB4	191	-0.85	0.31	479	0.005
mp-1220641	Nb3B4W3	38	-0.43	0.46	299	0.66
mp-10721	Ti2C	227	-0.64	0.14	386	0.0
mp-27919	Ti8C5	166	-0.72	0.22	455	0.0
mp-1218000	Ta4C3	160	-0.55	0.52	183	0.919
mp-1220752	Nb10(SiB)3	42	-0.65	0.24	310	0.0
mp-1189539	Hf2Al3C5	194	-0.13	0.47	1454	3.645
mp-9958	Ti2GeC	194	-0.81	0.48	276	0.847
mp-1025524	Zr2TlC	194	-0.63	0.21	188	0.0
mp-1216707	TiNbC2	166	-0.67	0.73	422	9.623
mp-1079992	Zr2PbC	194	-0.66	0.4	230	0.146
mp-1207413	Zr5Sn3C	193	-0.68	0.53	180	1.013
mp-1217106	Ti2C	166	-0.63	0.35	357	0.037
mp-1217822	TaVC2	166	-0.46	0.8	343	10.296
mp-12990	Ti2AlC	194	-0.7	0.25	371	0.0
mp-3871	Ti2SnC	194	-0.73	0.24	353	0.0
mp-1025427	Ta2GaC	194	-0.52	0.45	231	0.385
mp-1078712	Hf2TlC	194	-0.63	0.21	171	0.0
mp-1079076	Hf2PbC	194	-0.63	0.41	194	0.15
mp-1079908	Ti2SiC	194	-0.79	0.4	334	0.205
mp-1220365	NbVC2	166	-0.39	0.83	365	11.893
mp-21023	Ti3SnC2	194	-0.79	0.18	421	0.0
mp-22144	Ta2InC	194	-0.38	0.37	233	0.062

TABLE S15: EPC properties of dynamically stable compounds

ID	Compound	SG	FE (eV/atom)	λ	ω_{log} (K)	T _c (K)
mp-13137	Hf2CS	194	-1.51	0.19	303	0.0
mp-1220725	Nb2CN	166	-0.8	0.88	310	11.685
mp-1216616	V2CN	166	-0.8	1.0	322	16.224
mp-1214755	BPd6	15	-0.2	0.16	169	0.0
mp-7424	BPd2	58	-0.27	0.42	159	0.16
mp-1078540	Ni6Ge2B	189	-0.31	0.34	190	0.011
mp-1078623	Zr2BIr6	225	-0.81	0.36	184	0.03
mp-12073	Ba(BIr)2	139	-0.5	0.37	269	0.051
mp-7349	Ba(BRh)2	139	-0.48	0.29	295	0.001
mp-7705	NbFeB	187	-0.12	1.76	162	18.063
mp-1215258	ZrBeB	187	-0.58	0.45	436	0.751
mp-1208348	Ta5Ga3B	193	-0.42	0.31	190	0.002
mp-605839	Li2B2Rh3	55	-0.5	0.27	302	0.0
mp-8308	Ca3Ni7B2	166	-0.34	0.13	305	0.0
mp-1206490	Nb2B2Mo	127	-0.64	0.28	367	0.0
mp-31052	LaBPt2	180	-0.92	0.28	142	0.0
mp-1223681	La2(Ni2B)3	44	-0.33	0.46	227	0.517
mp-1097	B2Ta2	63	-0.81	0.41	366	0.297
mp-28930	C16K2	70	-0.03	0.57	1102	8.897
mp-7832	B4W4	141	-0.37	1.58	186	18.463
mp-28613	B3Li3Pt9	189	-0.51	0.4	155	0.088
mp-569759	B4Rh8Zn5	65	-0.42	0.26	222	0.0
mp-571419	Al4C5Zr2	166	-0.35	0.36	387	0.06
mp-1207385	Al8C8Zr2	164	-0.25	0.26	482	0.0
mp-1189895	B2Ge6Ta10	193	-0.45	0.61	181	2.053
mp-10140	B1Sc3Tl1	221	-0.36	0.54	216	1.324
mp-1216165	B1Si6Y10	162	-0.65	0.4	166	0.103
mp-20175	C2In2Sc4	194	-0.55	0.22	170	0.0
mp-20983	C2In2V4	194	-0.34	0.35	349	0.03
mp-1224263	B4Hf1Ti1	191	-1.02	0.1	592	0.0
mp-1224184	B4Hf1Zr1	47	-1.0	0.15	507	0.0
mp-8307	B2Ca2Ni8	191	-0.3	0.33	129	0.004
mp-4079	Al1C1Sc3	221	-0.59	0.04	303	0.048
mp-1103814	C3K5N6	229	-0.52	0.08	190	0.0
mp-1224285	C2Hf1Ta1	166	-0.81	0.62	359	4.486
mp-1215219	C2Ta1Zr1	166	-0.74	0.65	370	5.558
mp-570499	B2La5N6	12	-1.51	0.25	351	0.0
mp-569935	B2La3N4	71	-1.5	0.26	378	0.0
mp-1223086	C6La2Y1	12	-0.16	0.56	271	2.049
mp-1221519	C1Mo2N1	25	-0.35	0.37	473	0.105
mp-1222150	Al1B10Mg4	191	-0.14	0.59	768	7.488
mp-1189984	C8Mo4Y4	62	-0.24	0.61	409	4.562
mp-3380	C8La4Rh4	76	-0.33	0.27	263	0.0
mp-4262	BeAlB	216	-0.05	0.16	578	0.0
mp-5971	YBPt2	180	-1.0	0.18	191	0.0
mp-9596	La(BIr)4	86	-0.58	0.47	201	0.503
mp-1105186	Cu3B5Pt9	189	-0.21	0.4	164	0.099
mp-1106165	Nb5Si3B	193	-0.69	0.46	282	0.638
mp-1106398	V5Ge3B	193	-0.46	0.38	303	0.11
mp-1188194	Ta3B2Ru5	127	-0.53	0.33	146	0.006

TABLE S16: EPC properties of dynamically stable compounds

ID	Compound	SG	FE (eV/atom)	λ	ω_{log} (K)	T_c (K)
mp-29723	LaB ₂ Ru ₃	191	-0.41	0.67	148	2.477
mp-22759	CoBW	62	-0.43	0.37	342	0.071
mp-28786	Zn(BIr) ₂	139	-0.32	0.08	319	0.0
mp-9999	Ni(BMo) ₂	71	-0.48	0.3	352	0.001
mp-1076987	TaNiB	63	-0.62	0.3	253	0.001
mp-3348	LiBiIr	70	-0.51	0.16	325	0.0
mp-2760	Nb ₆ C ₅	12	-0.55	0.51	393	1.632
mp-32679	Nb ₁₀ C ₇	12	-0.48	0.45	301	0.537
mp-1226378	Cr ₂ C	164	-0.04	0.38	376	0.118
mp-2318	Nb ₂ C	164	-0.45	0.31	285	0.002
mp-974437	Re ₂ C	194	-0.03	0.32	348	0.007
mp-10037	AlCo ₃ C	221	-0.22	0.1	212	0.0
mp-9987	Nb ₂ PC	194	-0.75	0.44	345	0.493
mp-21003	Y ₂ ReC ₂	62	-0.42	0.29	282	0.0
mp-28767	Sc ₅ Re ₂ C ₇	65	-0.48	0.21	384	0.0
mp-567462	Sc ₃ RhC ₄	12	-0.5	0.68	393	6.91
mp-7130	ScRu ₃ C	221	-0.28	0.4	227	0.12
mp-996161	Nb ₃ AlC ₂	194	-0.52	0.36	384	0.048
mp-996162	Nb ₂ AlC	194	-0.51	0.46	337	0.768
mp-1078811	Nb ₂ GeC	194	-0.51	0.45	307	0.531
mp-1080835	V ₂ GaC	194	-0.52	0.27	375	0.0
mp-1189574	YWC ₂	62	-0.27	0.54	389	2.392
mp-4992	ScCrC ₂	194	-0.34	0.62	415	4.966
mp-8044	V ₂ PC	194	-0.69	0.4	409	0.227
mp-10046	V ₂ AsC	194	-0.53	0.47	354	0.878
mp-1212439	Hf ₅ Al ₃ C	193	-0.47	0.2	2988	0.0
mp-1217764	Ta ₂ CN	123	-0.82	2.7	127	19.495
mp-37179	Ta ₂ CN	141	-0.84	1.94	162	19.757
mp-4384	Nb ₂ CS ₂	166	-1.12	1.03	222	11.827
mp-559976	Ta ₂ CS ₂	164	-1.19	0.55	251	1.71
mp-995201	Ti ₅ Si ₃ C	193	-0.82	0.55	253	1.784
mp-1025441	Ta ₂ AlC	194	-0.52	0.44	272	0.374
mp-1079546	Nb ₂ GaC	194	-0.52	0.44	263	0.424
mp-1220371	NbAlVC	164	-0.47	0.44	362	0.491
mp-3732	Ti ₂ CS	194	-1.42	0.2	473	0.0
mp-4563	Ti ₃ TiC	221	-0.44	0.29	229	0.0
mp-1216139	Y ₄ C ₄ I ₃ Br	8	-0.91	0.84	174	5.825
mp-1220491	Nb ₆ V ₂ (CS ₂) ₃	12	-1.09	0.54	278	1.768
mp-1220693	Nb ₂ CuCS ₂	156	-0.9	0.85	207	7.255
mp-1215225	ZrTaCN	160	-1.15	0.78	301	8.323
mp-1025205	Y ₂ Re ₂ Si ₂ C	12	-0.62	0.73	172	3.887
mp-1215184	ZrTiCN	160	-1.33	0.43	437	0.5
mp-1224279	HfTiCN	160	-1.41	0.4	420	0.267
mp-1009894	Zr ₁ C ₁	216	-0.19	0.01	444	0.405
mp-1068661	ZrBRh ₃	221	-0.75	0.01	197	0.176
mp-1145	B ₂ Ti ₁	191	-1.06	0.11	638	0.0

TABLE S17: EPC properties of dynamically stable compounds

ID	Compound	SG	FE (eV/atom)	λ	ω_{log} (K)	T _c (K)
mp-1080664	B4Cr4	141	-0.53	0.27	449	0.0
mp-1994	B2Hf1	191	-1.02	0.16	518	0.0
mp-2331	B4Mo2	166	-0.43	0.4	437	0.239
mp-20689	B4Nb6	127	-0.63	0.26	365	0.0
mp-13415	B4Ta6	127	-0.67	0.24	306	0.0
mp-910	C1Nb1	225	-0.46	1.11	309	18.924
mp-1094093	C2Nb2	194	-0.35	1.14	300	19.284
mp-999388	C2Nb2	194	-0.33	0.84	455	15.269
mp-999377	C2Nb2	194	-0.09	0.71	320	6.7
mp-1086	C1Ta1	225	-0.58	0.68	236	4.239
mp-1207750	Y5(SiB4)2	127	-0.68	0.33	401	0.014
mp-1217023	TiB2W	38	-0.78	0.3	419	0.001
mp-1079333	B2CN	51	-0.53	0.46	1045	2.381
mp-13854	B3Ru2	194	-0.33	0.14	445	0.0
mp-14019	NiB	63	-0.24	0.24	376	0.0
mp-1018050	CrC	187	-0.0	0.23	610	0.0
mp-1215480	Zr3NbC4	166	-0.73	0.77	346	9.324
mp-1216691	TiVC2	166	-0.62	0.53	446	2.47
mp-1215174	ZrTiC2	123	-0.71	0.25	461	0.0
mp-1215218	ZrMoC2	166	-0.35	1.79	120	13.656
mp-4893	Hf2SnC	194	-0.78	0.31	205	0.003
mp-5659	Ti3SiC2	194	-0.82	0.37	345	0.081
mp-1092281	Ti2TlC	194	-0.57	0.14	295	0.0
mp-3747	Ti3AlC2	194	-0.76	0.26	342	0.0
mp-3886	Zr2AlC	194	-0.64	0.56	163	1.181
mp-1188856	V5Si2B	140	-0.39	0.37	302	0.067
mp-1216445	V9Cr3B8	10	-0.7	0.25	459	0.0
mp-1216643	V10Si6B	162	-0.63	0.33	323	0.014
mp-1220688	Nb3Re3B4	38	-0.35	0.53	265	1.47
mp-1226327	Cr3B4Mo3	38	-0.29	0.78	289	8.091
mp-1009817	C1Ta1	187	-0.16	1.54	235	22.8
mp-1542	YB2	191	-0.56	0.42	473	0.453
mp-1216692	TiNbB4	191	-0.89	0.29	481	0.001
mp-4613	Zr2SnC	194	-0.79	0.32	259	0.004
mp-1232384	ZrBC	194	-0.32	1.12	320	19.998

- [20] J. Chacón-Torres and T. Pichler, Defect modulated raman response of KC8 single crystals, Phys. Status Solidi (b) **248**, 2744 (2011).
- [21] U. Burkhardt, V. Gurin, F. Haarmann, H. Borrmann, W. Schnelle, A. Yaresko, and Y. Grin, On the electronic and structural properties of aluminum diboride Al_{0.9}B₂, J Solid State Chem. **177**, 389 (2004).
- [22] M. Bäcker, A. Simon, R. K. Kremer, H.-J. Mattausch, R. Dronskowski, and J. Rouxel, Superconductivity in intercalated and substituted y₂br₂c₂, Angew. Chem. Int. Ed. Engl. **35**, 752 (1996).
- [23] M. Kayhan, E. Hildebrandt, M. Frotscher, A. Senyshyn, K. Hofmann, L. Alff, and B. Albert, Neutron diffraction and observation of superconductivity for tungsten borides, WB and W₂B₄, Solid State Sci. **14**, 1656 (2012).
- [24] C. Pei, J. Zhang, C. Gong, Q. Wang, L. Gao, Y. Zhao, S. Tian, W. Cao, C. Li, Z.-Y. Lu, et al., Distinct superconducting behaviors of pressurized WB₂ and ReB₂ with different local b layers, Sci. China: Phys. Mech. Astron. **65**, 1 (2022).
- [25] I. Bat'Ko, M. Bat'Kova, K. Flachbart, V. Filippov, Y. B. Paderno, N. Y. Shicevalova, and T. Wagner, Electrical resistivity and superconductivity of LaB₆ and LuB₁₂, J. Alloys Compd. **217**, L1 (1995).
- [26] V. Hadjiev, E. Baburaj, and J. Guan, Phonons in ultra-high melting temperature Ta₂C, EPL (Europhys. Lett.) **111**, 68001 (2015).
- [27] Not reported.

[28] S. Datta, A. Vasdev, S. Halder, J. Singh, Y. Singh, and G. Sheet, Spectroscopic signature of two superconducting gaps and their unusual field dependence in RuB₂, *J. Phys.: Condens. Matter.* **32**, 315701 (2020).

[29] K. Langguth, Production of superconducting vanadium carbide by ion implantation, Tech. Rep. (Kernforschungszentrum Karlsruhe (Germany, 1977).

[30] M.-S. Park, J. Giim, S.-H. Park, Y. Lee, S. Lee, and E. Choi, Physical properties of ZnCNi₃: comparison with superconducting MgCNi₃, *Supercond. Sci. Technol.* **17**, 274 (2003).

[31] No transition observed above 2.0 K.

[32] D. Johnston, Superconductivity in a new ternary structure class of boride compounds, *Solid State Commun.* **24**, 699 (1977).

[33] No transition observed above 1.5 K.

[34] H. Ku, G. Meisner, F. Acker, and D. Johnston, Superconducting and magnetic properties of new ternary borides with the CeCo₃B₂-type structure, *Solid State Commun.* **35**, 91 (1980).

[35] No transition observed above 1.2 K.

[36] National institute of materials science, materials information station, http://supercon.nims.go.jp/index_en.html, SuperCon (2018).

[37] M.-S. Park, J. Giim, S.-H. Park, Y. Lee, S. Lee, and E. Choi, Physical properties of ZnCNi₃: comparison with superconducting MgCNi₃, *Supercond. Sci. Technol.* **17**, 274 (2003).

[38] N. Hoffmann, T. F. Cerqueira, J. Schmidt, and M. A. Marques, Superconductivity in antiperovskites, *Npj Comput. Mater.* **8**, 150 (2022).

[39] M. J. van Setten, M. Giantomassi, E. Bousquet, M. J. Verstraete, D. R. Hamann, X. Gonze, and G.-M. Rignanese, The pseudodojo: Training and grading a 85 element optimized norm-conserving pseudopotential table, *Comput. Phys. Commun.* **226**, 39 (2018).

[40] N. Hoffmann, T. F. Cerqueira, J. Schmidt, and M. A. Marques, Superconductivity in antiperovskites, Materials Cloud Archive 2022.49 (2022).

[41] M. Kayhan, E. Hildebrandt, M. Frotscher, A. Senyshyn, K. Hofmann, L. Alff, and B. Albert, Neutron diffraction and observation of superconductivity for tungsten borides, WB and W₂B₄, *Solid State Sci.* **14**, 1656 (2012).

[42] A. Bortolozo, Z. Fisk, O. Sant'Anna, C. Dos Santos, and A. Machado, Superconductivity in Nb₂InC, *Physica C Supercond.* **469**, 256 (2009).

[43] B. Matthias, T. Geballe, K. Andres, E. Corenzwit, G. Hull, and J. Maita, Superconductivity and antiferromagnetism in boron-rich lattices, *Science* **159**, 530 (1968).

[44] A. Czopnik, N. Shitsevalova, V. Pluzhnikov, A. Krivchikov, Y. Paderno, and Y. Onuki, Low-temperature thermal properties of yttrium and lutetium dodecaborides, *J. Condens. Matter Phys.* **17**, 5971 (2005).

[45] G. P. Kafle, C. R. Tomassetti, I. I. Mazin, A. N. Kolmogorov, and E. R. Margine, Ab initio study of Li-Mg-B superconductors, *Phys. Rev. Mater.* **6**, 084801 (2022).

[46] E. Karaca, P. J. P. Byrne, P. J. Hasnip, and M. Probert, Prediction of phonon-mediated superconductivity in new Ti-based M₂AX phases, *Scientific reports* **12**, 13198 (2022).

[47] A. Bortolozo, O. Sant'Anna, C. Dos Santos, and A. Machado, Superconductivity in the hexagonal-layered nanolaminates Ti₂InC compound, *Solid State Communications* **144**, 419 (2007).